UNIVERSITY OF CALIFORNIA, SAN DIEGO

Spectral Characterization of Ekman Velocities in the Southern Ocean Based on Surface Drifter Trajectories.

A dissertation submitted in partial satisfaction of the
requirements for the degree Doctor of Philosophy
in
Oceanography

by

Shane Elipot

Committee in charge:

Sarah Gille, Chair
Bruce Cornuelle
Glenn Ierley
Peter Niiler
Sutanu Sarkar

2006

The dissertation of Shane Elipot is approved, and it is acceptable in quality and form for publication on microfilm:

Chair

University of California, San Diego

2006

To my godson and nephew Zenon Duncan Elipot.

TABLE OF CONTENTS

LIST OF FIGURES

LIST OF TABLES

ACKNOWLEDGMENTS

I would like to acknowledge and thank here the colleagues and friends who had an influence on this work.

I would like to thank Sharon Lukas who got me started with the drifter dataset in the Southern Ocean. I would like to thank Tomomi Ushii and Dawn Huffman for their administrative assistance.

I am grateful to Jennifer MacKinnon who asked how much energy was there, which is a very relevant question. I would like to thank Jonathan Lilly who assured me that I should be able to derive a spectral equation, which I did. I would like to thank Jurgen Theiss for his enthusiastic and polarized interest. I would like to thank Nikolai Maximenko for his disinterested help.

I would like to thank my dear friend Yueng Djern Lenn Polton for our stimulating discussions about the Southern Ocean, and most importantly for holding my hand above and below the water. I thank my classmates from the very first day and after, Elena Brambilla, Elizabeth Douglass, Chad English, Josh Willis, Jessica Kleiss, and Sarah Zedler for being such good pals.

I am deeply grateful to my friends who kept me in check and made me so happy throughout all these years, Eduardo Balcazar, Brian Moore, James Geiger, Shannon Otterbeck, Elisa Kreth, Kate Buska, Tanya Bloch, Lolita Pellos, Remi Dingreville, Sylvain Rigal, Tilia Caizergues, Julie Bassuel, and Benjamin Nicot.

I am indebted to Paul Robbins and Paulette Murphy for being so helpful during my last months in San Diego.

I would like to thank Lisa Beal and Teresa Chereskin for requesting my presence onboard the R/V Melville for the Aguhlas Under-Current Experiment cruise. I would like to thank Greg Mitchell for allowing me onboard the ARSV Laurence M. Gould for the Blue Water Zone cruise.

I am immensely indebted to Lisa Beal for being a mentor in my scientific life and actually in some other parts of my life, too.

I am grateful to Glenn Ierley for keeping an eye on my mathematical derivations. I am indebted to Peter Niiler for letting me drift the way I wanted to. I regret that Colm-Cille Caulfield could not remain on my committee in the end, and I would like to thank him for his warm encouragements. I would like to thank Bruce Cornuelle for always showing interest my this work. I would like to thank Sutanu Sarkar for agreeing to be on my committee.

Finally, I would like to thank my advisor Sarah Gille whose help, support and careful attention to my work were so devoted and inspiring that I always felt like the luckiest graduate student in the place.

VITA

2006	Ph.D. in Oceanography, Scripps Institution of Oceanography, University of California, San Diego, La Jolla.
2001-2006	Graduate Student Researcher, Scripps Institution of Oceanography, University of California, San Diego, La Jolla.
2001	*Diplôme d'Etudes Approfondies* in Meteorology, Oceanology and Environment, *Université de Bretagne Occidentale*, Brest, France.
2001	Diplôme d'Ingénieur, *Ecole Nationale Supérieure* *des Ingénieurs des Etudes et Techniques d'Armement*, Brest, France.
1995-1998	*Classes Préparatoires aux Grandes Ecoles d'ingénieur*, *Physique, Chimie et Sciences de l'Ingénieur*, *Physique, Chimie**, Lycée Henri Poincaré, Nancy, France.

PUBLICATIONS

Lisa M. Beal, Teresa. K. Chereskin, Yueng D. Lenn, and **Shane Elipot**, 2006, The Sources and Mixing Characteristics of the Agulhas Current. *J. Phys. Oceanogr.*, in press.

PRESENTATIONS

Elipot, S. and and S. Gille, 2006: Wind energy input and vertical viscosity in the Southern Ocean, *Ocean Sciences*, Honolulu, Hawaii.

Elipot, S. and S. Gille, 2004: Evidence of frequency dependent Ekman currents from drifters in the Southern Ocean, *Ocean Sciences*, Portland, Oregon.

Elipot, S. and S. Gille, 2003: Comparing drifter and altimeter-derived velocities in the Southern Ocean, *From TOPEX/Poseidon to JASON, SWT meeting*, Arles, France.

Elipot, S. and S. Gille, 2002: Spectral response of the Southern Ocean surface circulation to wind, , *WOCE and Beyond Conference*, San Antonio, Texas.

FIELDS OF STUDY

Studies in Physical Oceanography.
Professors M. Hendershott, and P. Robbins

Studies in the Analysis of Physical Oceanography Data.
Professors S. Gille and R. Pinkel

Studies in Fluid Mechanics.
Professors C. Winant

Studies in Geophysical Fluid Dynamics.
Professors P. Cessi and R. Salmon

Studies in Linear and Nonlinear Waves.
Professors M. Hendershott, R. Guza, and K. Melville

Studies in Ocean Turbulence and Mixing.
Professors L. Armi

Studies in Methods of Applied Analysis
Professors G. Ierley, S. Llewellyn Smith and W. Young

ABSTRACT OF THE DISSERTATION

Spectral Characterization of Ekman Velocities in the Southern Ocean Based on Surface Drifter Trajectories.

by

Shane Elipot
Doctor of Philosophy in Oceanography
University of California, San Diego, 2006
Professor Sarah Gille, Chair

Velocity time series from surface drifter data are exploited in a novel way to study the Southern Ocean surface circulation response to wind forcing. The ageostrophic component of the drifter velocities at 15 m is approximated by subtracting altimeter-derived geostrophic velocities from the drifter velocities. The resultant ageostrophic velocity time series are studied in the frequency domain jointly with contemporaneous time series of local wind stress from atmospheric reanalysis data.

Rotary spectral analysis indicates that both wind stresses and ocean velocities are predominantly anticyclonic. Cross-spectral analysis shows that the upper ocean responds preferentially to anticyclonic winds not only at the inertial frequency but also at subinertial frequencies. The phase of the cross-spectra which is interpreted as a geometric angle indicates that the component of velocity that is coherent with the wind stress is to the left of the wind at subinertial frequencies and to the right at supra-inertial frequencies, and is seen as evidence of Ekman-type currents.

A first order closure of the oceanic vertical turbulence, where the oceanic stress is equal to a viscosity coefficient K times the velocity vertical shear, is used to interpret the cross-spectrum. In this framework, the real part of the cross-spectrum of the wind stress and ocean surface ageostrophic velocity is shown to be a measure of the wind energy input rate to the Ekman layer. This energy input is therefore estimated across the Southern Ocean.

The observed transfer function, which is the cross-spectrum divided by the auto-spectrum of the wind stress, is compared to the theoretical transfer functions arising from 10 different Ekman-type boundary layer models. These models differ in the dependence of K on the vertical coordinate and in the bottom boundary condition. The most dynamically consistent model has a vertical viscosity that is finite at the surface and increases linearly to the bottom of the boundary layer depth. Results of the comparison to models provide in situ seasonal estimates of zonally averaged near-surface viscosities and boundary layer depths across the Southern Ocean.

Chapter 1

The Southern Ocean, global oceanic circulation, and energetics

1.1 The wind energy input in the Southern Ocean

Strong and highly variable winds over the Southern Ocean drive the Antarctic Circumpolar Current (ACC). The tilted isopycnals associated with this flow outcrop in the same region where an Ekman transport drives surface water equatorward. The interaction of these two processes suggests that intense mixing is occurring there, and as such, the Southern Ocean is thought to be a major contributor to the total wind-induced mixing which is required to sustain the global thermohaline circulation (Wunsch and Ferrari, 2004). These processes induce transfers of mechanical energy from the atmosphere to the ocean. These transfers take place through different physical mechanisms that can be distinguished by the time scales on which they occur.

First, at low frequencies, the wind stress $\boldsymbol{\tau}$ works on the ocean general circulation (represented by the geostrophic velocity $\mathbf{u}_g$ at the surface) as:

$$\boldsymbol{\tau} \cdot \mathbf{u}_g \equiv \mathbf{U}_e \cdot \nabla p_s / \rho. \tag{1.1}$$

Eq. (1.1) can be seen as either a direct generation of geostrophic kinetic energy or as an increase in potential energy by the work of the Ekman transport $\mathbf{U}_e$ against the pressure forces at the surface $\nabla p_s/\rho$ (Gill et al., 1974; Fofonoff, 1981). Weijer and Gille (2005) showed that the potential energy framework is more germane to the energetics of a numerical model of the Southern Ocean. Wunsch (1998) estimated the left-hand side of Eq. (1.1) by using altimeter-derived geostrophic velocities and wind stress field analyses for the 1992-96 time period. In his estimate, 95% came from the time mean components of $\boldsymbol{\tau}$ and $\mathbf{u}_g$. Over the global ocean, the maximum energy input rates, greater than 20×10^{-3} W m^{-2}, were found in the Southern Ocean (his Fig. 2). Moreover, 70% of the wind work integrated over the surface of the global ocean was found south of 40°S. Huang et al. (2006) studied the decadal variability of this energy input from both altimetry data and numerical model outputs. They found that the ACC region is where most of the variability is found for the 1979-2003 time period and furthermore that it is increasingly dominant in the global integral.

Second, at high frequencies, around the inertial frequency $-f/2\pi$, where f is the Coriolis parameter[1], inertial motions are triggered in the mixed layer by rapid, small-scale wind stress fluctuations (e.g. D'Asaro, 1985b; Poulain, 1990) and resonance can occur when the wind stress contains a significant rotary spectral component at the inertial frequency (e.g. Crawford and Large, 1996). The associated energy flux has attracted interest, because it is oriented towards the ocean interior and downward by propagating internal waves (e.g. D'Asaro et al., 1995). These waves eventually dissipate and can drive diapycnal mixing (Gregg, 1987). The energy flux to mixed layer near-inertial motions has been estimated from wind stress and ocean velocities measured at mooring locations (D'Asaro, 1985a) or more recently from global wind stress analyses (Alford, 2001; Watanabe and Hibiya, 2002; Alford, 2003). In these global studies, the inertial velocities $\mathbf{u}_i$ were inferred from Pollard and Millard's (1970) damped slab-layer model for which the inertial currents are uniform in the vertical. By using either numerical integration in time or spectral resolution of the equations, the wind energy input was computed as $\boldsymbol{\tau} \cdot \mathbf{u}_i$. Alford (2003) included depth-uniform Ekman velocities $\mathbf{u}_e$ arising from a time-varying Ekman transport, because their energy is also available for dissipa-

---

[1] Throughout this dissertation f will either have units of radians per second or radians per day.

tion, but their impact was modest in the final results. For the period 1989-95, he found an average zonal-mean energy input rate at 40°S of about 3×10^{-3} W m^{-2} (his Fig. 1). However, this value may be too large since Plueddemann and Farrar (2006) showed that the slab layer model systematically results in an overestimation of the work done on mixed-layer inertial currents.

Third, what energy fluxes are taking place at intermediate or "sub-inertial" frequencies? Vertically-sheared Ekman currents are expected to exist at all frequencies of forcing: Gonella (1972) extended Ekman's (1905) theory by retaining the time-varying terms and derived several frequency and depth dependent transfer functions. The resulting Ekman velocities $\mathbf{u}_e$, spiral with depth and rotate with the wind-forcing frequency and also exhibit a resonance at the inertial frequency. While the Ekman currents themselves should play a role in the wind energy input into geostrophic currents via Eq. (1.1), maintaining the Ekman spiral requires dissipation within the Ekman layer, or a wind energy input rate "to the Ekman layer".

To estimate this, Wang and Huang (2004) used a spectral approach to compute the ocean surface Ekman velocities from wind stress analyses as a function of frequency, assuming the simplest frequency dependent Ekman model with a constant vertical viscosity. They set the Ekman depth to be proportional to the mean friction velocity ($\sqrt{|\boldsymbol{\tau}|/\rho}$) and inversely proportional to the Coriolis parameter, which implies through Ekman scaling that the vertical viscosity was proportional to the mean wind stress and inversely proportional to the Coriolis parameter. The total wind energy input into the Ekman layer was then obtained by summing the dot products $\boldsymbol{\tau}\cdot\mathbf{u}_e$ computed for each frequency component. It was apparent that the global integral for this energy input is also dominated by the contribution from the Southern Hemisphere. Examination of Fig. 3 in Wang and Huang (2004) reveals that this is mainly due to the strong winds over the Southern Ocean and notably large values over the ACC of about 20×10^{-3} W m^{-2}. They also computed the changes of the global energy input to the Ekman layer over the 1948-2002 time period, which Huang et al. (2006) subsequently attributed to wind stress variability in the equatorial region and in the Southern Ocean.

Because the upper ocean is a complicated place where linear and non-linear superpositions of geostrophic, tidal, wave-induced and inertial currents are expected, observations of frequency dependent Ekman currents as formulated by Gonella (1972) and their relationship to the wind stress are few (see Table 2.3). From surface drifter data, however, attention has been drawn to frequency dependent motions. The work of Rio and Hernandez (2003) shared some common analyses techniques with this current work, though their purpose was ultimately different, i.e. estimating ageostrophic currents on a global scale.

In Chapter 2 of this dissertation, it is shown again that wind-driven currents at a wide range of frequencies can be identified using spectral and cross-spectral analysis of surface drifter velocities and wind stresses, and we describe the spectral results in greater detail than Rio and Hernandez (2003). In Chapter 3, it is argued that the rate of wind energy dissipation that is needed to sustain the Ekman balance can be estimated qualitatively, if not quantitatively, from the real part of the cross-spectrum between the wind stress and the drifter ageostrophic velocities. This energy estimate is important as a potential contributor to the upper ocean mixing energy budget.

1.2 The Ekman layer and the mixing at the surface in the Southern Ocean

As mentioned above, the Southern Ocean is believed to be a primary location of ocean mixing and wind energy input, of relevance for the global oceanic circulation (Wunsch and Ferrari, 2004). More specifically, the magnitude of the mixing in the Southern Ocean has been shown to be critical in numerical process studies (Toggweiler and Samuels, 1998), and this implies that unless we have observations from this region to constrain general circulation models, mixing processes there could be incorrectly represented (Large et al., 1997).

Estimating the “mixing” could consist of obtaining a mixing coefficient that models the unresolved physical processes that redistribute quantities in space. In the ocean these quantities are scalars like temperature, salinity, mass, and other tracers or vectors like momentum. Starting from a set of observations of an ocean quantity ϕ, oceanographers attempt to estimate a turbulent or "eddy" coefficient:

$$K_\phi = \frac{\text{flux of } \phi}{\text{gradient of } \phi}. \tag{1.2}$$

This assumes that turbulent fluxes of tracers and momentum are down-gradient, following a Fickian law akin to what occurs at the molecular level. K_ϕ varies depending of course on the actual physical quantity ϕ, the spatial scales on which these properties are measured, and the direction along which they are measured with respect to an iso-surface.

In the Southern Ocean, mixing of deep water increases the potential energy that was lost when the water sank in northern high latitudes. When the water upwells, in the ACC, it closes the deep cell of the meridional circulation. A number of recent studies have evaluated Southern Ocean mixing. In Drake Passage and downstream of it, Naveira Garabato et al. (2004) estimated widespread and intense diapycnal diffusivities linkable to topographic roughness, from observed vertical profiles of ocean properties and velocities. Using standard hydrographic data, Sloyan (2005) found that mixing along the ACC was heterogeneous in the vertical and the horizontal directions, with enhancements in frontal regions and above rough topography. Further up in the water column, from approximately 1000 to 100 m of the surface, Thompson et al. (2006) estimated diapycnal diffusivities from expendable CTD hydrographic data in Drake Passage and noted a surface intensification for the diffusivity north of the Polar Front, with seasonal variability that they suspected was linked to wind stress variance. Cisewski et al. (2005) estimated the vertical diffusivity in the upper 180 m of a mesoscale eddy within the Antarctic Polar Frontal Zone using CTD and ADCP data. They found values that ranged several orders of magnitude, from O(10^{-4} m^2 s^{-1}) in the pycnocline up to O(10^{-1} m^2 s^{-1}) in the mixed-layer during strong wind events.

The same turbulent phenomena could be mixing both temperature and momentum but at different rates and on different scales. The value of the turbulent Prandtl number, the ratio of the momentum to the heat diffusivities is usually found to be approximately 1 in neutral environments (Kundu and Cohen, 2002), but how can we be sure that this is applicable in the world ocean? While diffusivity is the term commonly used for temperature, salinity and mass, the term viscosity is used for momentum. The adjective diapycnal is used for fluxes perpendicular to iso-density surfaces while the adjective isopycnal for fluxes along these surfaces. For the viscosity and diffusivity that enter the equations of motion in a three-dimensional Cartesian coordinate frame, K takes values that differ by several orders of magnitude for its vertical and horizontal counterparts. How do these various K relate to each other? As an example, in the zonally-averaged conceptual picture of the Southern Ocean, historical hydrographic data show that isopycnals are horizontal to the north and curve upwards to the south to become vertical when reaching the surface (e.g. Orsi and Whitworth, 2004) and this has implication for the mixing schemes of eddy fluxes implemented in oceanic general circulation models (OGCMs) (Ferrari and McWilliams, 2006). The vertical viscosity K must vary from values closer to the surface determined by an oceanic boundary layer (OBL) model, to interior values that are usually ascribable to the background internal wave field. This is the approach used in the K-Profile Parameterization (KPP) by Large et al. (1994), implemented commonly in OGCMs, where a cubic vertical profile for K is made to match smoothly a background value at the bottom of the OBL.

In Chapter 4 of this dissertation, estimates of the vertical viscosity and boundary layer depth are obtained by identifying the wind-driven processes taking place at the ocean-atmosphere interface and studying the ocean frequency response to wind stress forcing, using surface drifter velocity data in the Southern Ocean. It is beyond the scope of this study but potentially of interest to compare the values for the vertical viscosities and boundary layer depth obtained here to what is determined by the KPP algorithm in neutral or stable conditions in an OGCM run for the Southern Ocean. One objective of Chapter 4 is to assess realistic values for momentum diffusivities that can be compared with recent heat or buoyancy diffusivity estimates.

Chapter 2

Data and spectral methods

In this chapter, we review the datasets used for this work and discuss in detail the results from the spectral and cross-spectral analyses.

2.1 Data selection

The Surface Velocity Program (SVP) (Siedler et al., 2001) and the ongoing Global Drifter Program (GDP) both provide horizontal velocity data from surface drifting buoys (drifters) on a global scale. A SVP drifter has a Holey-Sock drogue centered at 15-m depth, linked by a tether to a subsurface float and a surface float that radio-transmits its positions to the ARGOS satellite array at an uneven time rate, depending on satellite coverage and the drifter's setup (Sybrandy and Niiler, 1991; Niiler et al., 1995). The NOAA Atlantic Oceanographic and Meteorological Laboratory (AOML) processes the raw position data and interpolates them using a kriging procedure (Hansen and Poulain, 1996), resulting in a time series of velocity $\mathbf{u}_d(t, \mathbf{x}(t))$ and position $\mathbf{x}(t)$ at a six-hour intervals. Positioning uncertainties cause a 1 cm s^{-1} inaccuracy in daily drifter velocities.

In principle, the drifter motions represent the currents averaged over the 6.1 m length of the drogue. Vertical shear of velocity has been observed over this vertical extent from vector measuring current meters mounted at the top and the bottom of the drogue (Niiler et al., 1995). Here this information is unavailable and we interpret the drifter velocities to be at the nominal 15 m depth when comparing to the theoretical transfer functions, which are explicitly a function of depth (see section 3.2.3).

In the Southern Ocean between 30°S and 60°S, 2,839 independent SVP drogued drifter trajectories are available from November 1989 to May 2003. Undrogued drifter data were discarded. We identified 666 trajectories from drogued drifters that were at least 40 days long between October 1992, the first date for which AVISO altimetric maps are available (see below), to August 2002, the date when the ECMWF ERA-40 re-analysis ends (see below). The coastal areas are avoided by discarding the points of drifter trajectories for which a dynamic height relative to 3000 decibars from the 1° gridded historical atlas data by Gouretski and Jancke (1998) could not be interpolated linearly. When divided in 40-day long segments that overlap by 20 days, these trajectories provide 10,387 time series segments, shown in in Fig. 2.1. These segments are further sorted in 2° latitudinal bands according to their mean latitude and are plotted with different colors to distinguish these zonal bands. The number of segments per band is listed in Table 2.1. These numbers are used to evaluate the number of degrees of freedom for the spectral estimates, as explained in section A.2. Panel a of Fig. 2.2 reveals the latitudinal biases, due to the decrease in data segments south of 44°S. In panel b of this figure, the longitudinal distribution of the data segments indicates that the drifters are primarily from the Atlantic and Indian sectors of the Southern Ocean. The temporal distribution of the data segments (Fig. 2.3) suggests that the observations are weighted more heavily toward the second half of the decade but show little seasonal bias. The drifter dataset is also further divided into an austral winter subdataset (5,282 segments) and a summer subdataset (5,105 segments) to study the seasonal variability. The austral winter is taken to correspond to the months of April through September and the austral summer to the months of October through March. The nominal month of a 40-day trajectory segment is chosen here as the month of the median date of the segment.

It is hypothesized that the statistical characteristics of the flow in the ACC

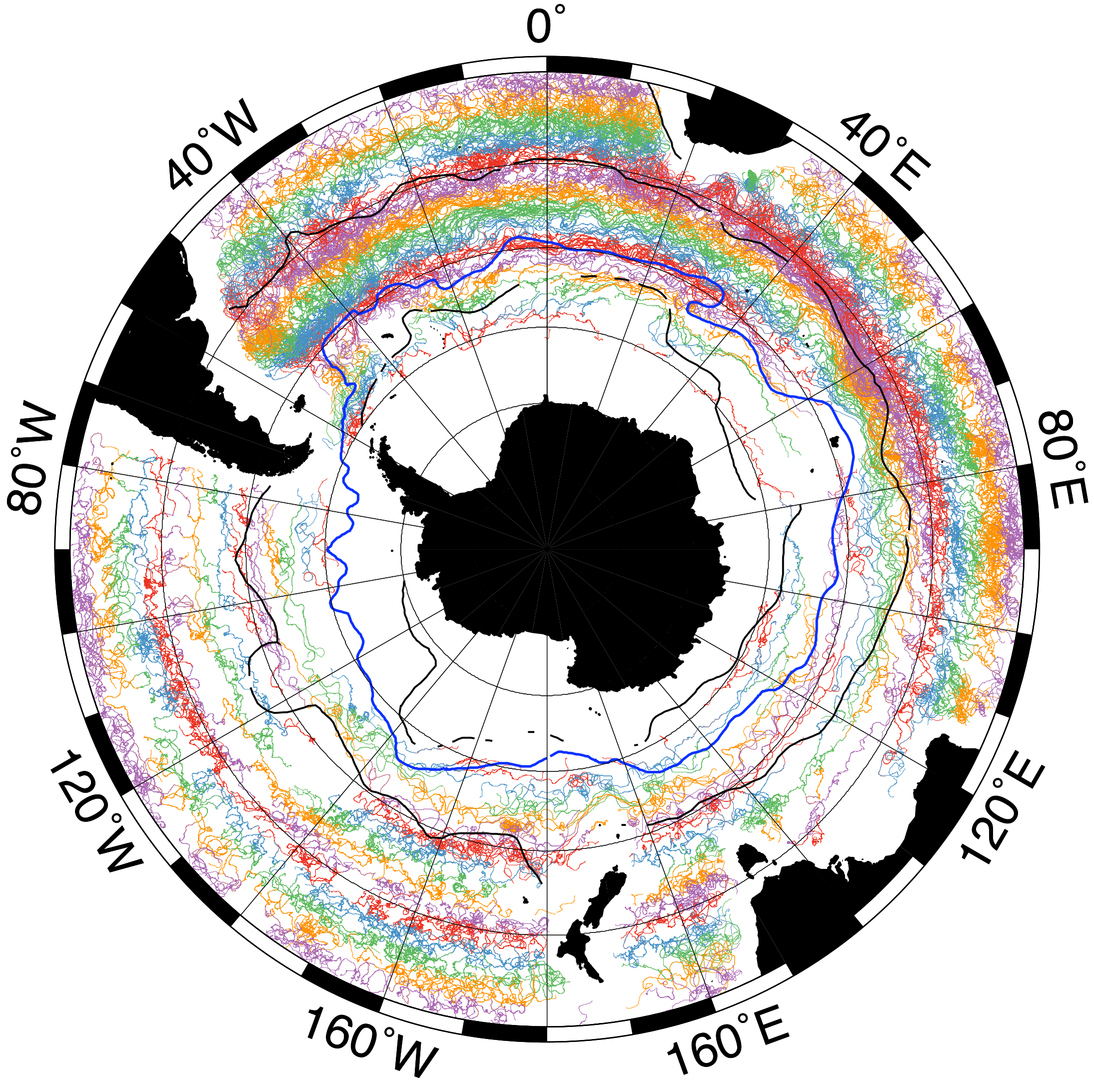

Figure 2.1: (a) Drifter trajectory segments used in this study between 30°S and 60°S. The 40-day segments are colored according to their mean latitude, following a repeated 5-class qualitative colormap to distinguish one 2° latitudinal band from the next. The solid blue line is the Polar Front position from Orsi et al. (1995). The 1 and 2.2 m dynamical height contours relative to 3000 decibars are drawn with black solid lines. These circumpolar contours delineate the ACC to the north and to the south.

Table 2.1: Characteristics of trajectory segments per 2°latitudinal band and in the ACC. The constant time lag is discussed in sections 2.3.2 and 4.2.2. $\chi(0)$ is the mean angle with the wind stress for drifter velocities $\mathbf{u}_d$ and ageostrophic velocities $\mathbf{u}$.

Latitudes	Number of segments			Lag (°cpd^{-1})	$\chi(0)$ (°)	
	all	summer	winter		$\mathbf{u}_d$	$\mathbf{u}$
30-32°S	723	361	362	41.53	42.58	46.13
32-34°S	1080	570	510	48.36	29.45	37.88
34-36°S	1124	587	537	39.01	28.68	35.69
36-38°S	1045	525	520	36.43	27.85	33.86
38-40°S	1076	505	571	37.95	20.09	27.24
40-42°S	1172	569	603	34.77	16.87	33.18
42-44°S	1019	542	477	29.68	15.30	39.68
44-46°S	848	397	451	27.82	17.23	33.31
46-48°S	622	279	343	28.26	17.59	34.17
48-50°S	543	261	282	22.56	16.88	27.80
50-52°S	363	167	196	26.63	15.83	25.80
52-54°S	279	105	174	23.54	21.32	35.29
54-56°S	222	118	104	30.81	16.44	28.44
56-58°S	143	65	78	29.93	17.71	26.71
58-60°S	128	54	74	21.23	16.11	23.48
Total	10387	5105	5282	-	-	-
ACC	3528	1689	1839	28.07	16.04	31.74

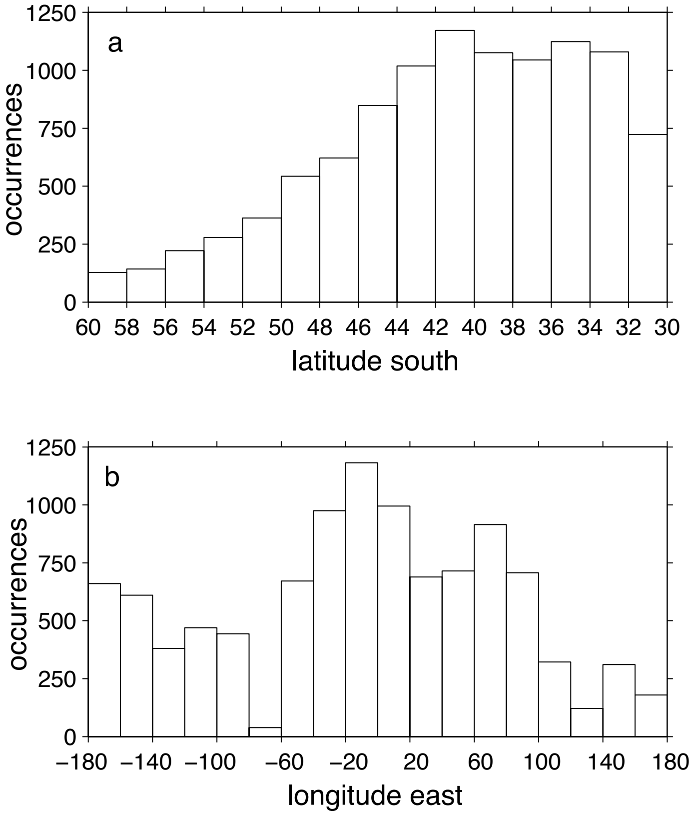

Figure 2.2: (a) Latitudinal distribution and (b) longitudinal distribution of the median dates of the of the 20-day overlapping 40-day drifter trajectory segments.

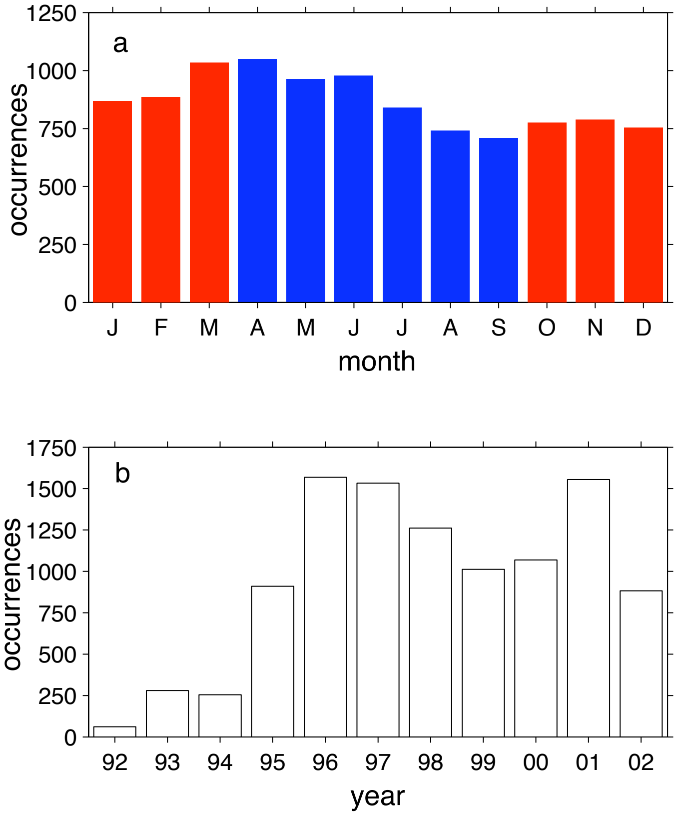

Figure 2.3: (a) Month distribution of the median dates, and (b) year distribution of the mean latitude of the 20-day overlapping 40-day drifter trajectory segments used in this study. In (a), the red indicates the austral summer season and blue the winter season.

should differ from the subtropics and that circumpolar streamlines could be controlled by different forcing than non-circumpolar streamlines in the subtropical gyres (Mestas-Nuñez et al., 1992). As such, a subdataset for the ACC is constituted by selecting the 3,528 segments south of 40°S and between the 1 and 2.2 m dynamic height contours relative to 3000 decibars (e.g. Pond and Pickard, 1983), which we calculated from 1° gridded historical atlas data (Gouretski and Jancke, 1998).

In order to obtain an estimate of the absolute geostrophic velocity component of the drifter velocities, two satellite altimetry datasets were combined. The anomalies $\mathbf{u}'_g$ were derived from "Archiving, Validation and Interpretation of Satellite Oceanographic" data that are produced by the Centre Localisation Satellite (AVISO). These provide high-resolution maps ($1/3^\circ \times 1/3^\circ$ Mercator grid) by merging TOPEX/Poseidon (T/P) and ERS-1 and -2 altimeter measurements, using an objective analysis method (Ducet et al., 2000). These maps are available at 7-day intervals implying a Nyquist frequency of 1/14 cpd, which is the highest frequency that one can hope to resolve in the geostrophic signal. We computed the velocity anomalies from the zonal and meridional gradients of the height anomalies. To these, a mean geostrophic velocity $\bar{\mathbf{u}}_g$ was added, computed from the Gravity Recovery and Climate Experiment (GRACE) satellite-derived dynamic topography available on a global 1° grid (Tapley et al., 2005). This mean geostrophic velocity field was interpolated linearly in space, and the velocity anomaly maps were linearly interpolated in space and time, at all the drifter positions, to obtain the absolute geostrophic velocity $\mathbf{u}'_g + \bar{\mathbf{u}}_g$ at the surface every 6-hours along the drifter trajectories. In the coherence analysis (section 2.3) it is shown that adding a mean velocity permits us to resolve some of the geostrophic velocity variance at zero and low frequencies.

The ageostrophic velocity $\mathbf{u}$ at 15 meters at the location $\mathbf{x}_0$ is then obtained as the drifter velocity minus the absolute geostrophic velocity at the surface:

$$\mathbf{u}(t) = \mathbf{u}_d\,(t, \mathbf{x}(t) = \mathbf{x}_0) - (\mathbf{u}'{}_g\,(t, \mathbf{x}_0) + \bar{\mathbf{u}}_g(\mathbf{x}_0)). \tag{2.1}$$

This neglects the geostrophic shear in the upper 15 meters of the ocean. Expendable bathythermograph data in the Drake Passage indicate a geostrophic shear of less than 10^{-3} s^{-1} in the upper 400 meters (Janet Sprintall, personal communication), yielding a potential maximum 1.5 cm s^{-1} geostrophic velocity difference between the surface and 15 meters. This is of the same order as other sources of noise in this study.

For the wind data, the chosen product is the European Center for Medium-Range Weather Forecasts (ECMWF) ERA-40 Project re-analysis wind stresses (Simmons and Gibson, 2000) obtained from the Data Support Section of the Scientific Computing Division at the National Center for Atmospheric Research. The zonal and meridional wind stress components are available four times daily at the times 00, 06,12 and 18 UTC. The values are instantaneous and are given as forecasts valid 6 hours after the re-analysis time. This detail will appear to be crucial for the interpretation of the phase of the cross-spectra (see section 2.3.2). The data are released on a Gaussian grid with resolution of 1.125° longitude by roughly 1.125° latitude. These grids were linearly interpolated on the drifter positions to obtain contemporaneous six-hourly time series of wind stress.

2.2 Power rotary spectra of wind stress and ocean velocity

2.2.1 Rotary spectral decomposition

For this study, time series of vector quantities are analyzed. A vector time series of temporal length $\mathcal{T}$ (here of the wind stress, drifter velocity or ageostrophic velocity) can be written as a complex quantity. Such a time series can be assumed to have a complex Fourier series representation and be written [1]:

$$\mathbf{u}(t) = u(t) + iv(t) = \sum_{k=-\infty}^{k=+\infty} \mathbf{u}_k(t), \tag{2.2}$$

---

[1] Formally the assumption is that the times series are periodic of period $\mathcal{T}$. The usual approach is to assume that the real time series coincides with an idealistic periodic time series over a time window $\mathcal{T}$.

where u and v are the zonal and meridional components, respectively; t is the time, and $i = \sqrt{-1}$. At each discrete frequency $\nu_k = k/\mathcal{T}$, the rotary component is

$$\mathbf{u}_k(t) = \mathbf{C}_k \exp(i2\pi\nu_k t), \tag{2.3}$$

with

$$\mathbf{C}_k(\nu_k) = \frac{1}{\mathcal{T}} \int_0^{\mathcal{T}} \mathbf{u}(t) \exp(-i2\pi\nu_k t) dt, \tag{2.4}$$

which is the complex Fourier series coefficient. Each component represents a rotating vector component of the original vector time series, the hodograph of which is a circle described in the sense given by the frequency sign. The absolute value and phase of $\mathbf{C}_k$ give the magnitude and angle at the time origin of each rotary component. Fig. 2.4 gives a graphical representation of rotary components at opposite frequencies.

The generalization of the complex Fourier series representation to stationary complex random variables constitutes the rotary spectral analysis. A rotary spectrum decomposes a vector signal into clockwise and counterclockwise rotary spectral components continuously as a function of frequency. This type of analysis can reveal polarized oscillatory movements characteristic of geophysical fluids and was introduced by Gonella (1972) and Mooers (1973) in oceanography. For this study, negative frequencies correspond to clockwise motions, cyclonic in the Southern Hemisphere. As such, the anticyclonic inertial frequency is $-f/2\pi > 0$.

Rotary power spectral density functions $S_{\mathbf{yx}}(\nu)$, functions of the frequency ν of the motions, are estimated for this study by the periodogram (e.g. Bendat and Piersol, 1986), for a finite number of frequency bands ν_k:

$$\hat{S}_{\mathbf{yx}}(\nu_k) = \frac{\langle \mathbf{Y}_k \, \mathbf{X}_k{}^* \rangle}{\mathcal{T}}, \tag{2.5}$$

where $\langle \cdot \rangle$ is the expected value operation over an ensemble of time series segments and $.^*$ is the complex conjugate. $\mathbf{X}_k$ is the finite Fourier transform of $\mathbf{x}$, computed over the finite time $\mathcal{T}$:

$$\mathbf{X}_k(\nu_k) = \int_0^{\mathcal{T}} \mathbf{x}(t) \exp(-i2\pi\nu_k t) dt. \tag{2.6}$$

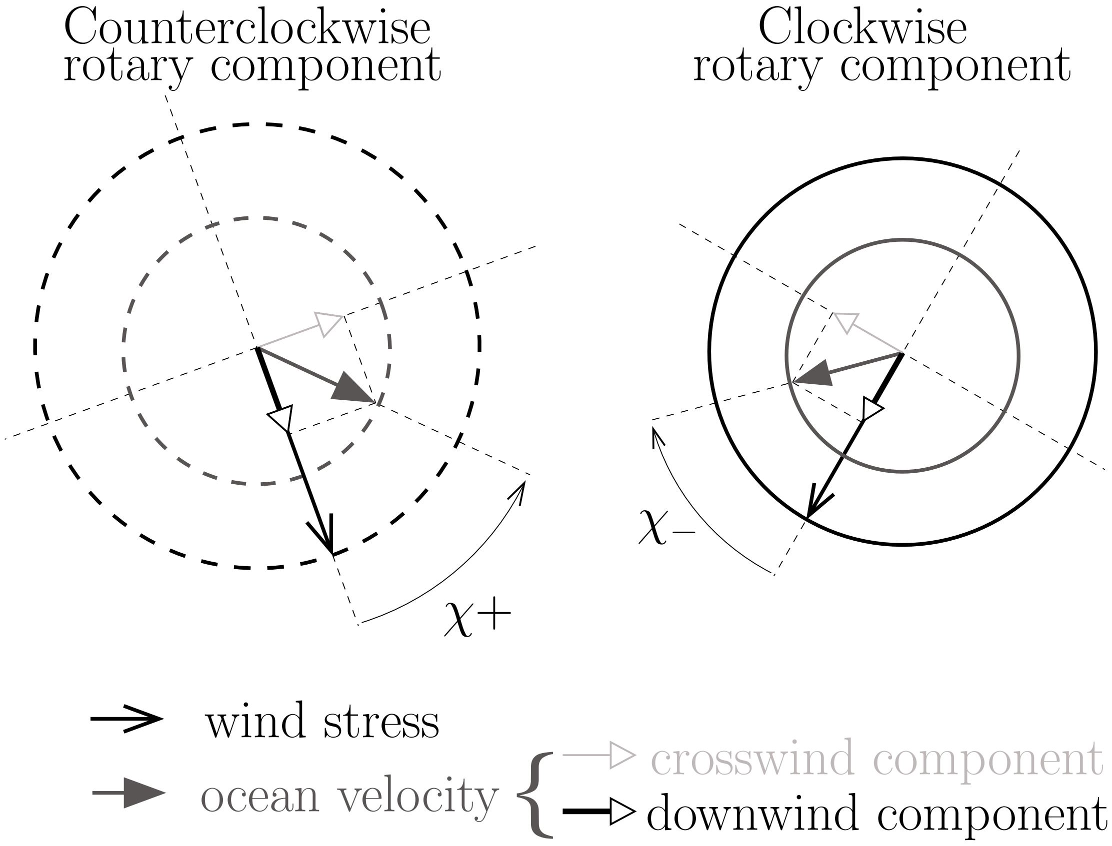

Figure 2.4: Sketch of rotary Fourier series components. The circles are the hodographs described during one time period by the rotary Fourier components of the wind stress (black) and of the ocean velocity (gray), for counterclockwise components (dashed circles) and clockwise components (solid lines). For random variables, the radius of these circles are representative of the power spectral density at the corresponding frequency. When considering pairs of coherent variables, as an example the wind stresses and the ocean velocities, the coherence phase $\chi\pm$ is the constant angle between two co-rotating components. The black (light gray) triangle arrow vector is the ocean velocity rotary component representative of the magnitude of the co-spectrum (quad-spectrum).

The finite Fourier transform is computed using a standard Fast Fourier Transform algorithm.

Since the drifter trajectories in the Southern Ocean are $\mathcal{T} = 40$ days with a sampling interval Δt =0.25 day, the formal Nyquist frequency is $1/(2\Delta t) = 2$ cycles per day (cpd), and the frequency bands considered are given by $\nu_k = k/\mathcal{T} = k/(N\Delta t)$, positive for $k = 0, \ldots, N/2$ and negative for $k = -N/2 + 1, \ldots, 0$, with $N = 160$. The frequency resolution, or bandwidth, is theoretically $\nu_r = 1/\mathcal{T}$ =0.025 cpd, but in reality it is 50$\%$ larger at 0.0375 cpd, because we applied a Hanning window to reduce spectral side-lobe leakage (Harris, 1978). Since the drifter data were ultimately sorted in 2°-latitudinal bands between 30°S and 60°S, this frequency resolution is sufficient to resolve the smallest difference in the inertial frequency from one 2°-latitudinal band to the next, except between the two most southern bands.

For this type of ensemble-averaging method for spectral estimation, it is usually recommended to subtract the mean value of each realization (Bendat and Piersol, 1986), in order to remove the bias or influence of any signal occurring at a lower frequency than ν_r. This procedure is applied in this chapter for the estimation of the autospectra of the wind stress and of the ocean velocity in the next section, as well as for the estimation of the coherence squared in section 2.3. In Chapter 3, for the purpose of estimating the wind energy input rate into the Ekman layer, it will be shown that the estimation of this mean is crucial and does carry an important physical meaning. In Chapter 4, for the purpose of estimating the transfer function, it will be seen that the zero frequency component is representative of the mean Ekman currents and should be kept as well. Table 2.1 lists for each latitudinal band the phase at zero frequency of the cross-spectrum between the wind stress and the drifter velocity, as well as between the wind stress and the drifter ageostrophic velocity, for which the mean was not subtracted.

2.2.2 Analyses of the instrumental noise spectrum

A variety of sources of noise may alter the spectral estimates. We focus on the noise in the drifter data, since ECMWF does not provide formal error estimates with the re-analysis wind fields. For the drifter velocities, three sources of "instrumental" error are considered. The first is the uncertainty in the ARGOS drifter positioning, which leads to velocity errors of about 1 cm s^{-1} (Niiler et al., 1995). The resulting noise velocity spectrum follows a quadratic law (Rupolo et al., 1996) and becomes greater than the velocity spectrum only at very high frequencies ($|\nu| \geq 1.8$ cpd), but its power density remains below 10^{-4} m^2 s^{-2} cpd^{-1}. The second source of error is the "wind-slip" or direct action of the wind on the drifter surface buoy which results in an erroneous downwind component in the ocean current velocity (see also section 3.2.3). Niiler et al. (1995) estimated the wind slip to be a linear function of the 10-m wind velocity. For standard SVP drifters they predicted about 1 cm s^{-1} slip for winds of 10 m s^{-1}, a scale factor of 10^{-3}. Assuming that the wind slip spectrum is correspondingly proportional to the 10-m wind spectrum (not shown), the wind slip should have a maximum power density of about 10^{-4} m^2 s^{-2} cpd^{-1}. Another error in the ocean velocities comes from a slippage proportional to the velocity shear across the length of the drogue (Chereskin et al., 1989). On the basis of the data tabulated by Niiler et al. (1995), we estimated that in the worst case, shear slippage would be of the order of the wind slip. Thus, for the purpose of spectral estimation, we combine the effect of wind and shear slips and assume the maximum slippage noise to have a power spectral density of 2×10^{-4} m^2 s^{-2} cpd^{-1}.

2.2.3 Spectral analyses

The spectral analysis in this work aims at studying the relationship between the wind stress and the ocean surface velocity in the Southern Ocean. In the remainder of this chapter, we focus on the ACC subset of the drifter dataset in the Southern Ocean. Since the number of trajectory segments in the ACC is much larger than in any 2° latitudinal band across the Southern Ocean, the spectral estimates are smoother and the error bars are smaller. However, it is found that the spectral characteristics discussed in this chapter are qualitatively similar all across the Southern Ocean.

The rotary autospectral density functions for the wind stresses, the drifter velocities and the ageostrophic velocities from the ACC sub-dataset are plotted in Fig. 2.5.

2.2.3.1 Wind stress spectra

The wind stress rotary autospectrum $S_{\boldsymbol{\tau}\boldsymbol{\tau}}$ (heavy black lines in Fig. 2.5) should be interpreted with care. These estimates do not formally represent Lagrangian spectra since they are not derived from material trajectories, but instead represent the wind stress forcing at drifter locations and measurement times. They show that anticyclonic power density (dashed curves) is higher than cyclonic power density (solid curves) for all frequencies considered. The maximum anticyclonic polarization is found for $\nu = 0.525$ cpd or a period of 1.9 days. The anticyclonic and cyclonic spectra have the same red shape with an attenuation of about 10 dB per frequency decade. Rio and Hernandez (2003), who interpolated ECMWF analysis wind stresses onto global SVP drifter positions found similar features in their wind stress spectral estimates. Similarly, Stockwell et al. (2004) found that the anticyclonic power exceeds the cyclonic power in spectra from moored buoy surface winds on an almost global scale.

Spectral slopes were computed by a least-square fitting procedure, using the error bar of the spectra to deduce 95$\%$ confidence intervals for the slopes. Spectral slopes of the anticyclonic and cyclonic domains were not statistically different and were averaged to obtain the overall slope estimates, listed in Table 2.2. The wind stress indicates several regimes: slopes are near zero at low frequencies, around 0.5 ($\mathrm{k_{sl}}$) from $\nu = 0.05$ to 0.325 cpd, and steepen to around 2.25 ($\mathrm{k_{sh}}$) from ν =0.5 to 1.5 cpd. These values agree with slope estimates from Eulerian zonal and meridional wind stress frequency spectra for ECMWF analyses (Gille, 2005). This is not surprising given that

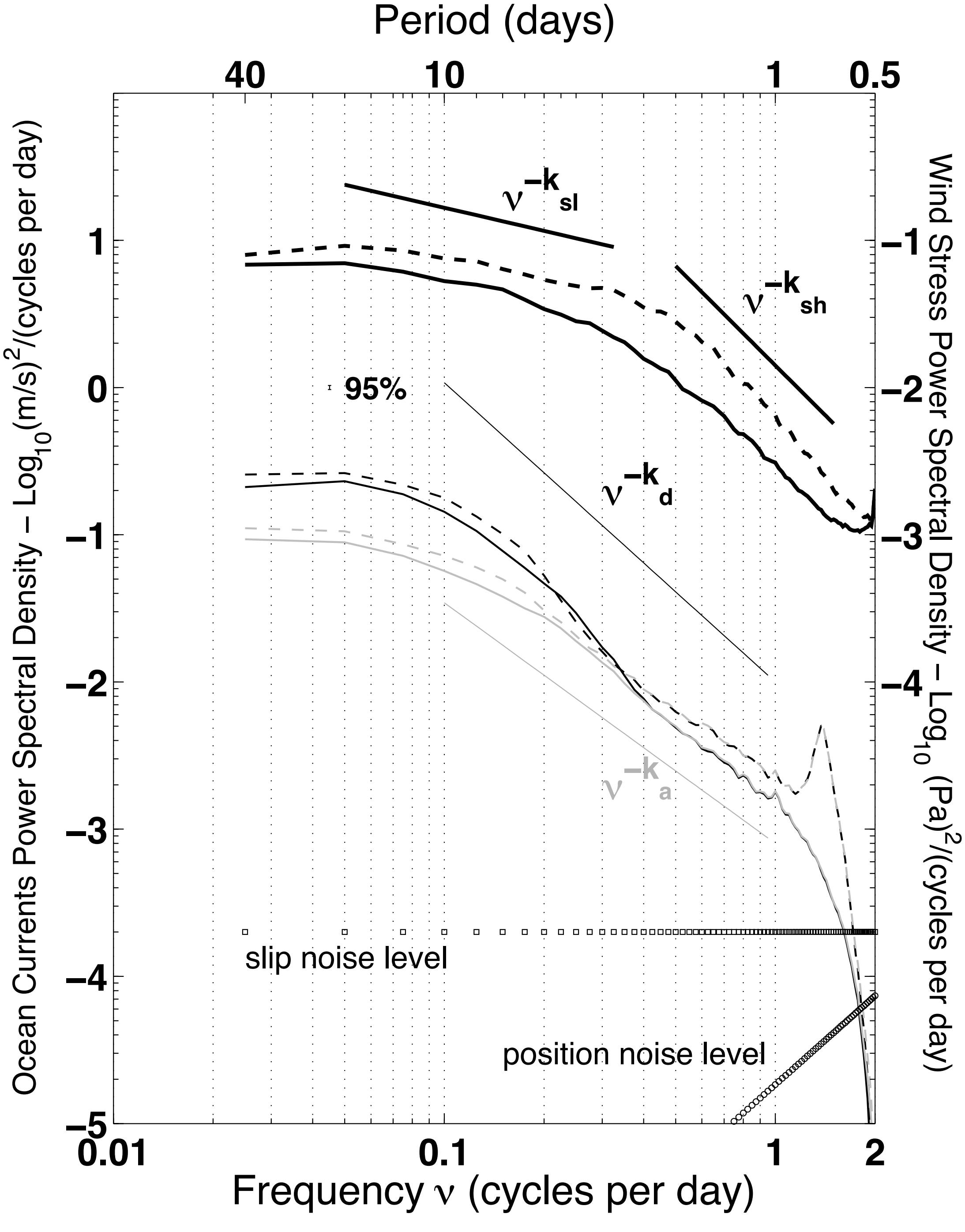

Figure 2.5: Rotary power spectral density functions of stresses (heavy black curves) with ordinate axis to the right, drifter velocities (thin black curves) and ageostrophic velocities (thin gray curves) with ordinate axis to the left. Solid curves correspond to cyclonic motions and dashed curves to anticyclonic motions. Slope magnitude estimates are listed in Table 2.2. The error bar is the formal 95% confidence interval for autospectral estimates.

Table 2.2: Spectral slopes of Fig. 2.5. Error bars are the 95% confidence intervals determined from the least-square estimates

Spectrum	Slope $\nu^{\text{-k}}$
Drifter velocities	$\mathrm{k_d} = 2.03 \pm 0.02$
Ageostrophic velocities	$\mathrm{k_a} = 1.63 \pm 0.02$
Low frequency stress	$\mathrm{k_{sl}} = 0.52 \pm 0.03$
High frequency stress	$\mathrm{k_{sh}} = 2.25 \pm 0.05$

winds have larger spatial scales than do ocean flows and therefore are relatively spatially homogeneous along the 40-day trajectories of the drifters.

2.2.3.2 Ocean velocity spectra

The Lagrangian rotary autospectrum $S_{\mathbf{u}_d \mathbf{u}_d}$ of the drifter velocities is indicated with thin black lines in Fig. 2.5. Both anticyclonic and cyclonic spectra display a plateau at low frequencies below about 0.1 cpd. As frequency increases, they follow a power law intermediate regime up to about 1.2 cpd. The anticyclonic spectrum then differs greatly from the cyclonic spectrum with a peak at about 1.45 cpd. This peak, which has been previously reported in drifter data, corresponds to near-inertial motions in the ocean mixed layer (e.g Poulain, 1990; Poulain et al., 1992; Saji et al., 2000). The so-called inertial peak is broad, extending from about 1.2 to 1.8 cpd because of the latitudinal distribution of the ACC data selected for this plot and because of the latitudinal displacement during each 40-day trajectory segment. In contrast with the wind stress spectra, for the drifters the polarization is less pronounced and varies in sign. Anticyclonic power predominates for all frequencies except from $\nu = 0.2$ to 0.375 cpd. There the polarization is not statistically significant (i.e. the difference between the cyclonic and anticyclonic spectra is less than the 95% confidence interval) except at $\nu = 0.25$ cpd, where it is marginally cyclonic. We further tested the statistics of this polarization reversal by applying a bootstrapping method (Efron and Gong, 1983) to recompute the drifter spectra a hundred times. Our findings indicate that this is a robust feature since cyclonic polarization is found in at least one frequency band between $\nu = 0.225$ and $\nu = 0.325$ cpd in 95% of the cases. Similarly, Colin De Verdière (1983) observed an anticyclonic polarization of Lagrangian spectra at low frequencies from 14 drifters drogued to 100 meters in the eastern North Atlantic. In contrast, from SVP drifter data, Lumpkin and Flament (2001) found polarizations of either sign in the wake of the Hawaiian archipelago in the North Equatorial Current. They ascribed these features to the cyclonic and anticyclonic vorticity of the respective gyres that transported the drifters. Here, ascribing the polarization to local flow features is difficult since we are using data collected all along the ACC.

The ageostrophic velocities $\mathbf{u}$ (Eq. 2.1) were used to compute the ageostrophic rotary autospectrum $S_{\mathbf{uu}}$ (gray lines in Fig 2.5). For $|\nu| < 0.1$ cpd, the power density of ageostrophic velocities is about 40% of the drifter velocities. This suggests that at low frequencies, the geostrophic component dominates the drifter velocities. For $|\nu| \geq 0.3$ cpd, the ageostrophic and drifter velocity spectra are identical. The ageostrophic velocities are polarized anticyclonically at all frequencies, except from $|\nu| = 0.2$ cpd to 0.35 cpd. In this range, in contrast with the drifter velocities, the polarization is not statistically different from zero anywhere. This suggests that the aforementioned cyclonic power in the drifter velocities can be ascribed to the geostrophic component of the velocities. This polarization might occur because drifters preferentially sample regions of convergence, where quasigeostrophic motions have cyclonic vorticity (e.g. Middleton and Garrett, 1986). In contrast, the anticyclonic polarization is explained by the stronger anticyclonic wind forcing and by a preferential response of the wind-driven upper ocean to anticyclonic wind stress (Gonella, 1972), as discussed in Chapter 4.

2.2.4 What sets the ocean spectral slope?

For the drifter and ageostrophic spectra, slopes were estimated for the frequency range between 0.1 and 1 cpd, where a power law decay is observed. Results are listed in Table 2.2. The drifter spectra display a slope $\mathrm{k_d} = 2.03 \pm 0.02$ while the ageostrophic spectra have a smaller slope $\mathrm{k_a} = 1.63 \pm 0.02$, as a result of reduced power at low frequencies. Our choice of data processing also affects the slope estimates. In the high-frequency range, spectral leakage from the inertial peak certainly occurs, and without windowing to reduce this effect, the slopes are reduced by about 15%. Applying the Niiler et al. (1995) wind slip correction did not modify the spectral slope estimates significantly.

Spectral slopes carry information about the physics governing variability. First, spectral slopes can be controlled by turbulent variability: power laws are expected in the inertial subrange. Kolmogorov's similarity theory predicts that wavenumber k spectra should scale as $k^{-5/3}$ whereas frequency spectra should scale as ν^{-2} (Pinton and Labbé, 1994). In addition, in geostrophic turbulence, energy is transfered towards larger scales from one spectral band to the next with no energy input from outside forcing. Such free decay should also give rise to a power law regime. Turbulence theories are therefore compatible with our slope $\mathrm{k_d}$ for the drifter spectra, as some previous Lagrangian studies have also found. Rupolo et al. (1996) identified from 700-m float trajectories in the North Atlantic a three-piece shaped typical power spectrum for which a plateau at low frequency is followed by an intermediate power law regime with a small slope ($\approx \nu^{-0.25}$) and finally a power law regime with steep slope (> 3). They suggested that slopes greater than 2 may be due to the Lagrangian nature of the frequency spectra in contrast to Eulerian spectra which have longer decorrelation time scales. In spectra computed from three drifters drogued to 100 meters in the Kuroshio region, Osborne et al. (1989) found a power law regime with a $\nu^{-2.5}$ slope that they interpreted as a manifestation of the inertial range of geostrophic turbulence.

Second, specific ocean features can alter or modify spectral slopes. Rupolo et al. (1996) linked their intermediate power law regime to their floats' sampling of energetic features like jets or vortices. In computations based on SVP drifters around Hawaii, Lumpkin and Flament (2001) found slopes between ν^{-1} and ν^{-3} in the approximate $(40)^{-1}$ to 1 cpd frequency range. They also ascribed these anomalous slopes to the coherent vortices in the flow. This is reminiscent of the slight bulge in the shape of our spectra in the 0.2 to 0.375 cpd frequency bands, which changes the polarization of the drifter velocity spectrum and that we suggested was due predominantly to mesoscale geostrophic cyclonic motions.

Finally, external forcing influences spectra. Hasselmann (1976) noted that the ocean integrates high-frequency wind variations, and therefore the ocean velocity spectral slope is expected to be steeper than the forcing slope (e.g. Colin De Verdière, 1983). Such a regime is found in our drifter and ageostrophic spectra for which $\mathrm{k_a}$ and $\mathrm{k_d}$ are greater than $\mathrm{k_{sl}}$, the spectral slope of the wind stress forcing at low frequencies. This stochastic interpretation fails toward higher frequencies as the wind stress slope steepens and becomes greater than the ocean velocity slope. This may be due to a lack of high-frequency power in the ECMWF re-analysis wind stress fields.

The ocean spectral slopes therefore appear to represent a combination of intrinsic variability and wind stress forcing, and a simple spectral slope analysis is inconclusive. The surface currents in the Southern Ocean do not mirror the local wind stress forcing but the common anticyclonic polarization of the wind stress forcing and of the ageostrophic spectra suggests a relationship between these two. The cross-spectral analysis of the next section as well as the study of the transfer function in Chapter 4 elucidates this relationship.

2.3 The linear relationship from the coherence

What fraction of the drifter or ageostrophic spectra in Fig. 2.5 can be attributed to local wind stress forcing? Rotary cross-spectral analysis allows us to study the relationship between the pairs of vector time series of the local wind stresses $\boldsymbol{\tau}$ and the drifter or ageostrophic velocities $\mathbf{u}$. Gonella (1972) and Mooers (1973) developed these vector time series cross-spectral analysis techniques and pioneered their application to meteorological and oceanographic data. Table 2.3 reviews results from previous Lagrangian studies. Details in these results diverge for a variety of reasons associated

Table 2.3: Cross-spectral analyses results from selected Lagrangian studies. The frequency ranges indicates ranges for which γ^2 is statistically significant at the 95% confidence level when available. $\nu > 0$ corresponds to anticyclonic frequencies, and the values for the phase, χ, are for the corresponding frequency ranges. Error bars for χ are given when available.

	Data	Frequency range (cpd)	χ
Daniault et al. (1985)			
	single Marisonde G surface buoy velocities and winds	$\mid\nu\mid < \mid f/2\pi\mid$[a]	scattered values
McNally et al. (1989)[b]			
	30-m drifters, FNOC[c] winds		
	summer data	$(16)^{-1} < \mid\nu\mid < (2.65)^{-1}$	unreliable
	winter data	$(16)^{-1} < \mid\nu\mid < 1$	$15° < \mid\chi\mid < 110° \pm 13°$
Niiler and Paduan (1995)			
	15-m Holey-Sock and TRISTAR drifters, ECMWF winds converted to stress	$(20)^{-1} < \mid\nu\mid < (5)^{-1}$	$60° < \mid\chi\mid < 100°$
Rio and Hernandez (2003)[d]			
	SVP drifters, ECMWF wind stress analyses		
	$3° <$ latitude $< 15°$	$\mid\nu\mid < (10)^{-1}$	$30° < \mid\chi\mid < 60°$
	$15° <$ latitude $< 30°$	$-(10)^{-1} < \nu < 1$	$30° < \mid\chi\mid < 60°$
	latitude $> 30°$	$-(0.5)^{-1} < \nu < 1$	$30° < \mid\chi\mid < 60°$

[a] Local inertial frequency. [b] Results taken from Fig. 6. of this study. [c] Fleet Numerical Ocean Center. [d] No statistical significance level for γ^2 is provided in this study

with differences in drifting buoy design and data processing, in oceanic or atmospheric conditions, and in the quality of wind stress data used. In contrast, the standardized SVP drifters used here are all expected to have the same water-following capabilities, whatever their location in the Southern Ocean. Moreover, the data span a decade and we expect that they represent the average response of the surface circulation in the Southern Ocean.

The rotary cross-spectral power density function $S_{\boldsymbol{\tau}\mathbf{u}}(\nu)$ between $\boldsymbol{\tau}$ and $\mathbf{u}$ was estimated. $S_{\boldsymbol{\tau}\mathbf{u}}(\nu)$ is a complex quantity that measures the covariance between the co-rotating rotary components of $\mathbf{u}$ and $\boldsymbol{\tau}$ as a function of frequency (e.g. Mooers, 1973) and consequently has the units of a spectral density of a momentum flux. A detailed interpretation of the meaning of the cross-spectrum is the focus of Chapter 3.

We first examined the coherence squared γ^2, which quantifies the linear relationship between two signals as a function of frequency:

$$\gamma^2(\nu) = \frac{|S_{\boldsymbol{\tau}\mathbf{u}}(\nu)|^2}{S_{\boldsymbol{\tau}\boldsymbol{\tau}(\nu)}S_{\mathbf{uu}}(\nu)}, \tag{2.7}$$

where $S_{\boldsymbol{\tau}\boldsymbol{\tau}}(\nu)$ and $S_{\mathbf{uu}}(\nu)$ are the autospectral power density functions of $\boldsymbol{\tau}$ and $\mathbf{u}$, respectively. One can interpret γ^2 as the percentage of variance of $\mathbf{u}$ that is ascribable to linear forcing by $\boldsymbol{\tau}$. γ^2 was estimated as

$$\widehat{\gamma^2}(\nu_k) = \frac{|\langle \mathbf{T}_k\,\mathbf{U}_k{}^*\rangle|^2}{\langle \mathbf{T}_k\,\mathbf{T}_k{}^*\rangle\,\langle \mathbf{U}_k\,\mathbf{U}_k{}^*\rangle}. \tag{2.8}$$

The phase of the cross-spectrum is,

$$\chi(\nu) = \arctan\left[\frac{\mathcal{I}\left(S_{\boldsymbol{\tau}\mathbf{u}}(\nu)\right)}{\mathcal{R}\left(S_{\boldsymbol{\tau}\mathbf{u}}(\nu)\right)}\right], \tag{2.9}$$

where $\mathcal{R}$ and $\mathcal{I}$ designate the real and imaginary parts, respectively. χ is interpreted as the geometric angle between the coherent components of the two quantities (Gonella, 1972), as shown schematically in Fig. 2.4. In this study a positive angle means that the coherent rotary component of $\mathbf{u}$ is to the left of the rotary component of $\boldsymbol{\tau}$.

Fig. 2.6a and b show γ^2 and χ for the wind stresses and the drifter velocities (black curves) and for the wind stress and the ageostrophic velocities (gray curves). The

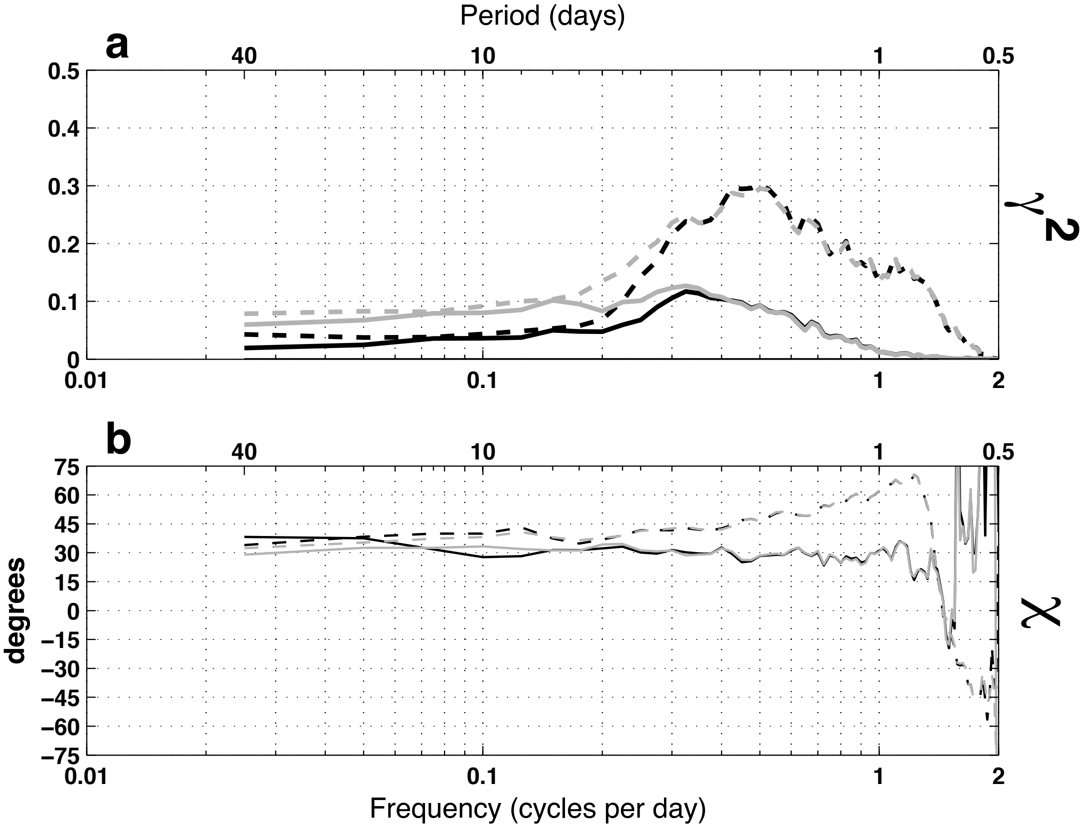

Figure 2.6: (a) Coherence squared γ^2 and (b) coherence phase χ between ECMWF stresses and drifter velocities (heavy black curves) or ageostrophic velocities (thin gray curves). Solid curves correspond to cyclonic frequencies and dashed curves to anticyclonic frequencies. The 95% confidence limit for γ^2 is indistinguishable from the 0 on this plot.

subset of data used to compute these estimates is the same as the one used to compute the spectral estimates of Fig. 2.5 and is expected to produce results representative of the ACC. The formal 95% confidence level (Bendat and Piersol, 1986) for γ^2 is 5×10^{-4}. For frequencies lower than 1 cpd, the average error bar for γ^2 is $\pm 10^{-3}$ and for χ it is $\pm 0.05°$. The large number of degrees of freedom make these error bars small and therefore not visible on the scales of these plots. From $|\nu| = 0$ to 0.15 cpd, the cross-spectra depend on the mean sea surface height product used. The influence of the mean field on non-zero frequencies is explained by the Lagrangian nature of the drifters, because advection by the mean field produces a low-frequency component in the velocity time series.

2.3.1 Coherence squared

Values of γ^2 shown in Fig. 2.6a are generally low (≤ 0.3) but well above the 95% confidence level for all frequencies except for the higher end of the inertial band. For all anticyclonic frequencies, γ^2 is significantly higher than for the corresponding cyclonic frequencies; since γ^2 is a normalized quantity, this means that the ocean surface responds preferentially to anticyclonic forcing. This polarized response was noted in previous studies but its statistical significance was not assessed (e.g. Gonella, 1972; Rio and Hernandez, 2003). A strict anticyclonic response is a classic result at near-inertial frequencies in the oceanic mixed layer (e.g. Gill, 1982, p.322); but a stronger anticyclonic response is predicted at all frequencies by extensions of the Ekman model developed by Gonella (1972). In these extended models, the response is largest at the inertial frequency located in the anticyclonic domain and decreases monotonically as the frequency is further away from the inertial frequency, resulting in a stronger anticyclonic response. The comparison between theoretical and observed transfer functions is discussed in details in Chapter 4.

The maximum value of γ^2 in the anticyclonic domain is 0.30 for $\nu = (2)^{-1}$ cpd. Since γ^2 measures the fraction of drifter variance explained by linear forcing of the wind stress, the results indicate that at this frequency the wind-driven currents explain roughly 30% of the anticyclonic variance of total drifter velocity in the ACC. For the corresponding cyclonic frequency $\nu = -(2)^{-1}$ cpd, γ^2 is much lower, at 0.09.

For frequencies higher and lower than this anticyclonic peak, γ^2 drops rapidly in both the cyclonic and anticyclonic domains. Niiler and Paduan (1995) interpreted the coherence peak as a trough in the noise spectrum. For the purposes of this study, any velocity component that is not linearly driven by local wind stress is assumed to be noise. Thus noise may include instrumental and nonlinear wind stress forcing effects, as well as other non wind-driven or turbulent velocities, all of which contribute to reduce γ^2.

2.3.1.1 Low frequencies: coherence squared between drifter and altimetric velocities

In order to evaluate the geostrophic velocities interpolated along the drifter trajectories, γ^2 was computed between the drifter velocities $\mathbf{u}_d$ and the geostrophic velocities from AVISO and GRACE measurements $(\mathbf{u}'_g + \bar{\mathbf{u}}_g)$ (see Eq. 2.1) and is plotted in (Fig. 2.7). The value of γ^2 is approximately 0.64 for cyclonic and anticyclonic frequencies that are resolved by both the drifter and altimeter datasets, i.e. $|\nu| < (14)^{-1}$ cpd. Interestingly, γ^2 remains high until about $|\nu| = (10)^{-1}$ cpd, and then drops abruptly but is still about 0.15 at $|\nu| = (3)^{-1}$ cpd with a higher cyclonic γ^2. This suggests that some of the higher frequency geostrophic energy is either aliased in the maps or created by the spatio-temporal interpolation along the drifter trajectories. The higher cyclonic coherence may be due to a higher sampling of cyclones by the drifters (e.g. Middleton and Garrett, 1986). The phase (not shown) is found to be zero on average. ECMWF wind stresses showed no coherence with the geostrophic velocities (not shown) demonstrating the lack of linear relationship between wind stresses and geostrophic velocities at the local scale. Since geostrophic velocities dominate at low frequencies, this may explain the drop in γ^2 between total drifter velocities and wind stresses at low frequencies. These

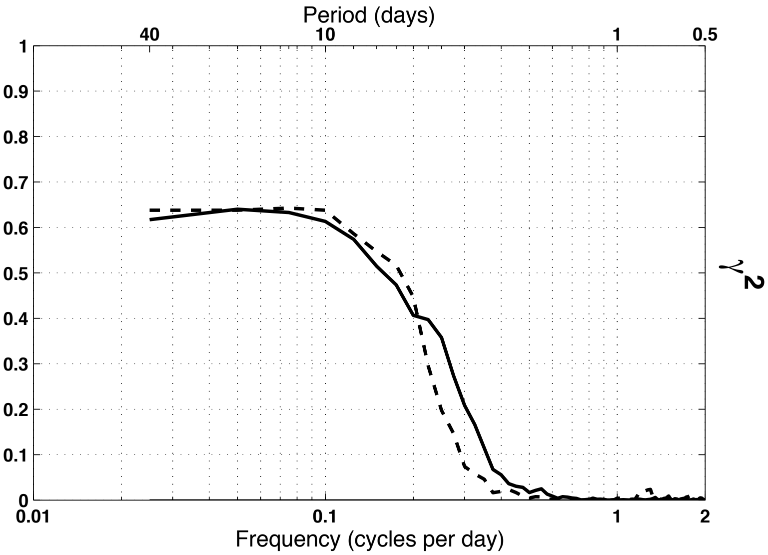

Figure 2.7: Coherence squared γ^2 between drifter velocities and geostrophic velocities derived from AVISO and GRACE altimetry measurements for the same subset of data as in Fig. 2.5. The solid curve corresponds to cyclonic frequencies and dashed curve to anticyclonic frequencies. The 95% confidence limit is plotted but is indistinguishable from the 0 line on the scale of this plot.

results imply that about 64% of the total drifter velocity variance is geostrophic and uncorrelated to local wind stress for the frequencies resolved by altimetry. Low-frequency geostrophic motions are likely to be manifestations of Rossby waves or of global scale ACC transport variations, which have been shown to be correlated to global scale wind variations (e.g. Gille et al., 2001). Since the geostrophic velocity is not coherent with the local wind stress, it can be interpreted as noise, and as such, was subtracted as described in section 2.1 in order to obtain the drifter ageostrophic velocities.

In Fig. 2.7, the coherence squared γ^2 between the local wind stress and the ageostrophic velocities differs from the results for the drifter velocities only for frequencies lower than 0.4 cpd in both anticyclonic and cyclonic domains. On average γ^2 is increased by 0.035 for the ageostrophic velocities compared to the drifter velocities. Although the difference is small, it is nonetheless statistically significant. This increase in coherence was also observed by Rio and Hernandez (2003).

2.3.1.2 High frequencies

At ν approaches ± 2 cpd, γ^2 from the drifter or ageostrophic velocities decreases to zero. We hypothesize three reasons for this. The first reason pertains to uncertainty in the accuracy of ECMWF re-analyses at high frequencies. The Nyquist frequency of the 6-hourly wind stress fields is theoretically 2 cpd but the highest frequency resolved may in reality be lower. Alford (2001) reported that the coherence between the NCEP analysis surface winds and moored buoy wind observations dropped at about 1.5 cpd. For latitudes poleward of 50°, the inertial frequency exceeds 1.5 cpd which led Alford to conclude that NCEP surface winds were not adequate to study inertial oscillations at these latitudes. ECMWF re-analyses are likely to suffer from similar problems, and their use to study high-frequency wind-driven currents may not be optimal. This issue may be even more important in the Southern Ocean, where the in-situ data assimilated in these atmospheric numerical models are relatively sparse.

The second reason is the mixed nature of the energetic inertial oscillations, which are manifested in Fig. 2.5 by the inertial peak in the ocean velocity spectra. Oceanic inertial oscillations were shown to be well represented by a slab-layer model which is linearly forced by the wind stress (e.g. Pollard, 1970; D'Asaro, 1985b). Triggered by relatively rapid atmospheric fluctuations like traveling storms, inertial oscillations can be resonant under certain circumstances (e.g. Crawford and Large, 1996; Skyllingstad et al., 2000), but they are transient phenomena. They decay relatively slowly over several inertial periods (e.g. Pollard, 1970; Lewis and Belcher, 2004) and as a consequence can interfere destructively with newly generated oscillations, causing incoherence with the local wind stress.

Thirdly, another type of high frequency motion of concern in the Southern Ocean is associated with the Stokes drift, which may be aliased in the high-frequency end of the drifter spectra, adding even more noise in the inertial frequency bands. Lewis and Belcher (2004) showed that the Stokes drift can reduce the deflection of Ekman flow relative to the wind stress direction. However, they also stated that the time-dependent

Ekman currents are unaffected by the Stokes drift. The exact effect of the Stokes drift on the frequency-dependent Ekman currents evidenced here remains unclear.

2.3.2 Coherence phase

At zero frequency (not shown), the phase of the cross-spectrum computed when the mean of the signal is retaained, indicates that the time-mean wind-driven velocity is 31.75°± 0.05° to the left of the wind stress when the mean geostrophic velocities from GRACE data are used, in qualitative agreement with the Ekman theory. This angle is reduced to 27°± 0.05° when velocities from atlas data are used. Fig. 2.6b shows the results for the anticyclonic and cylonic phase, χ^+ and χ^- respectively, for $|\nu| = 0.025$ to 2 cpd, for the cross-spectrum computed by removing the mean of the signal. The curves are noisy for frequencies higher than the average inertial frequency of the ACC dataset (1.46 cpd), where γ^2 decays almost to zero and the phase significance becomes dubious. For $|\nu| < 1$ cpd, the phase differs by less than 3° between the drifter velocities and the ageostrophic velocities, and subsequently we discuss only the ageostrophic curves. In Fig. 2.6b, the anticyclonic phase χ^+ increases with increasing anticyclonic frequencies, from 32.30° at $(40)^{-1}$ cpd to 70.30° at 1.225 cpd. In contrast, the cyclonic phase χ^- is almost constant with an average value of 29.45° between -$(40)^{-1}$ and -1.225 cpd. At the inertial frequency, χ^+ is approximately zero, meaning that the coherent rotary currents at 15 m are aligned with the wind stress direction.

As ν becomes greater than the inertial frequency, χ^+ changes sign, indicating that the ocean velocity jumps from the left to the right of the wind stress vector. This phase behavior is in very good agreement with Gonella's (1972) models, which predict such a phase jump. A slab-layer model for wind-driven motions (Pollard and Millard, 1970) is also consistent with a phase jump at the local inertial frequency but predicts a near 90° phase between wind stresses and wind-driven ocean velocities at all depths, which is not observed here. Since χ is less than 90° at zero and at low sub-inertial frequencies, the wind stress-coherent ocean velocities captured by the cross-spectral analysis appear to be manifestations of Ekman motions and this is discussed in Chapter 4. On the basis of this interpretation, estimates of the wind energy input to the Ekman layer are provided in Chapter 3.

For a given frequency band, the fraction of the phase due to angle separation and the fraction due to a potential time separation or lag are indistinguishable when considering rotary circular components (as illustrated in Fig. 2.4). However, in the anticyclonic domain, where γ^2 is the highest and the phase information is therefore more reliable, χ^+ appears to depend linearly on frequency, as would be the result of a constant time lag; a least-square fit between 0 and 1 cpd for χ^+ gives a linear slope of 28.07° per cpd, corresponding to a 1.87 hour lag of wind stresses relative to drifters.

For the data in the ACC, correcting for this time lag increased the energy input rate estimation only slightly by 3.5%. The energy input estimation is the focus of Chapter 3. However, this time lag is more problematic in Chapter 4 because it appears to distort significantly the shape of the observed transfer function in a way that is incompatible with the Ekman models considered. Several other types of wind products from the ERA-40 ECMWF Project re-analyses and the NCEP/NCAR Reanalysis Project (Kalnay et al., 1996) were tested in order to investigate further this frequency dependency. The phases of the cross-spectra for data in the 52°- 54°S latitudinal band are plotted in Fig. 2.8, on a linear frequency scale. From this figure, it appears that the time stamp of the data must be interpreted with care. In particular, both for 10-m wind or wind stress fields it must be considered whether winds are nowcast or forecast and whether the winds are intended to be valid instantaneously or if they represent average values valid over the length of the model time step. As an example, the NCEP wind stress, which is an average value valid over the 6 hours following the drifter time, shows a constant time lag of 3 hours with respect to the instantaneous ECMWF wind stress value valid at the drifter time. In the end, we decided to use the instantaneous ECMWF wind stress valid at the drifter time and to correct in each latitudinal band for a constant time lag estimated by a least-square linear fit for χ^+ between 0 and 1 cpd. The constant time lags for each of the 2° latitudinal bands are listed in Table 2.1.

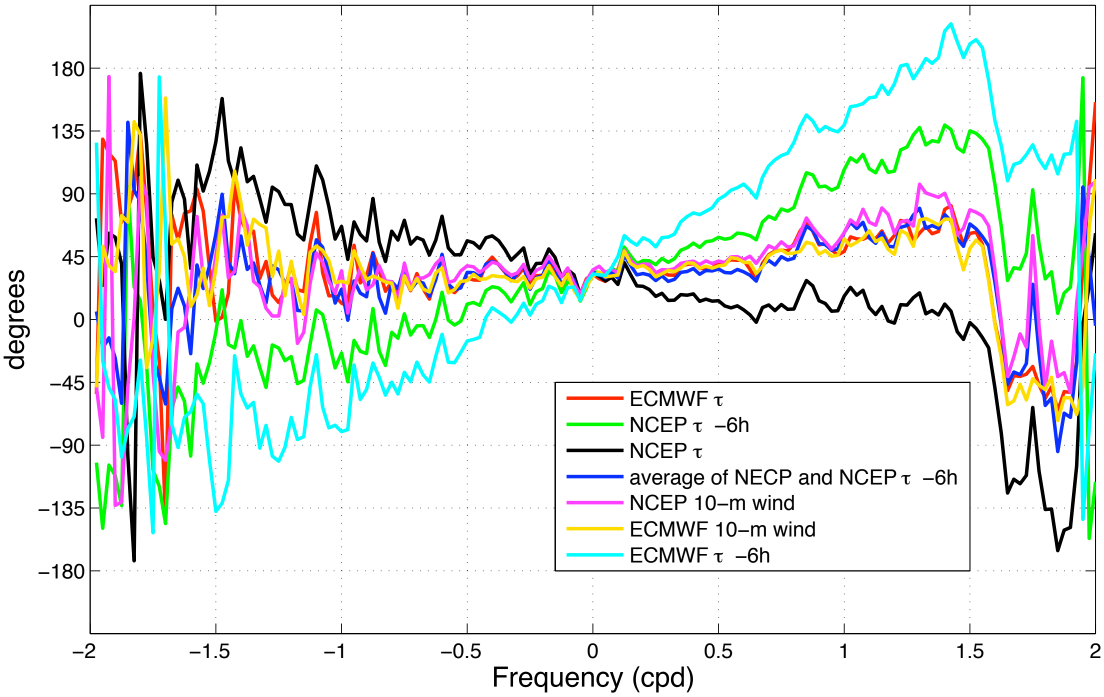

Figure 2.8: Phase of the cross-spectrum between the drifter ageostrophic velocities and various wind and wind stress data for the data in the 52°- 54°S latitudinal band. ECMWF stress, ECMWF 10-m wind and NCEP 10-m wind are instantaneous values valid at the drifter time. NCEP stress -6h is the average value valid over the previous 6 hours before the drifter time. NCEP stress is the average value valid over the next 6 hours starting from the drifter time. Average NCEP stress is the arithmetic average of these last two values. ECMWF stress -6h is the instantaneous stress value valid 6 hours before the drifter time. A positive phase means that the ocean velocity is to the left of the wind. A positive linear slope of the phase indicates that the wind lags the ocean velocities. In the order of the legend, the linear dependency of the phase on frequency between 0 and 1 cpd converted to a constant time lag in hours of the wind product with respect to the ocean velocity are: 1.62, 4.69, -1.36, 1.68, 1.77, 1.26, 7.64.

2.4 Summary

Frequency rotary spectra of wind stress and 15-m Lagrangian velocity were estimated in the Southern Ocean, based on SVP drifter trajectories in the Southern Ocean during the decade 1992-2002. The rotary spectrum of ECMWF re-analyses wind stress interpolated on the drifter positions was found to be red and polarized anticyclonically. The rotary spectrum of drifter velocities was also found red but with steeper slope in the lower frequency range. This spectrum was also found to be polarized anticyclonically expect for $|\nu| = 0.25$ cpd, where it was found cyclonic. It also clearly displayed an inertial peak in the anticyclonic domain. The ageostrophic component of the drifter velocities was obtained by subtracting geostrophic velocities derived from altimetry. The ageostrophic rotary spectra was computed and found to be anticyclonic. Spectral slopes of the drifter and of the ageostrophic spectra did not reveal a straightforward relationship with the wind stress forcing spectrum but rather showed that a combination of intrinsic variability and wind stress forcing shaped the oceanic spectra. Cross-spectral analysis elucidated the linear relationship as a function of frequency. The coherence squared between wind stress and ocean velocity was found to be statistically significant at the 95% confidence level at all frequencies except close to the Nyquist frequency of 2 cpd. The coherence squared was found greater for anticyclonic frequencies, meaning that the upper ocean responds preferentially to anticyclonic forcing at inertial and sub-inertial frequencies, as predicted by extensions of the Ekman theory in the spectral domain first introduced by Gonella (1972). The study of these Ekman models is conducted in Chapter 4. The combination of stronger anticyclonic forcing and response of the ocean certainly is responsible for the observed anticyclonic polarization of the ageostrophic rotary spectrum.

Chapter 3

A spectral view of the wind energy input to the Ekman layer in the Southern Ocean

The cross-spectral analysis in Chapter 2 indicates that a statistically significant fraction of the ageostrophic velocity is coherent with the local wind stress. Statistically significant coherence does not imply causality; however, the agreement of the phase results with extensions of the Ekman theory (Gonella, 1972) suggest a causal relation. In this chapter we go back to the power cross-spectrum between wind stresses and ocean surface velocities and derive its meaning starting from the horizontal momentum balance. The derivation of a spectral energy equation will show that the real-part of the cross-spectrum, the co-spectrum, gives an estimate of the power spectral density, or frequency partition, of the rate at which kinetic energy is dissipated in the Ekman layer.

3.1 Spectral energy equation: the balance of spectra

The linearized horizontal momentum balance for the ocean in the absence of horizontal pressure gradients is:

$$\frac{\partial \mathbf{u}(t,z)}{\partial t} + if\mathbf{u}(t,z) = \frac{1}{\rho}\frac{\partial \boldsymbol{\tau}(t,z)}{\partial z}, \tag{3.1}$$

where here $\boldsymbol{\tau}$ is the turbulent Reynolds stress. The finite Fourier transform of Eq. (3.1) is:

$$i(2\pi\nu_k + f)\mathbf{U}_k(\nu, z) = \frac{1}{\rho}\frac{\partial \mathbf{T}_k(\nu_k, z)}{\partial z}, \tag{3.2}$$

where $\mathbf{T}_k$ is the Fourier transform of $\boldsymbol{\tau}$. Multiplying Eq. (3.2) by ${\mathbf{U}_k}^*$ and integrating from $z < 0$ to the surface $z = 0$ gives:

$$i\rho(2\pi\nu_k + f)\int_z^0 |\mathbf{U}_k|^2\,dz = \int_z^0 \frac{\partial \mathbf{T}_k}{\partial z}{\mathbf{U}_k}^* dz. \tag{3.3}$$

Integrating by parts the right hand side yields:

$$i\rho(2\pi\nu_k + f)\int_z^0 |\mathbf{U}_k|^2\,dz = \mathbf{T}_k{\mathbf{U}_k}^*\bigg|_{z=0} - \mathbf{T}_k{\mathbf{U}_k}^*\bigg|_{z} - \int_z^0 \mathbf{T}_k\left(\frac{\partial \mathbf{U}_k}{\partial z}\right)^* dz. \tag{3.4}$$

The first term on the right-hand side of Eq. (3.4) corresponds to the wind stress boundary condition at the surface. The second term vanishes when we let z go to $-\infty$ to represent the base of the wind-driven layer where velocities and/or turbulent stresses vanish, and hence their Fourier transforms go to zero. Next, we apply to this equation the expected value operator and divide by the length of the observation $\mathcal{T}$ to form a spectral energy equation:

$$i(2\pi\nu_k + f)E + D = S_{\boldsymbol{\tau}\mathbf{u}}, \tag{3.5}$$

where

$$E = \rho\int_{-\infty}^0 \frac{\left\langle |\mathbf{U}_k|^2 \right\rangle}{\mathcal{T}}dz, \tag{3.6}$$

$$D = \int_{-\infty}^0 \frac{\left\langle \mathbf{T}_k\left(\frac{\partial \mathbf{U}_k}{\partial z}\right)^* \right\rangle}{\mathcal{T}}dz, \text{ and} \tag{3.7}$$

$$S_{\boldsymbol{\tau}\mathbf{u}} = \frac{\left\langle \mathbf{T}_k\,{\mathbf{U}_k}^*\Big|_{z=0} \right\rangle}{\mathcal{T}} \tag{3.8}$$

are estimates of the vertically integrated kinetic power spectral density of the Ekman layer, the vertically integrated dissipated power spectral density in the Ekman layer, and the power cross-spectrum between the wind stress and the ocean surface velocity. This equation does not give the rate of change of energy but rather the average balance among various power spectral quantities.

Next, we assume that the turbulent stress $\boldsymbol{\tau}$ is proportional to the vertical shear (following a classical diffusion model),

$$\frac{\boldsymbol{\tau}(t,z)}{\rho} = K(z)\frac{\partial \mathbf{u}(t,z)}{\partial z}. \tag{3.9}$$

The stress is aligned with the velocity vertical shear, implying that the vertical eddy viscosity K is real and independent of time. No additional assumptions are applied to K. The finite Fourier transform of Eq. (3.9) is:

$$\frac{\mathbf{T}_k}{\rho} = K\frac{\partial \mathbf{U}_k}{\partial z}. \tag{3.10}$$

As a consequence,

$$D = \int_{-\infty}^{0} \rho K \frac{\left\langle \left|\frac{\partial \mathbf{U}_k}{\partial z}\right|^2 \right\rangle}{\mathcal{T}} dz \tag{3.11}$$

is a real and positive quantity. The power cross-spectrum can be decomposed classically into real and imaginary parts:

$$S_{\boldsymbol{\tau}\mathbf{u}} = C_{\boldsymbol{\tau}\mathbf{u}} - i\, Q_{\boldsymbol{\tau}\mathbf{u}}, \tag{3.12}$$

where $C_{\boldsymbol{\tau}\mathbf{u}}$ is the coincident spectrum (co-spectrum) and $Q_{\boldsymbol{\tau}\mathbf{u}}$ is the quadrature spectrum (quad-spectrum). Thus, Eq. (3.5) gives two equalities, which can be interpreted physically:

$$D = C_{\boldsymbol{\tau}\mathbf{u}}, \tag{3.13a}$$

$$-(2\pi\nu + f)E = Q_{\boldsymbol{\tau}\mathbf{u}}. \tag{3.13b}$$

In terms of dynamics, Eq. (3.13a) describes the throughput of energy in each frequency band: the dissipated energy in the Ekman layer or energy sink equals the energy source given by the co-spectrum of the Ekman velocity at the surface and the wind stress. Eq. (3.13b) states that the kinetic energy of the Ekman layer can be obtained from the quad-spectrum. These equations resemble the spectral equations for atmospheric motions derived in the time domain by Chiu (1970) who found that the spectral density of the kinetic energy is shaped by quadrature spectral quantities and that the Coriolis parameter plays a role, as is apparent in Eq. (3.13b).

Ideally, one would want to obtain the cross-spectrum using ocean surface velocities but here we have at our disposal a proxy for these, the drifter velocities, which are representative of the average velocities across the 6.1 meter length of the drogue, centered at 15 m depth. Chapter 4 contains the study of the transfer function from the wind stress to the ocean velocity as a function of frequency and depth. By comparing the observed transfer functions to the transfer functions derived from theoretical models of the Ekman layer, the vertical structure of the wind-driven velocities can be obtained. From this, the cross-spectrum with ocean surface velocities can be estimated from the cross-spectrum with the 15 m depth ageostrophic velocities as explained in section 3.2.2.

First we describe the co- and quad-spectra, $C_{\boldsymbol{\tau}\mathbf{u}}$ and $Q_{\boldsymbol{\tau}\mathbf{u}}$, between the wind stresses and the ageostrophic velocities from the time series segments located in the ACC, which are shown in Fig. 3.1. Note that for this plot, the cross-spectrum has been corrected for the spurious time lag discussed in section 2.3.2. Also, the time series segments were de-meaned following the standard procedure of spectral estimation. Fig 3.1 indicates that the anticyclonic $C_{\boldsymbol{\tau}\mathbf{u}}$ and $Q_{\boldsymbol{\tau}\mathbf{u}}$ (dashed curves) both decrease by an order of magnitude and their cyclonic counterparts (solid lines) by two orders of magnitude, as frequency increases from $|\nu| = (40)^{-1}$ to 1 cpd. This shows the stronger relative importance of the low frequencies.

$C_{\boldsymbol{\tau}\mathbf{u}}$ and $Q_{\boldsymbol{\tau}\mathbf{u}}$ are greater for anticyclonic than for cyclonic frequencies with a ratio that increases from 1.3 at $|\nu| = (40)^{-1}$ cpd to about 6 at $|\nu| = 1$ cpd for $C_{\boldsymbol{\tau}\mathbf{u}}$. The combination of a greater anticyclonic forcing spectra (Fig. 2.5) and of a preferential anticylonic ocean response results in a greater dissipation D of anticyclonic energy (Eq. (3.13a)). The polarization of E, the kinetic power of the Ekman currents, is also

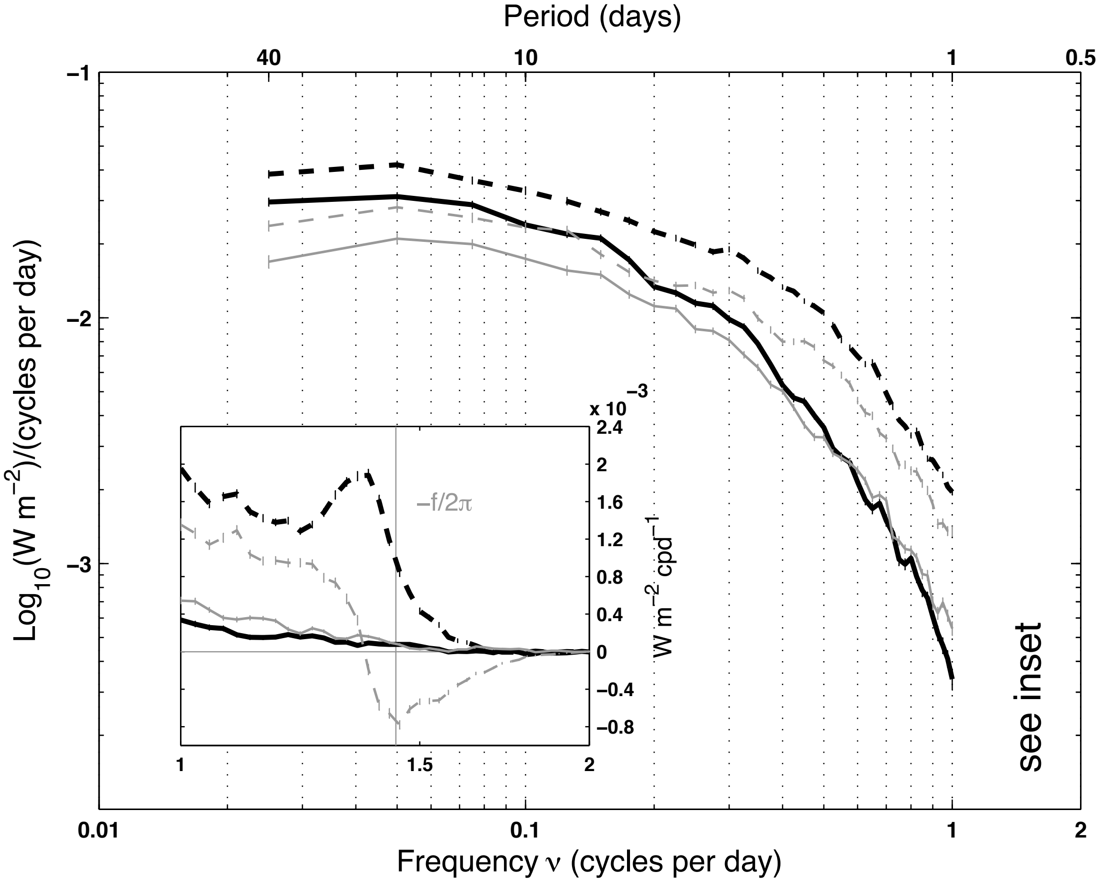

Figure 3.1: Estimates of the co-spectrum $C_{\boldsymbol{\tau}\mathbf{u}}$ (heavy black curves) and the quad-spectrum $Q_{\boldsymbol{\tau}\mathbf{u}}$ (light gray curves) density functions for anticyclonic (dashed curves) and cyclonic (solid curves) frequencies, on logarithmic scales between the wind stresses and the drifter ageostrophic velocities. The inset enlarges the 1 to 2 cpd frequency range, on linear scales. Error bars are the standard error of the means in each frequency band. The zero frequency estimates are not plotted.

anticyclonic, given by the polarization of $Q_{\boldsymbol{\tau}\mathbf{u}}$, and implies that more anticylonic energy is present in the Ekman layer.

The inset in Fig. 3.1 shows the 1 to 2 cpd frequency range. In agreement with Eq. (3.13b), $Q_{\boldsymbol{\tau}\mathbf{u}}$ approximately goes to zero and changes sign at $\nu = -f/2\pi$ (with f in radians day^{-1}). At this frequency, the study of Ekman models in chapter 4 shows that Ekman velocities are undefined and consequently the energy content E is undefined as well; A number of Ekman models that best explain the observations, however, predict the existence of a limit behavior of the Ekman velocities at the inertial frequency. These will be at all depths aligned with the wind stress direction, and the dissipation D in the Ekman layer will be theoretically maximized.

3.2 Energy input rate to the Ekman layer

3.2.1 The integral of the co-spectrum

The Wiener-Khinchine theorem states that the frequency integral of the cross-spectrum is equal to the complex cross-correlation function at zero time lag $\mathbf{R}_{\boldsymbol{\tau}\mathbf{u}}(0)$ (e.g. Bendat and Piersol, 1986):

$$\int_{-\infty}^{+\infty} S_{\boldsymbol{\tau}\mathbf{u}}(\nu)\, d\nu = \mathbf{R}_{\boldsymbol{\tau}\mathbf{u}}(0) \tag{3.14}$$

$$= \langle (\boldsymbol{\tau} - \langle \boldsymbol{\tau} \rangle)(\mathbf{u} - \langle \mathbf{u} \rangle)^* \rangle + \langle \boldsymbol{\tau} \rangle \langle \mathbf{u}^* \rangle \,. \tag{3.15}$$

For the real part this gives:

$$\int_{-\infty}^{+\infty} C_{\boldsymbol{\tau}\mathbf{u}}(\nu)\, d\nu = \mathcal{R}\left(\langle (\boldsymbol{\tau} - \langle \boldsymbol{\tau} \rangle)(\mathbf{u} - \langle \mathbf{u} \rangle)^* \rangle \right) + \mathcal{R}\left(\langle \boldsymbol{\tau} \rangle \langle \mathbf{u}^* \rangle \right), \tag{3.16}$$

which mathematically states that the integrated co-spectrum equals the sum of the real parts of the complex covariance of $\boldsymbol{\tau}$ and $\mathbf{u}$ and of the product of their time means. In no way does this imply that the co-spectrum is the frequency distribution of the total work done on the ocean by the wind stress.

The spectral analysis of the latter quantity would include the work on geostrophic currents and other processes including nonlinear forcings and interactions between frequencies. Nonlinear processes are not truly captured by the cross-spectral analysis because the cross-spectrum is a measure of the linear relationship between two signals as a function of frequency. As mentioned earlier in section 2.3, on average γ^2 between the wind stresses and the geostrophic velocity anomalies interpolated along a 40-day drifter trajectory segment is negligible. Only in a few frequency bands does it ever marginally exceed the 95% confidence level. The wind stress work on geostrophic currents at non-zero frequencies is consequently negligible in this analysis of drifter data.

This is not the case for the contribution from the mean. Indeed, for the purpose of estimating the wind energy input to the Ekman layer, the second term on the right-hand side of Eq. (3.16) indicates that a mean wind-driven current and a mean stress should be retained in order to represent the zero-frequency contribution to the wind energy input. As a consequence, the common procedure in spectral analysis of subtracting the mean from each time series segments should not be applied here. As such, it is clear that the zero frequency contribution will be contaminated if $\langle \mathbf{u}^* \rangle$ is not the true mean wind-driven velocity on average along a 40-day drifter trajectory segment. In order to best estimate the mean wind-driven velocity, one needs at least to subtract the best mean geostrophic velocity available, so the mean geostrophic velocity field derived from GRACE (Tapley et al., 2005) is used. Other available mean velocity fields derived from a combination of surface drifter data and other datasets (e.g. Rio and Hernandez, 2004; Niiler et al., 2003) were not considered because they are not independent of the drifter dataset used for this study. The influence of the mean geostrophic field goes beyond the zero-frequency and affects the cross-spectrum up to the $\pm(20)^{-1}$ cpd frequency bands, the lowest non-zero frequencies resolved in this analysis. This can be understood as a byproduct of the Lagrangian nature of the data, because the interpolation of a time-mean spatially-varying field along a drifter's spatial displacement causes a low-frequency component in the velocity signal.

In general, GRACE data lead to larger mean geostrophic velocities than atlas hydrographic data, especially south of 42°S; a consequence is that in the ACC, the contribution from the low-frequency components less than or equal to $(40)^{-1}$ cpd to the wind energy input using GRACE data is about 22% smaller than when atlas hydrographic data are used. This difference is however not constant across the Southern Ocean when the data are further sorted in 2° latitudinal bands. It is reduced by 17% on average south of 42°S but is increased on average by 1.9% north of 42°S. When the total wind energy input is considered, the influence of the mean field is somewhat less; the energy input is reduced by 8% south of 42°S and this influence is approximately zero north of 42°S.

3.2.2 The shear bias

In this section, some results that are presented in chapter 4 are anticipated for the purpose of estimating the wind energy input rate. The transfer function theoretically links the auto-spectrum of the wind stress to the cross-spectrum of the wind stress and the velocity at depth z (e.g. Bendat and Piersol, 1986, p. 190):

$$S_{\boldsymbol{\tau}\mathbf{u}}(\nu, z) = \mathbf{H}(\nu, z) S_{\boldsymbol{\tau}\boldsymbol{\tau}}(\nu). \tag{3.17}$$

Since $S_{\boldsymbol{\tau}\boldsymbol{\tau}}$ is a real quantity, the co-spectrum is obtained by taking the real part of the previous expression:

$$C_{\boldsymbol{\tau}\mathbf{u}}(\nu, z) = \mathcal{R}\left[\mathbf{H}(\nu, z)\right] S_{\boldsymbol{\tau}\boldsymbol{\tau}}(\nu) \tag{3.18}$$

Applying this equation for $z = 0$ and $z = -15$, the co-spectrum of the wind stresses and the ocean velocities at the surface is obtained by:

$$C_{\boldsymbol{\tau}\mathbf{u}}(\nu, 0) = \frac{\mathcal{R}\left[\mathbf{H}(\nu, 0)\right]}{\mathcal{R}\left[\mathbf{H}(\nu, -15)\right]} C_{\boldsymbol{\tau}\mathbf{u}}(\nu, -15) \tag{3.19}$$

$$= R^{-1} C_{\boldsymbol{\tau}\mathbf{u}}(\nu, -15). \tag{3.20}$$

In order to obtain the shear correction coefficient R^{-1}, the transfer function $\mathbf{H}$ needs to be known as a function of frequency and depth. In order to do this, as

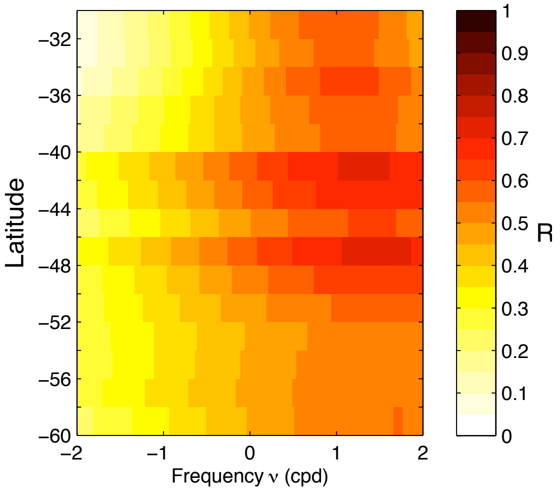

Figure 3.2: Ratio of the co-spectrum at 15 m to the co-spectrum at the surface.

explained in greater detail in Chapter 4, the observed transfer function is estimated from the drifter and stress data. Then, theoretical models of the oceanic boundary layer are considered to derive 9 analytical expressions for the transfer function, which are fitted to the observations by finding the best set of parameters that minimizes a cost function. Once the best model is assessed and the optimum parameters are estimated, the full theoretical transfer function as a function of depth and frequency is known. As such, the ratio R can be explicitly computed and used in expression (3.19) to obtain the co-spectrum at the surface.

The overall best model (model (1b), see Chapter 4) across the Southern Ocean is a 1-layer model with a constant viscosity O(0.01-0.1) m^2 s^{-1} and a boundary layer depth O(30-50) m.

The inverse of the shear correction coefficient R, which is less than 1 and more convenient to display, is plotted in Fig. 3.2 as a function of latitude and frequency. These correction coefficients are applied throughout the rest of this dissertation whenever the surface co-spectrum is discussed.

3.2.3 The bias from the slip

Surface drifters are excellent but not perfect water-followers and their velocities contain an erroneous slip velocity thought to be caused by two phenomena. First, the direct action of the wind on the surface flotation buoy, and second the vertical shear of the horizontal velocity across the vertical extend of the drogue. Niiler et al. (1995) estimated the slip $\mathbf{u}_s$ as the arithmetical average of the water velocities past the drifter's drogue, measured by two vector measuring current meters mounted at the top and bottom of the drogue of drifters released in the tropical and northeastern Pacific. They modeled the slip as:

$$\mathbf{u}_s = \frac{a}{R}\mathbf{w}_{10} + \frac{b}{R}\Delta\mathbf{u}, \tag{3.21}$$

where $\mathbf{w}_{10}$ is the 10-m wind velocity, R is the drag area ratio of the drogue to the other constituents of a drifter (40 for a SVP-type drifter) and $\Delta\mathbf{u}$ is the velocity difference measured between the top and bottom of the drogue. The coefficients a and b were obtained by regressing the downwind component of $\mathbf{u}_s$ against $\mathbf{w}_{10}$ and $\Delta\mathbf{u}$. Since no measurements in the field were obtained for winds stronger than 10 m s^{-1}, this model has only been validated for winds of magnitude less than 10 m s^{-1}. This is problematic in the Southern Ocean where intense winds are encountered. In fact, the mean quarter-daily ECMWF ERA-40 reanalysis 10-m winds interpolated onto the drifter locations are found to be greater than 10 m s^{-1} between 48°S and 58°S, and the wind slip at these latitudes could be largely underestimated (Niiler et al., 2003).

Since $\Delta\mathbf{u}$ cannot be determined from drifter data alone, only the impact of the wind-produced slip, the first term on the right-hand side of Eq. (3.21), can be evaluated for this study. This wind slip is computed using ECMWF 10-m winds interpolated in time and space, and is subtracted from the drifter velocities in order to obtain the wind slip-corrected velocities. Niiler et al. (1995) found that the best-fit values of a for either of two different types of drifter, TRISTAR or Holey-Sock (the SVP kind) were not statistically different. As a consequence, the best estimated from the combined drifter datasets, $a = 4.63 \times 10^{-2}$ is used here.

For this study, the basic impact of this slip correction is to modify the estimates of the cross-spectrum, but it potentially acts at two steps of the wind energy input computation. First, in the fitting procedure in Chapter 4, it is found that applying the wind slip correction increases the magnitude of the vertical viscosity and of the boundary layer depth for the best model. A deeper boundary layer and larger viscosity coefficient means that the shear from the surface to 15 m depth is not as large. Second, the wind slip correction also modifies the cross-spectrum of the wind stress and the 15 m velocity by reducing the magnitude of its real part, the co-spectrum. Correspondingly, this reduces the inferred co-spectrum of the wind stress and the surface ocean velocity. The estimates for the energy input rate D are accordingly reduced. We find that these are decreased by 39% for the data specifically in the ACC. North of 54°S, the reduction averages 32% but it is only 13% south of this latitude. In terms of absolute energy input rates, this amounts to approximately 13 $\times 10^{-3}$ W m^{-2} for the data in the ACC, and to between 3 and 17 $\times 10^{-3}$ W m^{-2} across the Southern Ocean, averaging to 8.6 $\times 10^{-3}$ W m^{-2}.

3.3 Results in the ACC and across the Southern Ocean

3.3.1 ACC

Fig. 3.3 shows the cumulative integration from $|\nu| = 0$ to 2 cpd of the surface co-spectrum from data in the ACC region for anticyclonic frequencies (dashed curves), cyclonic frequencies (thin solid curve) and both frequencies (heavy solid curve). Fig. 3.3 also shows frequency limits used in previous published estimates of wind energy inputs to the ocean (see Section 1.1).

The anticyclonic energy input contributes 59% of the total input and is 46% greater than the cyclonic input due to a combination of stronger anticyclonic wind stress and polarized ocean response.

On average in the ACC, the energy input rate totals $34.2 \pm 0.4 \times 10^{-3}$ W m^{-2} for all frequencies resolved. The zero frequency contribution alone is $8.4 \pm 0.3 \times$

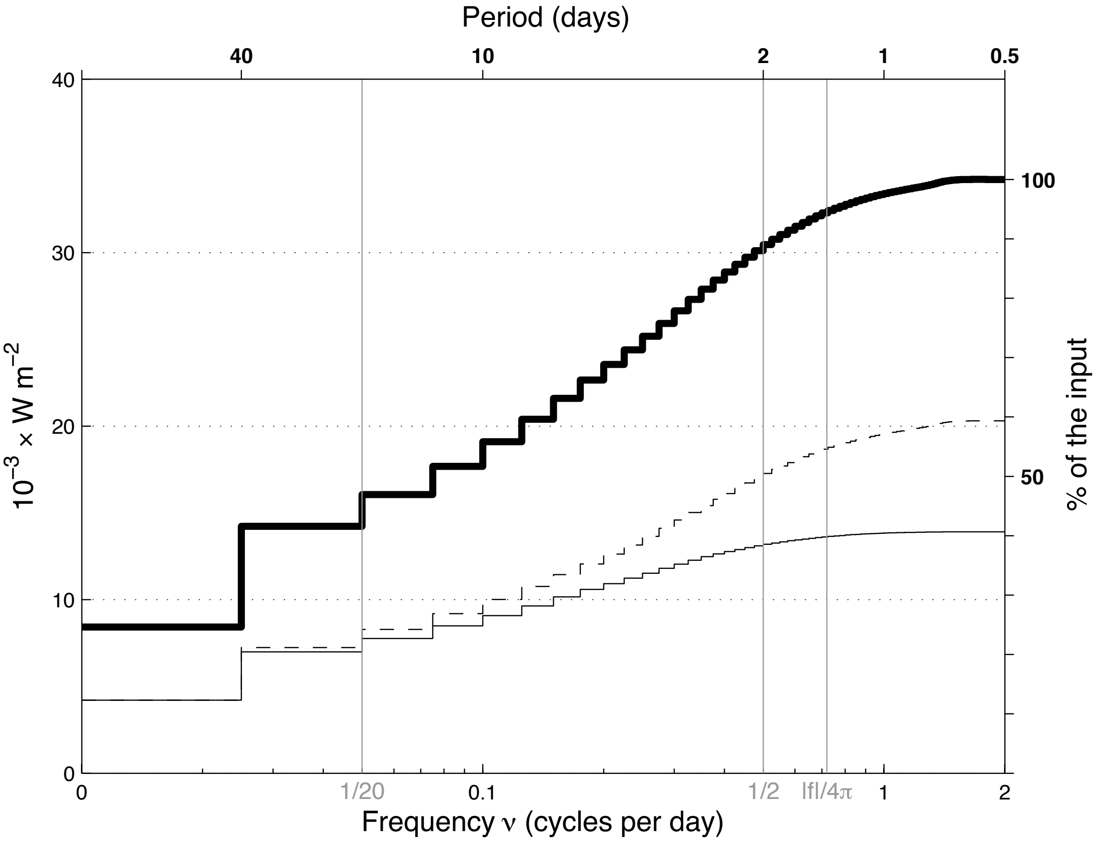

Figure 3.3: Cumulative integration of the co-spectra at the surface in the ACC for anticyclonic frequencies (dashed curve), cyclonic frequencies (thin solid curve) and the sum of anticyclonic and cyclonic frequencies (solid heavy curve). The axis of the abscissas is on a logarithmic scale but the lowest frequency plotted in each case is the zero frequency contribution, which is split evenly between the anticyclonic and cyclonic domains. Vertical lines mark specific frequencies.

10^{-3} W m^{-2}, or about 25%. The predominance of the time-varying components is actually seen all across the Southern Ocean in Fig. 3.4 (panel a), as it is always greater than the contribution from the zero frequency. This is in contrast with the time scales at which potential energy is thought to increase: Wunsch (1998) found in his estimate of Eq. (1.1) that the contribution from the time mean accounted for about 94% of the global average value. However, the time-varying components were resolved up to approximately $(20)^{-1}$ cpd only, the Nyquist frequency for T/P orbit repeat period, and contributions from higher frequencies, especially arising from wind fluctuations, were believed to be very small. For the wind energy input rate to the Ekman layer, motions at frequencies higher than $(20)^{-1}$ cpd actually contribute 53% of the total, in the ACC.

Up to $|\nu| = 1/2$ cpd (indicated by a vertical gray line in Fig. 3.3), the energy input rate sums to $30.5 \pm 0.4 \times 10^{-3}$ W m^{-2}. This is larger than Wang and Huang's (2004) estimates, which varied between about 12 and 20×10^{-3} W m^{-2} in the ACC region (see their Fig. 3). For their estimates, they used a theoretical model to compute the Ekman velocities at the surface. Their model assumes an infinitely deep ocean and a constant vertical viscosity , and is shown in Chapter 4 to be the worst model among the ten models tried. For the purpose of the wind energy input, this model underestimates the co-spectrum because it imposes the velocities at the surface to be at 45° from the wind stress direction. Moreover, we find that higher frequencies from $|\nu| = 0.525$ to 2 cpd, neglected by Wang and Huang (2004), add a non-negligeable 11% contribution of $3.8 \pm 0.6 \times 10^{-3}$ W m^{-2}. In fact, the variance of the wind stress from numerical weather reanalyses like ECMWF may be too low at high latitudes (Gille, 2005), and consequently the contribution from these frequencies may be underestimated.

In the "near-inertial" frequency range, here taken from $\nu = -f/2\pi/2$ to 2 cpd, the anticyclonic frequencies input $1.52 \pm 0.01 \times 10^{-3}$ W m^{-2}. This represents a 4.4% contribution to the total, and is of the same order of magnitude as the energy flux into wind-forced near-inertial mixed-layer motions, over broad oceanic regions, that can be estimated from a slab-layer model (e.g Alford, 2001). This suggests that time-dependent Ekman velocities need to be considered when estimating the wind energy input around the inertial frequency. Also, this shows that, at least for the ACC region, the wind energy input to the Ekman layer is a process which takes place dominantly at subinertial frequencies and not in the inertial band.

3.3.2 Southern Ocean: latitudinal and seasonal variabilities

The total drifter dataset is divided in 2° latitudinal bands, without regard for dynamic height contours, to study latitudinal and seasonal variability. The co-spectra were estimated in each of these bands, and in order to analyze the frequency distribution of the energy input rate, they were integrated over specific frequency ranges. The results for the whole dataset are plotted in Fig 3.4 and the results for the austral winter and summer subdatasets are plotted in Fig. 3.5. The detailed caption of Fig. 3.4 applies for Fig. 3.5 with the difference that the series of red-shaded curves correspond to the austral summer and the blue-shaded series to the austral winter.

The frequency band-limited energy input rates are plotted in the first columns of Figs. 3.4 and 3.5; the second columns show the relative contribution of these integrals as a function of latitude, and the third columns show the corresponding integrals of the wind stress spectral density function. The zero frequency corresponds to the mean value squared, the integral for all non-zero frequencies is the wind stress variance, and an integral over a frequency range that includes the zero frequency is a mean square value.

3.3.2.1 All data

First, our attention is turned to the results obtained from all data. For the energy input rates in Fig. 3.4a, the contribution from the zero frequency (light gray line) increases by approximately a factor of 12 from $(1.1 \pm 0.1) \times 10^{-3}$ W m^{-2} at 31° S to a maximum of $(13 \pm 2) \times 10^{-3}$ W m^{-2} at 53° S. The increase in its relative contribution is not so dramatic, from 11.5% at 31°S to 28% of the total input at 51°S (Fig. 3.4b). South of 53°S, both the absolute and relative contributions of the zero frequency decrease. In contrast, the contribution from the non-zero frequencies (Fig. 3.4a, dark gray line) increases further south from (8.6 ± 0.2) $\times 10^{-3}$ W m^{-2} at 31°S to (40 ± 2) $\times 10^{-3}$ W m^{-2} at 57°S, an increase by a factor larger than 4. The total energy input rate (Fig. 3.4a, black line) is minimum at (9.8 ± 0.3) $\times 10^{-3}$ W m^{-2} at 31°S and maximum at (53 ± 3) $\times 10^{-3}$ W m^{-2} at 57°S, an increase by more than a factor of 5. In Fig. 3.4c, the wind stress mean value squared (light gray line), variance (dark gray line) and the mean squared value (black line) show similar behaviors with latitude: all three increase southwards from 31°S to maxima at 53°S, and then decrease again south of 53°S.

As was already pointed out in the detailed study of the co-spectrum estimated from the data in the ACC, the energy input to the Ekman layer is predominantly anticyclonic and, as shown in Fig. 3.4d, this is observed almost throughout the Southern Ocean, except southwards of 57°S where about an equal amount of energy is input through cyclonic and anticyclonic frequencies. The relative contributions of the anticyclonic and cyclonic frequencies (for which the contribution of the mean is divided equally between the two frequency domains) are plotted in Fig. 3.4e. The anticyclonic contribution decreases from 72% at 31°S to 50% at 59°S. This is a consequence of two factors. First, as indicated in Fig. 3.4f, the wind stress forcing has a larger mean square value for anticyclonic frequencies (dashed lines) than for cyclonic frequencies (solid lines) across the Southern Ocean. The relative contribution of the anticyclonic frequencies for the mean square value of the wind stress (not shown) is approximately 70% at 31°S and decreases to about 53% at 59°S (not shown). If the oceanic response were flat, the exact same contribution of the anticyclonic frequencies for the energy input should be observed. Here, it is found that it is greater, because of the second factor, which is the preferential anticyclonic response of the ocean, as predicted by theoretical Ekman models, explicitly studied in Chapter 4.

Fig. 3.4g,h,i show (with gray lines) the contribution of the near inertial frequencies from $\nu = -f/2\pi/2$ to 2 cpd. In panel i, the variance of the wind stress contained in this near-inertial range is isolated (multiplied by 10 for legibility): it increases from 31°S to 45°S, then stays almost constant to 53°S, and finally decreases towards 59°S. Similarly, the energy input rate in this frequency range (multiplied by

10 for legibility in panel g) increases with latitude, peaks at 45°S and decreases further south. The contribution from the remaining (non inertial) frequencies (panel g) is almost identical to the total frequency range (panel a) because the near-inertial relative contribution is quite modest, from 6.6% at 31°S, decreasing almost monotonically to 1.5% at 59°S (panel h). This decrease may be due to the fact that as we progress southward, less and less supra-inertial energy is captured by the 6-hour sampling, because the inertial frequency is closer to the Nyquist frequency of 2 cpd.

3.3.2.2 Seasonal variability

The wind energy input estimates in Fig. 3.4 were recomputed after sorting the data between a summer season and a winter season. All the curves in Fig. 3.4 fall in between their seasonal counterparts in Fig. 3.5. Broadly speaking, the seasonal variability manifests itself latitudinally and also as a function of the frequency range considered. From summer to winter, south of 48°S, the energy input rates due to the mean (light blue and red lines in Fig.3.5) are not distinguishable within the error bars and only north of this latitude are the differences statistically significant with modifications by factors between 0.5 and 3.1.

However, on average, the energy input rates from the non-zero frequencies are increased by 69%. This increase also varies latitudinally, roughly decreasing from north to south, with almost twice the fractional seasonal difference at 39°S as at 55°S. As a consequence, since the total energy input (red and dark blue lines in Fig. 3.5) is dominated by the non-zero frequencies, from summer to winter, the total input is increased on average by 67%, but this seasonal increase varies greatly: south of 42°S it averages to 42% but north of 42°S it averages to 105%.

Figs. 3.5d, e and f indicate that the partition of the input between anticyclonic and cyclonic frequencies does not show qualitative differences as a function of seasons.

The wind energy input in the near-inertial range (Fig. 3.5g) does show an increase from summer to winter, between 5% and 122% across the Southern Ocean.

This pattern follows the trend of increased wind stress variance in winter in the near-inertial band, but it is less dramatic since the near-inertial variance of the wind stress can be multiplied by a factor up to 2.5. This surprising defect in the seasonal variability of the near-inertial energy (directly forced by the wind) could come, like the observed decrease in Fig. 3.4 g, from the fact that drifters may not capture all the high frequency energy of the ocean currents.

Figure 3.4: Energy input rates across the Southern Ocean. (a) Contribution from the mean (light gray line), contribution from the non zero frequencies (gray line) and total (black line) within each latitudinal band. (b) Relative contributions of the zero frequency (light gray line) and of the non zero frequencies (gray line) in the total energy input rate. (c) Mean value square (light gray line), variance (gray line) and mean square value (black line) of the wind stresses interpolated on the drifter positions. (d) Energy input rate contributions from the anticyclonic (dashed line) and the cyclonic frequencies (solid line). (e) Relative contribution of the anticyclonic (dashed line) and cyclonic (solid line) frequencies for the total energy input rate. (f) Mean square value (variance plus half of the mean) of the wind stresses for anticyclonic (dashed line) and cyclonic frequencies (solid line). (g) Contribution from the near-inertial frequencies multiplied by 10 for legibility (gray line) and contribution from the remaining frequencies (black line). (h) Relative contribution of the near inertial frequencies for the total energy input rate. Note the change of scale for the abscissa compared to panels b and e. (i) Wind stress variance for the near-inertial frequencies multiplied by 10 for legibility (gray line) and mean square value for the remaining frequencies (black line). Error bars for the energy input rate are derived from the standard errors for the co-spectra. Error bars for the wind stress variance are derived from the formal 95% confidence intervals of the wind stress spectra.

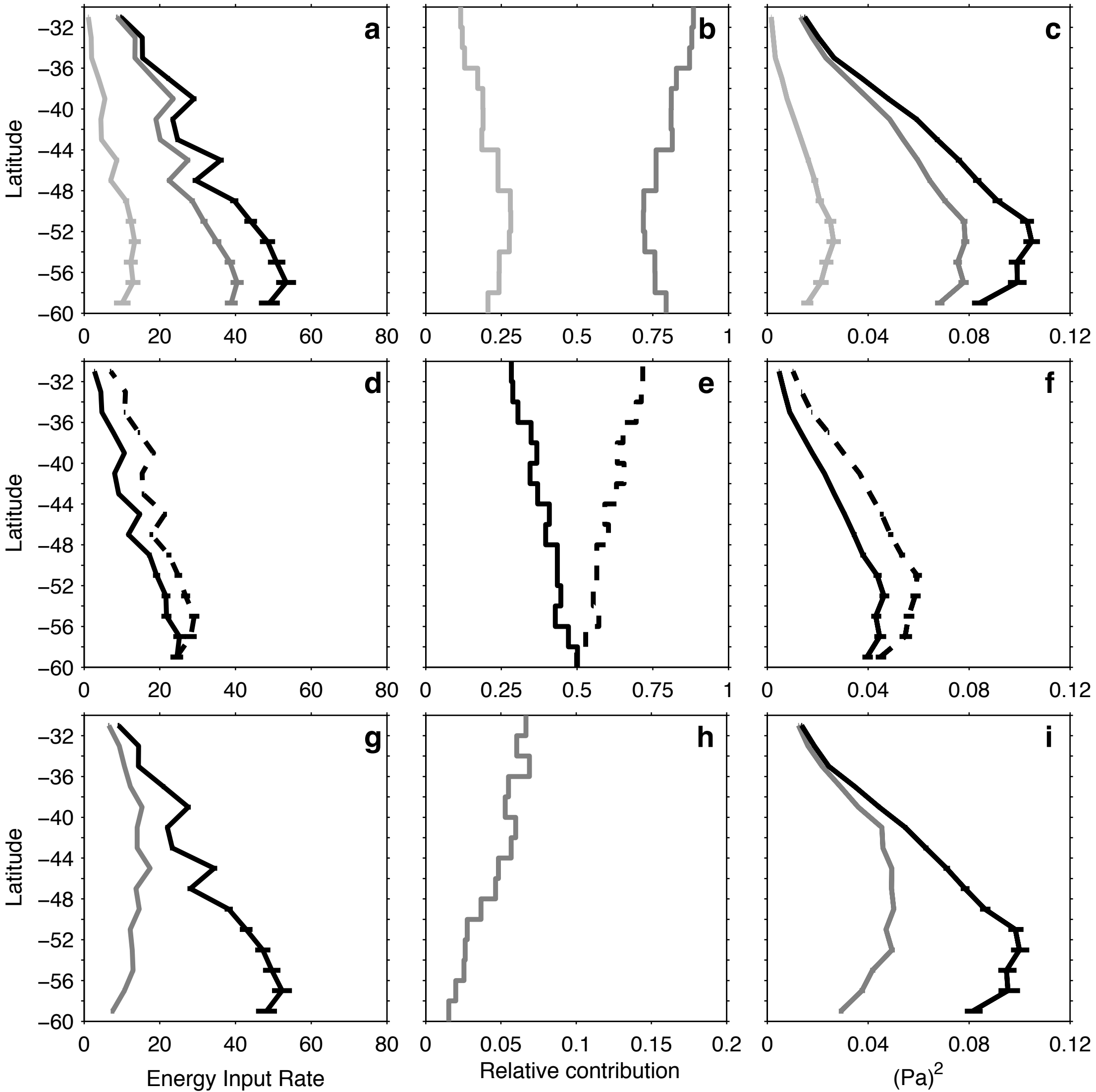
a
b
c
d
e
f
g
h
i
Latitude
-32
-36
-40
-44
-48
-52
-56
-60
0
20
40
60
80
0.25
0.5
0.75
1
0.04
0.08
0.12
0.05
0.1
0.15
0.2
Energy Input Rate
$(10^{-3} \times W\ m^{-2})$
Relative contribution
$(Pa)^2$

3.4 Summary

On the basis of the cross-spectral analysis conducted in Chapter 2, the fraction of the ageostrophic velocities that was coherent with the wind stress was identified as Ekman velocities. From there, it was assumed that Ekman dynamics took place on average at a local scale along a drifter trajectory segment and that a classical diffusion model applied, where the turbulent stress is proportional to the vertical velocity shear. In this framework, the real part of the cross-spectrum, the co-spectrum, between the ageostrophic velocity at the surface and the wind stress is a measure of the energy source for the Ekman balance, as a function of frequency. This energy goes into turbulent kinetic energy available for dissipation throughout the Ekman layer. Anticipating results presented in Chapter 4 about the vertical structure of the Ekman layer, drifter ageostrophic velocities were used to estimate the surface cross-spectrum with the wind stress, and the total energy input rate was obtained by integrating the surface co-spectrum over the cyclonic and anticyclonic frequencies from $|\nu| = 0$ to 2 cpd. In the ACC, the average wind energy input rate was found to be (34.2 $\pm$ 0.4) $\times$ 10^{-3} W m^{-2}. Of this input rate, 75% comes from the non-zero frequencies, and 59% comes from the anticyclonic frequencies. On average in the Southern Ocean, the zonally averaged rate of wind energy input has a mimimum value of (9.7 $\pm$ 0.2) $\times 10^{-3}$ W m^{-2} at 31°S, and reaches a maximum of (53 $\pm$ 2) $\times$ 10^{-3} W m^{-2} at 57°S. In all latitudinal bands, the contribution from the non-zero frequencies dominates over the mean. Moreover, for these frequencies, the anticylonic frequencies contribute more than the cyclonic frequencies. This is a consequence of the anticyclonic polarization of the wind stress forcing and of the preferential anticyclonic response of the upper ocean. Not only the wind energy input to the Ekman layer follows the latitudinal variations of the wind stress but also its seasonal variations. Seasonal variability of the energy input is found for the zero-frequency component only north of 48°S, and is found at all latitudes for the non-zero frequency components, in close accordance with the variability of the wind stress.

The spectral partition of the energy input to the Ekman layer in the Southern

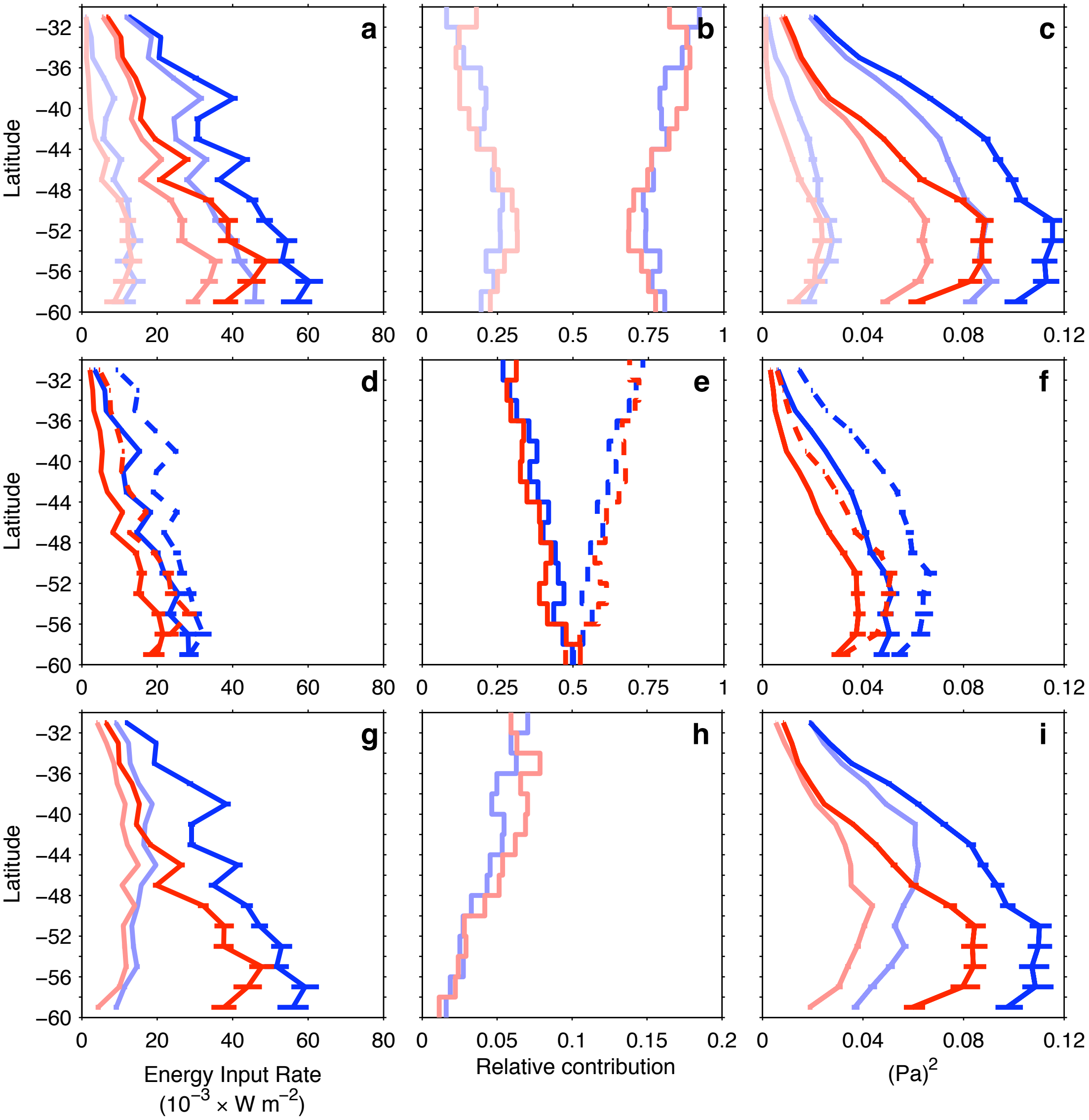

Figure 3.5: Energy input rates across the Southern Ocean as a function of season. Blue shading: austral winter, red shading: austral summer. For the description of each panel see the caption of Fig. 3.4.

Ocean clearly relate the energy input to the amount of energy contained in the wind stress, interpolated from ECMWF reanalyses data on the drifter positions. Overall, the large energy input found here is available for dissipation and mixing and is likely important for sustaining the thermohaline circulation.

Chapter 4

Ekman layer depth and vertical viscosity in the Southern Ocean

4.1 Introduction

In this chapter, we are interested in the near-surface vertical mixing of horizontal momentum that has been injected at the surface by the wind stress in the Southern Ocean, and which was estimated in Chapter 3. This mixing is equivalent to the vertical flux per unit mass $\langle \mathbf{u}' w' \rangle$, where angular brackets ($\langle \cdot \rangle$) represent the "fast" time average and primes the turbulent fluctuations that are not resolved by slowly varying large-scale observations, and where $\mathbf{u}$ is the horizontal component of the oceanic velocity. This flux defines a turbulent or Reynolds stress (per unit mass) acting on the large-scale circulation (e.g. Pedlosky, 1979):

$$\langle \mathbf{u}' w' \rangle \equiv \frac{\boldsymbol{\tau}}{\rho}, \tag{4.1}$$

with w the vertical component of ocean velocity, chosen here positive if downward, and ρ the density of seawater. Following the concept of Eq. (1.2), this turbulent stress is written as an eddy coefficient times the vertical gradient of horizontal velocity:

$$\frac{\boldsymbol{\tau}}{\rho} = -K \frac{\partial \langle \mathbf{u} \rangle}{\partial z}, \tag{4.2}$$

where K is the symbol used from now on for the vertical viscosity. Eq. (4.2) provides a first order turbulence closure scheme of the Reynolds equations for the ocean velocity in the OBL. This parameterization yields equations of motion conveniently in terms of $\mathbf{u}$ only. In section 4.3 of this chapter, by Fourier transforming the linearized version of the equations of motion, we show that the theoretical linear transfer functions from the wind stress to the ocean wind-driven velocity can be obtained, as a function of frequency. These transfer functions are dependent on the assumptions made for the shape of vertical profile for K, as well as on the lower boundary condition for the OBL. As such, simultaneous observations of ocean velocity and wind stress allow to estimate the transfer function, which can be compared to theoretical models and, since these depend on the viscosity, the latter can be estimated.

Oceanic observations at sub-inertial frequencies (Weller and Plueddemann, 1996) indicate that turbulence closure models can lead to better predictions of wind-driven velocities than slab-like models. For prediction of wind-driven velocities, an alternate approach consists in using mixed-layer models that assume that the momentum injected by the wind is instantaneously (i.e. within one model time step) and uniformly distributed over the depth of the OBL, implying that the viscosity is infinite. Mixed-layer models have been successful at modeling oceanic oscillations around the local inertial frequency but do not provide information about the way the momentum is mixed, nor about parameterization of the momentum flux in the OBL.

The simplest model which assumes a finite viscosity is the steady Ekman (1905) model. In terms of the transfer function, it corresponds to the zero frequency component, that is when the wind stress is steady and unidirectional. In this model, K is constant and the ocean is assumed to be homogeneous and of infinite depth. It is unlikely that these conditions can be achieved in the real ocean and, as a consequence, the modeled vertical structure of the current, the famous Ekman spiral has been very difficult to observe and only through extensive spatial and temporal averaging was it demonstrated to some degree (e.g. Price et al., 1987; Wijffels et al., 1994; Chereskin, 1995). For this model, an analytical solution for the transient motions from an ocean initially at rest to a fully developed spiral can also be predicted (see also Lewis and Belcher, 2004) but the noisy nature of ocean velocity observations makes the comparison to data a very difficult task so that the spatial average or temporal mean is usually considered.

Time domain observations can equivalently be analyzed in the frequency domain. Gonella (1972) Fourier transformed the equations of motion in order to obtain theoretical expressions for the transfer function and compared these to observations obtained from mooring data. Weller (1981) tested Gonella's theory by studying the transfer function for the vertical shear but not the absolute velocity because his observations were relative to the slow but significant drift of the FLIP observation platform. Daniault et al. (1985) pioneered the use of surface velocity estimates, derived from the displacements of a free-drifting meteorological buoy, in order to estimate the phase of the transfer function between the wind and the buoy velocity. This is the approach chosen here: we use surface drifter data to estimate the zonally-averaged transfer function from the wind stress to the ocean velocity as a function of latitude in the Southern Ocean. The equation of horizontal motion, from which the transfer function is derived, is written in the Eulerian framework, and one may argue that Lagrangian velocity time series are inadequate. Despite their Lagrangian nature, surface drifter data have nevertheless been successfully used to obtain either mean geostrophic (Niiler et al., 2003) or Ekman (Rio and Hernandez, 2003) velocity fields on a global scale, by spatially averaging velocities derived from drifter displacements. For the purpose of estimating the transfer function, horizontal uniformity is assumed, and only the time dimension of the velocity time series is considered. Several results from Chapter 3 justify the use of surface drifter data. Drifter velocities are found to be significantly coherent over a wide range of frequencies with a coherence phase (equivalent to the phase of the transfer function), interpreted as evidence for wind-driven Ekman-type currents in Chapter 3 and, as will be seen in this chapter, comparable to the ones predicted from the models presented in this chapter. This demonstrate that Lagrangian velocities can be utilized and that the nonlinear advective terms are comparatively small and can be treated as noise in this analysis.

This chapter is organized as follows: section 4.2 explains the concept of transfer function from the wind stress to the ocean velocity, section 4.3 gives the theoretical transfer functions from Ekman layer models arising from different vertical profiles for the vertical viscosity (these different models constitute a hierarchy), section 4.5 presents the results of fitting our observed transfer functions to these theoretical models, and finally section 4.6 provides a summary.

4.2 The transfer function

4.2.1 Theory of the transfer function for vectors

We start from the concept of the local wind stress $\boldsymbol{\tau}(t)$ being the input of a causal linear system (the atmosphere-ocean interface) for which the output is the ocean velocity $\mathbf{u}(t,z)$. As such, the velocity $\mathbf{u}(t,z)$ at time t is a convolution of the wind stress with the impulse response function $\mathbf{h}(t',z)$, which is a function of the time lag t' and depth z (e.g. Bendat and Piersol, 1986, p. 189):

$$\mathbf{u}(t,z) = \int_0^{\infty} \mathbf{h}(t',z)\boldsymbol{\tau}(t-t')dt'. \tag{4.3}$$

Taking the Fourier transform $\int_{-\infty}^{+\infty} (\cdot)\, \exp(-i2\pi\nu t)dt$ of Eq. (4.3), the convolution theorem gives

$$\mathbf{U}(\nu,z) = \mathbf{H}(\nu,z)\mathbf{T}(\nu). \tag{4.4}$$

This linearizes the relationship: the Fourier transform of the ocean velocity $\mathbf{U}$, at frequency ν is simply obtained by multiplying the Fourier transform of the wind stress $\mathbf{T}$ at the same frequency by the transfer function $\mathbf{H}$, which is the Fourier transform of $\mathbf{h}$. Here, $\mathbf{H}$ is estimated from ocean data and compared to theoretical models.

How can one interpret the complex-valued transfer function? Let's assume the wind stress forcing is monochromatic of magnitude unity $\boldsymbol{\tau}(t) = \mathbf{1} \times \exp(+i2\pi\nu_0 t)$ (in units of N m^{-2}), rotating with frequency $\nu_0 > 0$. The hodograph of such a wind stress is a circle traced in a counterclockwise fashion. The Fourier transform of such a signal can be defined with the help of the delta function, i.e. $\mathbf{T}(\nu) = \mathbf{1} \times \delta(\nu - \nu_0)$ (in units of N m^{-2} s). The resulting ocean velocity $\mathbf{u}(t, z)$ is the inverse Fourier transform of $\mathbf{U}(\nu, z)$:

$$\begin{aligned} \mathbf{u}(t, z) &= \int_{-\infty}^{+\infty} \mathbf{U}(\nu, z) \exp(+i2\pi\nu t) d\nu \\ &= \int_{-\infty}^{+\infty} \mathbf{H}(\nu, z) \mathbf{T}(\nu) \exp(+i2\pi\nu t) d\nu \\ &= \int_{-\infty}^{+\infty} \mathbf{H}(\nu, z) \delta(\nu - \nu_0) \exp(+i2\pi\nu t) d\nu \\ &= \mathbf{H}(\nu_0, z) \exp(+i2\pi\nu_0 t). \end{aligned} \tag{4.5}$$

Thus, $\mathbf{u}(t, z)$ is a vector rotating with the wind stress at the same frequency ν_0 in the same angular direction. The velocity vector has a constant deflection angle with respect to the stress vector, which is given by the phase of the complex number $\mathbf{H}(\nu_0, z)$ (in units of kg^{-1} m^2 s). The absolute value of $\mathbf{H}$ also corresponds to the current speed for a stationary rotating wind stress magnitude of 1 N m^{-2}, which corresponds approximately to a 10-m wind speed of 20 m s^{-1}(e.g. Wu, 1980; Large and Pond, 1981; Smith, 1980; Yelland and Taylor, 1996). From the ECMWF winds and wind stresses interpolated onto the drifter positions, a similar correspondence is found (not shown). The Smith (1980) formula gives a stress of 0.124 N m^{-2} for a wind speed of 10 m s^{-1} so a good approximation to obtain the wind-driven velocity in 10 m s^{-1}wind speed from the models presented here is to divide the transfer function by a factor 10. In the remainder of this chapter, observed and theoretical transfer functions will be plotted in the complex plane. The axes are fixed in a reference frame rotating with the wind stress vector, with the x-axis aligned with the wind stress. This cross-spectral analysis is therefore independent of the coordinate system and, it is particularly appropriate for studying the angular relationship between the wind-driven ocean velocity and the wind stress. This is reminiscent of the wind coherent ensemble averaging method developed by Price et al. (1987), where the signal-to-noise ratio of the wind-driven velocities is improved by projecting them into time-averaged along- and cross-wind directions.

4.2.2 Observed transfer functions and fitting procedure

Theoretically, the transfer function also satisfies (Bendat and Piersol, 1986):

$$S_{\boldsymbol{\tau}\mathbf{u}}(\nu, z) = \mathbf{H}(\nu, z)\, S_{\boldsymbol{\tau}\boldsymbol{\tau}}(\nu), \tag{4.6}$$

where $S_{\boldsymbol{\tau}\mathbf{u}}$ is the cross-spectral density function between the wind stress $\boldsymbol{\tau}(t)$ and the ocean velocity $\mathbf{u}(t, z)$, and $S_{\boldsymbol{\tau}\boldsymbol{\tau}}$ is the autospectral density function of the wind stress, which is analyzed in detail for the drifter data within the ACC in chapter 2. The transfer function from $\boldsymbol{\tau}$ to $\mathbf{u}$ at 15 m depth was therefore estimated using the previous expression as:

$$\hat{\mathbf{H}}(\nu_k, z) = \frac{\hat{S}_{\boldsymbol{\tau}\mathbf{u}}(\nu, z)}{\hat{S}_{\boldsymbol{\tau}\boldsymbol{\tau}}(\nu)} = \frac{\langle \mathbf{T}_k\, {\mathbf{U}_k}^{*} \rangle}{\langle \mathbf{T}_k\, {\mathbf{T}_k}^{*} \rangle}, \tag{4.7}$$

using the drifter ageostrophic velocity and wind stress data sorted in 2° latitudinal bands.

The observed transfer functions from the data in each 2° latitudinal band are compared to the ten theoretical transfer functions presented in the next section. These comparisons consist in finding the optimum parameter or set of parameters that minimize the cost function L, which is a measure of the misfit between the observed and theoretical transfer functions:

$$\mathsf{L} = \sum_{\nu_k} |\mathbf{H}_m(\nu_k, z) - \hat{\mathbf{H}}(\nu_k)| \times w(\nu_k), \tag{4.8}$$

where $|\cdot|$ designates the absolute value. $\mathbf{H}_m$ is the model transfer function, $\hat{\mathbf{H}}$ is the transfer function estimate from the data and $w(\nu_k)$ is a weight which is a function of frequency. This L_1-norm was chosen over a L_2-norm because it performed better in the optimization procedure. An optimization algorithm looked for the minimum of L within the space of free parameters for $\mathbf{H}_m$. Depending on the model considered, different algorithm were utilized. The parameters for the optimization of each model are summarized in Table A.1. In the evaluation of the theoretical transfer functions, ρ was taken equal to 1027 kg m^{-3} and the depth z equal to 15 m. The value for f corresponds to the center latitude of the 2° latitudinal bands. The analysis of the coherence squared γ^2 in Chapter 2 shows that the strongest observed oceanic response takes place at sub-inertial anticyclonic frequencies. Moreover, theory of spectral estimation predicts that the normalized standard error of the cross-spectrum is inversely proportional to $(\gamma^2)^{1/2}$ (Bendat and Piersol, 1986). It is also noted (but not shown here) that the variance of the periodogram from the bootstrap samples is smaller in the same frequency bands than where γ^2 is the highest. As a consequence, the best estimates of the cross-spectrum and of the transfer function are found at subinertial anticyclonic frequencies. As a consequence, we choose $w = \widehat{\gamma^2}$ for the weight function (see Eq. 2.7).

4.3 Ekman layer models

4.3.1 Equation of motion

In this section, we present the theoretical transfer functions against which our observed transfer functions are compared. For consistency and convenience all through the derivations the vertical coordinate z is taken positive downwards and $z = 0$ is the mean ocean-atmosphere interface. The linearized horizontal momentum balance for the large-scale circulation (dropping the angle brackets for clarity) in the absence of pressure gradients is:

$$\frac{\partial \mathbf{u}(t,z)}{\partial t} + if\mathbf{u}(t,z) = -\frac{1}{\rho}\frac{\partial \boldsymbol{\tau}(t,z)}{\partial z}, \tag{4.9}$$

where $\mathbf{u}(t,z)$ is the horizontal velocity forced solely by the wind stress $\boldsymbol{\tau}(t,0)$, and f the Coriolis parameter. Csanady and Shaw (1980) concluded that " *'first-order' closure of the Reynolds equations; i.e., the classical idea that the action of turbulence on momentum transport is viscosity-like, can be made to work at least as well as more complex second-order closure schemes in describing the steady or time-dependent structure of a turbulent Ekman layer or of a surface mixed layer without vertical heat flux*." Using this approach, it is possible to model dynamically from Eq. (4.9) a linear relationship between the wind stress and the wind-stress driven ocean velocity at depth z. Using

Eq. (4.2), the momentum equation becomes:

$$\frac{\partial \mathbf{u}(t,z)}{\partial t} + if\mathbf{u}(t,z) - \frac{\partial}{\partial z}\left(K(z)\frac{\partial \mathbf{u}(t,z)}{\partial z}\right) = 0, \tag{4.10}$$

where the turbulent viscosity K is chosen to be dependent on depth only. In essence, the consideration of different physics for the Ekman layer is reflected in the choice of the vertical dependence for K. Notably, Ekman (1905), Thomas (1975), Madsen (1977), Jordan and Baker (1980) and Lewis and Belcher (2004) all solved Eq. (4.10) explicitly for $\mathbf{u}(t,z)$ using a variety of vertical profiles for $K(z)$ and applying several types of boundary conditions. Lewis and Belcher's 2004 derivations of the time-dependent solutions show that if a constant wind-stress boundary condition is employed, then the lower boundary condition controls the damping scale, viscous or inertial, of the transient terms (in the form of inertial oscillations). Here, the analytical forms of the transfer functions for a given vertical profile of $K(z)$ are also controlled by the bottom boundary condition. Here, we have sought solutions of Eq. (4.10) in the spectral domain for stationary rotating wind stress. For common cases, the spectral solutions presented here are modified versions of the time-mean terms of the solutions presented by the aforementioned authors.

The principle to obtain $\mathbf{H}$ for each of the theoretical models is the following: Eq. (4.10) is Fourier transformed to obtain an ordinary differential equation in z for $\mathbf{U}(\nu,z)$:

$$i(2\pi\nu + f)\mathbf{U}(\nu,z) - \frac{d}{dz}\left[K(z)\frac{d\mathbf{U}(\nu,z)}{dz}\right] = 0. \tag{4.11}$$

Then, using the Fourier transformed boundary conditions, a solution for $\mathbf{U}(\nu,z)$ is found in the form:

$$\mathbf{U}(\nu,z) = \mathbf{H}(\nu,z)\mathbf{T}(\nu), \tag{4.12}$$

where $\mathbf{T}(\nu)$ is the Fourier transform of the wind stress. The mathematical details of deriving the transfer functions for models (1-a,b,c) and (2-a,b,c) are omitted here because similar derivations have been published previously (e.g. Gonella, 1972; Thomas, 1975; Madsen, 1977; Weller, 1981; Lewis and Belcher, 2004). The transfer functions for models (3-a,b,c), to the best of our knowledge, is a new result but their derivations is trivial[1].

4.3.2 Parameterization of the vertical viscosity

We consider nine models arising from three different vertical profiles for $K(z)$, and three different bottom boundary conditions. These models are sketched in Fig. 4.1. The model number (1,2 and 3) designates the vertical profile of K and the letters (a,b and c) indicate the bottom boundary condition.

Models (1-a,b,c) have a constant viscosity $K = K_0$, as shown in the top row of Fig. 4.1. This simple choice was proposed by Ekman (1905). He realized that the value for K_0 could not be the molecular one of water, but a much larger one and that it should depend on the strength of the wind. A remarkable consequence of a constant viscosity in an infinite depth ocean is that the modeled velocity at the surface is always deflected 45° from the wind stress direction, independently of the frequency of the motion.

Models (2-a,b,c) have a viscosity that increases linearly with depth and that vanishes at the surface since $K(z) = K_1 z$. One physical argument in favor of a linear increase from zero at the surface is the concept of turbulent mixing length. Deeper in the water column, turbulent eddies caused by the wind are larger, and hence the turbulent viscosity is larger (e.g. Prandtl, 1952). For small z, it will be seen that this implies that the velocity should follow a logarithmic profile as for a wall-bounded shear flow (e.g. Kundu and Cohen, 2002, p. 528). Tennekes (1973) pointed out that for the atmospheric boundary layer, a logarithm law for the wind profile arises from matching asymptotically a surface-layer and a planetary boundary layer and that a linear profile for K can be derived from it. This type of profile is observed in the atmosphere and it seems sensible to think that this could apply to the oceanic boundary layer. It was theoretically investigated for an infinite depth ocean first by Madsen (1977) and is part of

---

[1] Lewis and Belcher (2004) did consider the case of a non vanishing K at the surface by equivalently considering a water-side surface roughness. However, they considered a coupled oceanic-atmosphere Ekman log-layer which is one step further in complexity for the analytical solution.

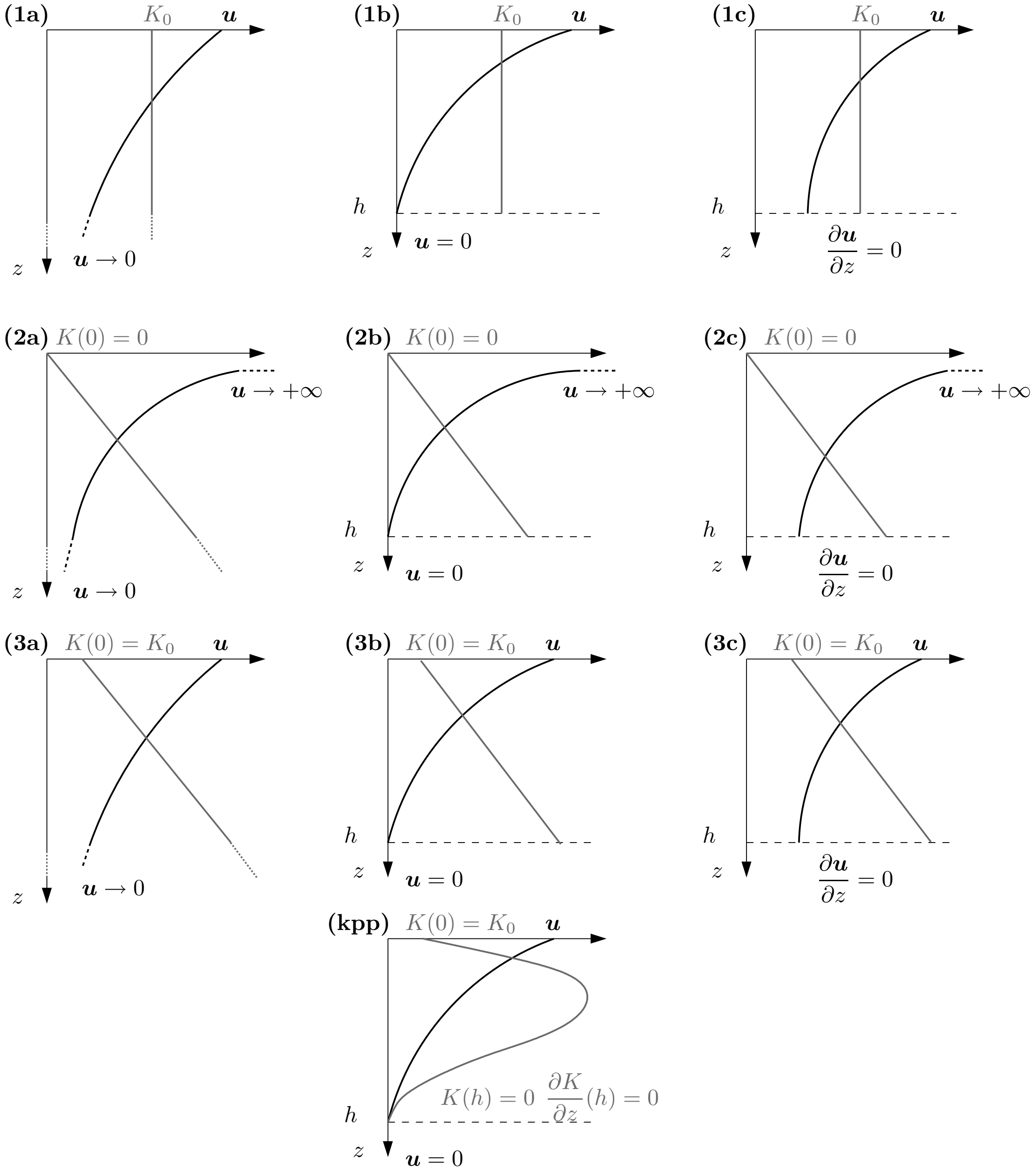

Figure 4.1: Schematics of the models. Black curves: velocity profiles. Gray curves: K profiles. $K = K_0$: models (1a,b,c); $K = K_1 z$, models (2a,b,c); $K = K_0 + K_1 z$, models (3a,b,c); $K = K_0 + K_1 z + K_1 2z^2 + K_3 z^3$, model (kpp).

the many parameterizations also studied theoretically by Jordan and Baker (1980). For a linearly increasing $K(z)$, the dependence on the atmospheric forcing can be accounted for, and Madsen (1977) suggested that $K_1 = \kappa u_*$ where $u_* = \sqrt{\boldsymbol{\tau}(0)/\rho}$ is the shear or friction velocity and $\kappa \approx 0.4$ is the Von Kàrmàn constant (e.g. Kundu and Cohen, 2002). Thomas (1975) considered an upside-down version of this model and suggested that in the shallow water case, since turbulent eddies are inhibited at the bottom, K is zero there and should increase linearly towards a maximum at the top where the wind stress is driving turbulence. Craig et al. (1993) combined these two approaches by investigating numerically a bilinear profile with K increasing linearly both from top and bottom. In these last two studies, the relevance of the depth of frictional influence of the wind stress with respect to the water depth was noted for the resulting velocity profile with depth.

Models (3-a,b,c) have a viscosity that is finite at the surface and that increases with depth: $K(z) = K_0 + K_1 z$, as shown in the third row of Fig. 4.1. The models and transfer functions bear the same general characteristics as models (2-a,b,c). However, these models allow the top boundary condition to be satisfied exactly without requiring approximations of the general solutions close to the surface. Moreover, the separation of K into a constant and a linear part potentially allows us to model other physical processes. As previous and current results both show, the coefficients K_0 and K_1 can be related to different external environmental parameters. In the case of a constant vertical viscosity, one can imagine that the influences of different factors (e.g. wind stress magnitude, latitude, wave heights) will combine into a single value for K which then could be characterized as an effective viscosity. As will be seen, in the derivation of the transfer function for these models, the ratio $z_0 = K_0/K_1$ appears naturally, and can be interpreted as the height of a sub-layer just below the surface that is affected by wave-related processes (e.g. Craig, 1996; Stips et al., 2005).

For the 9 models, the analytical solutions of Eq. (4.11) are available and the subsequent theoretical transfer functions are given. The tenth model derives from a third-order polynomial in z for the vertical viscosity $K(z) = K_0 + K_1 z + K_2 z^2 + K_3 z^3$, akin to the one implemented in the oceanic KPP of Large et al. (1994). This profile was proposed by O'Brien (1970) for the Ekman layer in the top part of the atmospheric boundary layer, on the dynamical ground of having a continuous and smooth viscosity profile across the atmospheric boundary layer. As such, specific bottom boundary conditions are applied for K itself as described below. No analytical solution was sought for this case and the solutions were obtained by numerical integration.

4.3.3 Boundary conditions

For all models, the boundary condition at the surface and its corresponding Fourier transform are:

$$-K(z)\frac{\partial \mathbf{u}(t,z)}{\partial z} = \frac{\boldsymbol{\tau}(t)}{\rho} \quad \leftrightarrow \quad -K(z)\frac{d\mathbf{U}(\nu,z)}{dz} = \frac{\mathbf{T}(\nu)}{\rho}, \quad z = 0. \tag{4.13}$$

This condition cannot be satisfied exactly when K vanishes at $z = 0$ (models (2-a,b,c)) and is taken as a limit.

For the bottom boundary condition, the three cases considered are:

1. Models (1,2,3-a) are for a homogeneous ocean of infinite depth and the corresponding bottom boundary condition is that the wind-driven velocity tends to zero as $z \to +\infty$:

$$\mathbf{u}(t,z) \xrightarrow[z \longrightarrow +\infty]{} 0 \quad \leftrightarrow \quad \mathbf{U}(\nu,z) \xrightarrow[z \longrightarrow +\infty]{} 0. \tag{4.14}$$

2. Models (1,2,3-b) and model (kpp) are 1-layer models, with a homogeneous wind-driven finite layer of thickness h, at the bottom of which the velocity goes to zero.

$$\mathbf{u}(t,z) \xrightarrow[z \longrightarrow h]{} 0 \quad \leftrightarrow \quad \mathbf{U}(\nu,z) \xrightarrow[z \longrightarrow h]{} 0 \tag{4.15}$$

3. Models (1,2,3-c) are 1 and 1/2-layer models, consisting of a homogeneous wind-driven layer of thickness h, at the bottom of which the stress and hence the velocity shear go to zero, but non-zero velocity is still possible. Price and Sundermeyer

(1999) used this bottom boundary condition to study the influence of stratification on Ekman layers.

$$\frac{\partial \mathbf{u}(t,z)}{\partial z} \xrightarrow[z \longrightarrow h]{} 0 \quad \leftrightarrow \quad \frac{d\mathbf{U}(\nu,z)}{dz} \xrightarrow[z \longrightarrow h]{} 0. \tag{4.16}$$

4.3.4 Constant eddy viscosity models

For $K = K_0$, the general solution of Eq. (4.11) is

$$\mathbf{U}(\nu,z) = \mathbf{A}(\nu)e^{-\alpha z} + \mathbf{B}(\nu)e^{+\alpha z} \quad \text{with} \quad \alpha = \sqrt{i\left(\frac{2\pi\nu + f}{K_0}\right)},$$

where $\mathbf{A}(\nu)$ and $\mathbf{B}(\nu)$ are determined by the boundary conditions.

4.3.4.1 Infinite depth ocean: model (1a)

Applying the boundary conditions (4.13) and (4.14), the solution for $\mathbf{U}$ for model (1a) is:

$$\mathbf{U}(\nu,z) = \frac{\mathbf{T}(\nu)}{\rho K_0 \alpha} e^{-\alpha z}.$$

Note that Ekman's steady case is recovered for $\nu = 0$, which gives, for $f > 0$ in the Northern Hemisphere:

$$\mathbf{U}(0,z) = \frac{\mathbf{T}(0)}{\rho\sqrt{K_0 f}}\, e^{-i\pi/4} e^{-z(1+i)\sqrt{\frac{f}{2K_0}}}.$$

The inverse Fourier transform of $\mathbf{U}(0,z)$ gives the Ekman spiral solution, independent of time:

$$\mathbf{u}(z) = \frac{\boldsymbol{\tau}(0)}{\rho\sqrt{K_0 f}}\, e^{-i\pi/4} e^{-z(1+i)/\delta_e},$$

where

$$\delta_e = \sqrt{\frac{2K_0}{f}}, \tag{4.17}$$

is the exponential decay scale. It is related to the "Depth of Wind-currents" $D_E = \pi|\delta_e|$ defined by Ekman (1905), which is the depth at which the velocity is opposite in direction to the velocity at the surface.

At non-zero frequencies, this depth scale is modified and we define:

$$\delta_1(\nu) = \sqrt{\frac{2K_0}{2\pi\nu + f}}, \tag{4.18}$$

and $\delta_1(0) = \delta_e$. Here, δ_1 and δ_e are formally complex numbers and are either pure real or pure imaginary numbers depending on the signs of $2\pi\nu + f$ and f. This means that $\mathbf{H}(\nu, 0)$ is located in the first or fourth quadrant of the complex plane. As explained in section 4.2, the phase and magnitude of $\mathbf{H}$ can readily be interpreted as the deflection from the wind stress direction and the speed of the currents, and this implies that the surface velocity should be either to the left or the right of the wind stress vector. From now on, when discussing these variables as depth scales, we actually refer to their absolute values.

The transfer function for model (1a) can therefore be written:

$$\mathbf{H}_{1\mathrm{a}}(\nu, z) = \frac{\mathbf{U}(\nu, z)}{\mathbf{T}(\nu)} = \frac{e^{-i\pi/4} e^{-z(1+i)/\delta_1}}{\rho\sqrt{(2\pi\nu + f)K_0}}. \tag{4.19}$$

This expression shows the dependence of the ocean response on the frequency ν of the forcing, the depth z and the parameters f, ρ, and especially K_0. This transfer function was first derived by Gonella (1972).

The frequency dependence is best illustrated graphically. Fig. 4.2 shows the transfer functions for models (1-a,b,c), Fig. 4.3 for models (2-a,b,c), Fig. 4.4 for models (3-a,b,c) and Fig. 4.5 for model (kpp). These transfer functions are plotted both as a function of frequency and of depth, evaluated with the optimum parameter values found to fit the observations. For legibility we do not plot all the frequency bands resolved in our spectral analysis but only those from -1.95 to 1.95 cpd at 0.075 cpd intervals. Each of these frequencies is colored coded, and plotted as a line showing the variation of $\mathbf{H}$ with depth. This is analogous to the velocity hodograph as a function of depth, and indicates the vertical shear. Gray dots show the theoretical transfer function at 15 m, and these can be compared to the observed transfer function obtained from drifter data plotted in the lower-right panel of each of these figures. For models (1-a,b,c), the transfer functions at the surface for continuous frequencies from -2 cpd to 2 cpd are drawn with thick dashed curves. For model (1c), the transfer function at the bottom of the boundary layer is also drawn. Since this study focuses on the Southern Ocean, we considered cases with $f < 0$ and where the mean Ekman current is to the left of the wind.

The top left panel of Fig. 4.2 shows the transfer function $\mathbf{H}_{1\mathrm{a}}$ fitted at 53°S. At this latitude, the optimization indicates a best estimate of $K_0 = 1.35\ \mathrm{m}^2\ \mathrm{s}^{-1}$. This value is large and, as a consequence the velocity shear is relatively small, and the velocity hodograph is a spiral that extends very deep. In general, the velocity spirals smoothly from the surface and vanishes at infinite depth for all frequencies. For cyclonic ($\nu < 0$) and sub-inertial anticyclonic frequencies ($0 < \nu < -f/2\pi$, recall $f < 0$), the velocity starts to the left of the wind stress and spirals anticylonically, while for supra-inertial anticyclonic frequencies ($\nu > -f/2\pi$), the spiral starts to the right of the wind and spirals cyclonically.

The exponential decay depth $\delta_1(\nu)$, where the current speed is $1/e$ (about 37%) of its surface value and the current vector has rotated by 1 radian ($\approx 57.3°$), is about 157 m at zero frequency, 25 m at 1 cpd in the cyclonic domain but 250 m in the anticyclonic domain, and goes to infinity as $\nu \rightarrow -f/2\pi$. At the surface, as $\nu \rightarrow -f/2\pi$,

$$\mathbf{H}_{1\mathrm{a}} \sim \frac{e^{-i\pi/4}}{\rho\sqrt{(2\pi\nu + f)K_0}},$$

implying that the transfer function exhibits a singularity, its phase tends to 45°, and its magnitude goes to infinity, typical of the resonance of an oscillator at its natural frequency. Since this resonance peak is located in the anticyclonic frequency domain, this model, like the others, predicts a stronger response of the ocean to wind stress forcing for all anticyclonic frequencies compared to the corresponding cyclonic frequencies.

Indeed, model (1a) imposes the angle at the surface to be 45° for all frequencies and requires it to increase with depth. This is in disagreement with the angle for the observed transfer function at 15 m, which for the data at 53°S is plotted in the lower-right panel of Fig. 4.2. This shows that model (1a) is incapable of accommodating such

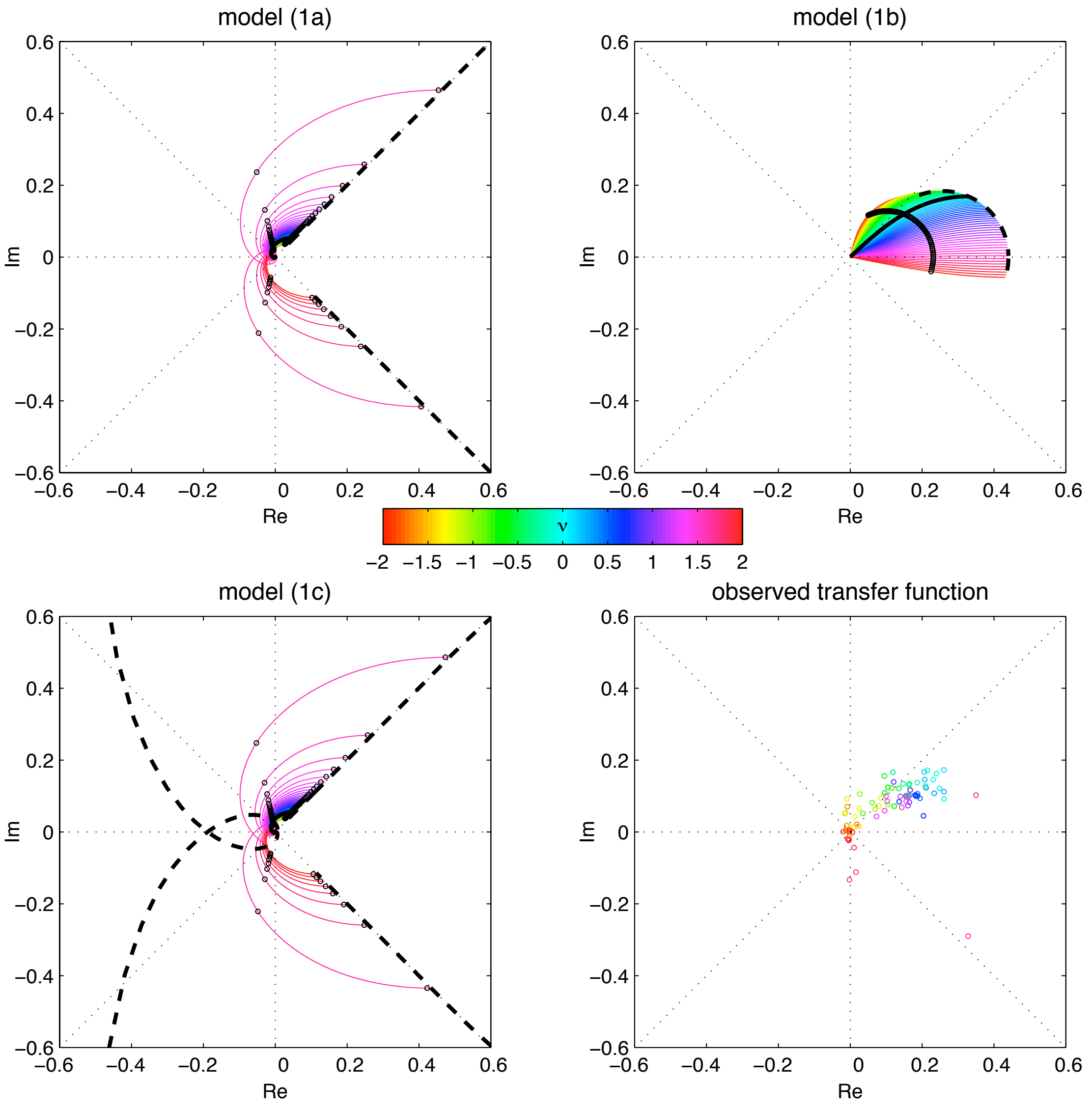

Figure 4.2: Transfer functions for model (1a) with $K_0 = 1.3$ m^2 s^{-1}; model (1b) with $K_0 = 698$ cm^2 s^{-1} and $h = 32$ m; model (1c) with $K_0 = 1.24$ m^2 s^{-1} and $h = 4297$ m; $f = -1.16 \times 10^{-4}$ s^{-1} corresponding to the 52-54°S latitudinal band. Each curve is the transfer function as a function of depth for frequencies $\nu = -1.95 \ldots 1.95$ cpd at 0.05 cpd interval. The color of each curve corresponds to the frequency indicated by the colorscale on the colorbar. For these three models, the solid black curve is for $\nu = 0$. The transfer function at 15 m is indicated by a black dot on each curve for each model. In addition, the transfer function at the depth scale δ_1 is indicated also by a black dot for models (1a) and (1c). The heavy dashed curve joins the $z = 0$ m points for all frequencies for models (1a), (1b) and (1c). For model (1c) a heavy dashed curve also joins the $z = h$ points. The dotted lines indicate the x and y axes and the $\pm$ 45° directions. The observed transfer function at 53°S is plotted in the lower-left panel for all the frequencies resolved ($\nu = -1.95 \ldots 1.95$ cpd at 0.025 cpd interval).

small angles and predicts very large viscosity K_0 to minimize the shear from the surface to 15 m. It performs therefore poorly, and it actually returns the largest cost function values at all latitudes (see panel d) of Fig. 4.7), making it the worst model considered here.

4.3.4.2 1 layer model: model (1b)

Applying the boundary conditions (4.13) and (4.15), the transfer function for model (1b) is:

$$\begin{aligned}\mathbf{H}_{1\mathrm{b}}(\nu, z) &= \frac{1}{\rho K_0 \alpha} \frac{\sinh[\alpha(h-z)]}{\cosh[\alpha h]} \\ &= \frac{e^{-i\pi/4}}{\rho\sqrt{(2\pi\nu + f)K_0}} \frac{\sinh\left[(1+i)(h-z)/\delta_1\right]}{\cosh\left[(1+i)h/\delta_1\right]}.\end{aligned} \tag{4.20}$$

$\mathbf{H}_{1\mathrm{b}}$ is plotted in the top-right panel of Fig. 4.2 using the results of the fit at 53°S, which are $K_0 = 698\ \mathrm{cm}^2\ \mathrm{s}^{-1}$ and $h = 32$ m. For this model, the boundary layer depth h allows the velocity deflection at the surface and below to be less than 45°, which is in better agreement with the observations.

Compared to model (1a), K_0 is two orders of magnitude smaller, and the wind-driven layer is quite shallow. The depth scale $\delta_1(\nu)$ is of the same order of magnitude as h, which allows the model to respond to the bottom. For the time-mean, $\delta_1(0)$ is slightly larger than h which causes an angle smaller than 45°. As $\nu \to -f/2\pi$, $\delta_1 \to +\infty$ so that

$$\mathbf{H}_{1\mathrm{b}} \sim \frac{h-z}{\rho K_0},$$

which is a finite real number, meaning that at the inertial frequency the Ekman velocities are aligned with the wind stress at all depths and decrease linearly with depth. In this configuration the "wind rotation" (Crawford and Large, 1996) is tuned to the inertial frequency, and the input of kinetic energy can be maximized. Since this resonant response is finite, the polarization of the response is smaller than for models with an infinite resonance. As an example, the diurnal polarization is predicted to be 1.44 at 53°, in much better agreement with the observations.

The vertical structure of the transfer function at 53°S shows very little resemblance to a spiral, and for $\nu > 0.3$ cpd, the shear is mostly downwind. Only for cyclonic frequencies $\nu < -0.3$ cpd are the cross- and downwind components approximately of similar magnitude.

At the surface, angular deflections of surface currents relative to the wind stress are less than 45° at all frequencies, in contrast to the classic Ekman model (1a). For the time mean velocity profile, the velocity deflection is 27° at the surface and rotates only by about 16° over the depth h.

This model is a substantial improvement over model (1a) described previously and is actually on average the best model to explain our observed transfer functions in the Southern Ocean, as will be discussed in the next section.

4.3.4.3 1 and 1/2 layer model: model (1c)

Applying the boundary conditions (4.13) and (4.16), the transfer function for model (1c) is:

$$\begin{aligned} \mathbf{H}_{1c}(\nu, z) &= \frac{1}{\rho K_0 \alpha} \frac{\cosh[\alpha(h-z)]}{\sinh[\alpha h]} \\ &= \frac{e^{-i\pi/4}}{\rho\sqrt{(2\pi\nu + f)K_0}} \frac{\cosh\left[(1+i)(h-z)/\delta_1\right]}{\sinh\left[(1+i)h/\delta_1\right]}. \end{aligned} \tag{4.21}$$

Gonella (1972) derived the transfer function for this model but in a different form, using image theory and writing the equations in the sense of distributions. Several typographic errors were found in Gonella's paper and the correct expression (with our convention $z > 0$) is:

$$\mathbf{H}(\nu, z) = \frac{1}{ih\rho(2\pi\nu + f)} \sum_{n=-\infty}^{+\infty} e^{-in\pi z/h} \left[1 - i \frac{n^2\pi^2}{h^2 \left(\dfrac{2\pi\nu + f}{K_0} \right)} \right]^{-1}.$$

The equality between these two mathematical expressions is demonstrated in Appendix B.

In the limit $\nu \to -f/2\pi$,

$$\mathbf{H}_{1c} \sim \frac{e^{-i\pi/2}}{\rho h(2\pi\nu + f)},$$

independent of K_0, which implies that wind-driven velocities tend toward infinity at 90° to the left of the wind stress for sub-inertial frequencies and to the right for supra-inertial frequencies. Similarly, Lewis and Belcher (2004) found in the time dependent solution for this model that an undamped mode oscillating at the inertial frequency is excited when an impulsive stress is imposed on an ocean originally at rest, and they consequently abandoned this model as being unphysical. Here, across the Southern Ocean, we find that the optimum values for K_0 are indistinguishable from the ones for model (1a), within error bars. Moreover, the optimum values for h are O(10^3 m), which seems unlikely at the local scale even in neutral buoyancy conditions, and as a consequence $\mathbf{H}_{1\mathrm{c}} \approx \mathbf{H}_{1\mathrm{a}}$. In the end, this model performs only marginally better than model (1a) (see panel d of Fig. 4.7) even though it introduces a new degree of freedom. Therefore, we will not further discuss the results of this model.

4.3.5 Linear viscosity models

For $K = K_1 z$, the general solution of Eq. (4.11) is:

$$\mathbf{U}(\nu, z) = \mathbf{A}(\nu)\mathcal{I}_0\left(2\sqrt{\frac{iz}{\delta_2}}\right) + \mathbf{B}(\nu)\mathcal{K}_0\left(2\sqrt{\frac{iz}{\delta_2}}\right),$$

where $\mathcal{I}_n$ and $\mathcal{K}_n$ are the nth-order modified Bessel functions of the first and second kind, respectively, and

$$\delta_2(\nu) = \frac{K_1}{2\pi\nu + f},$$

is the depth scale for models (2a,b,c). The limiting behaviors for small arguments of the zeroth and first order modified Bessel functions are summarized in Table 4.1 as a reference to aid interpreting the approximations discussed in the next subsections for models (2a,b,c) and (3a,b,c).

Table 4.1: Limiting behaviors for small argument of the zeroth and first orders modified Bessel functions of the first and second kinds. γ is the Euler constant.

	$\mathcal{I}_0(\xi)$	$\mathcal{K}_0(\xi)$	$\mathcal{I}_1(\xi)$	$\mathcal{K}_1(\xi)$
$\|\xi\| \rightarrow 0$	1	$-\ln\left(\frac{\xi}{2}\right)-\gamma$	$\xi/2$	ξ^{-1}

4.3.5.1 Infinite depth ocean: model (2a)

The boundary condition (4.14) imposes $\mathbf{A}(\nu)=0$ for model (2a). The boundary conditions (4.13) is taken in the limit $z \rightarrow 0$, and using a first-order approximation for the derivative of the Bessel functions one finds that $\mathbf{B}(\nu) = 2\mathbf{T}(\nu)/(\rho K_1)$, and consequently the transfer function for model (2a) is:

$$\mathbf{H}_{2\mathrm{a}}(\nu,z)=\frac{2}{\rho K_1}\mathcal{K}_0\left(2\sqrt{\frac{iz}{\delta_2}}\right). \tag{4.22}$$

$\mathbf{H}_{2\mathrm{a}}$ is plotted in the top left panel of Fig. 4.3, fitted to the data at 53°S with $K_1 = 1.23$ cm s^{-1}. The predicted polarization at 53°S for diurnal forcing is r^{-1} =1.93, in better agreement with the observations.

Madsen (1977) and Lewis and Belcher (2004) both derived this transfer function in Laplace transform form and inverted it to obtain the time dependent solution in the oceanic boundary layer. The frequency dependence for $\mathbf{H}_{2\mathrm{a}}$ is embedded in the non-dimensional depth $z/\delta_2(\nu)$ so that the velocity hodographs all collapse onto one curve spiraling slowly towards zero at infinite depth. As $z/\delta_2(\nu) \rightarrow 0$, for either $z \rightarrow 0$ or $\nu \rightarrow -f/2\pi$, retaining the first term of a series expansion for $\mathcal{K}_0$ around 0, one can approximate the transfer function (Bender and Orszag, 1999):

$$\mathbf{H}_{2\mathrm{a}}(\nu,z)\sim\frac{2}{\rho K_1}\left[-\ln\left(\sqrt{\frac{iz}{\delta_2}}\right)-\gamma\right], \tag{4.23}$$

where $\gamma \approx 0.5772\cdots$ is the Euler constant. For $\nu < -f/2\pi$ one can write $\delta_2 = -|\delta_2|$ and

$$\mathbf{H}_{2\mathrm{a}}(\nu,z)\sim\frac{1}{\rho K_1}\left[i\frac{\pi}{2}-\ln\left(\frac{z}{|\delta_2|}\right)-\gamma\right], \quad \frac{z}{\delta_2}\rightarrow 0. \tag{4.24}$$

This expression shows that for small z/δ_2, the imaginary part of the transfer function tends to a constant while the downwind component is logarithmic and eventually goes

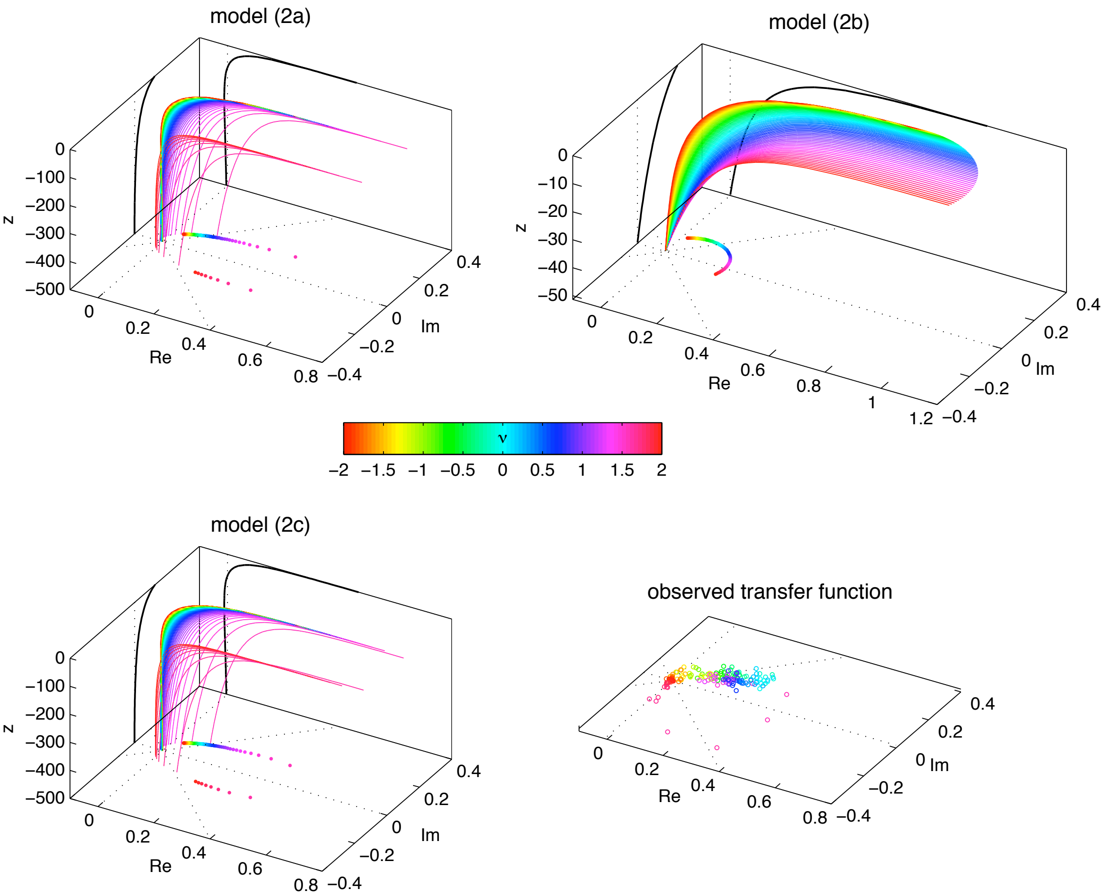

Figure 4.3: Transfer functions for model (2a) with $K_1 = 1.23 \times 10^{-2}$ m s^{-1}; model (2b) with $K_1 = 0.57 \times 10^{-2}$ m s^{-1}and $h = 51$ m; model (2c) with $K_0 = 1.20 \times 10^{-2}$ m s^{-1}and $h = 10000$ m; $f = -1.16 \times 10^{-4}$ s^{-1} corresponding to the 52°-54° latitudinal band. See also the caption for Fig. 4.2. The theoretical transfer functions at 15 m depth are projected on the plane coinciding with the bottom of the axes. The real part of the transfer functions at $\nu = 0$ is projected on the (x,z) plane and the imaginary part on the (y,z) plane and these curves are drawn in black. Since these transfer functions are not defined at the surface, the curves curves start at the depth $z- = 0.1$ m.

to infinity. This behavior applies for $z/\delta_2(\nu) \ll 1$ and its validity therefore depends on the frequency of the forcing. At zero frequency, at 53°S, we find $\delta_2(0) = 108$ m so that the logarithmic behavior for the downwind component is predicted to extend to within ten meter of the mean sea surface, whereas in the anticyclonic domain at the diurnal frequency, $\delta_2(1) \approx 280$ m which implies that a log-layer would be applicable to the upper 28 m of the water column.

The singularity at the inertial frequency, also found in models (2b) and (2c), is inconvenient because the subsequent surface velocity is not defined. In order to obtain the surface "drift", that is the velocity at the surface, Madsen (1977) evaluated the velocity at a distance z_0 from the theoretical surface. This distance is called the roughness length and for the case of an oceanic boundary layer should correspond to an unresolved sub-layer just beneath the surface where turbulence caused by waves (breaking or not) occurs. The value that this length should take is subject to much debate (e.g. Stips et al., 2005). Reviewing field and laboratory experiments, Madsen (1977) used a roughness length of O(1 cm) and found that only the order of magnitude was relevant since a multiplicative factor of 2 for z_0 changed the surface drift magnitude and angle by only 10%. In the present case, our optimum values for the linear coefficient K_1 are one to two orders of magnitude larger than what was used by Madsen (1977), so that our surface drift is much more sensitive to the choice of z_0. Also, selecting the surface roughness a posteriori can be seen to be inconsistent (Lewis and Belcher, 2004), because in this case the roughness is no longer compatible with the surface boundary condition for the stress (4.13).

4.3.5.2 1 layer model: model (2b)

Applying the boundary conditions (4.13) and (4.15), the transfer function for model 2b is:

$$\mathbf{H}_{2\mathrm{b}}(\nu, z) = \frac{2}{\rho K_1} \times \left[\mathcal{K}_0\left(2\sqrt{\frac{iz}{\delta_2}}\right) - \frac{\mathcal{K}_0\left(2\sqrt{\frac{ih}{\delta_2}}\right)\mathcal{I}_0\left(2\sqrt{\frac{iz}{\delta_2}}\right)}{\mathcal{I}_0\left(2\sqrt{\frac{ih}{\delta_2}}\right)} \right]. \tag{4.25}$$

$\mathbf{H}_{2\mathrm{b}}$ is plotted in the top right panel of Fig. 4.3, for the results of the fit at 53°S, which are $K_1 = 5.7 \times 10^{-3}$ cm s^{-1} and $h = 51$ m.

From expression (4.25), it can be seen that as $z \rightarrow 0$, $\mathcal{I}_0\left(2\sqrt{\frac{iz}{\delta_2}}\right) \rightarrow 1$ so that, near the surface, model (2b) is like model (2a) plus a complex constant function of h and $\delta_2(\nu)$, which is hence a function of frequency.

Near the inertial frequency, i.e as $\nu \rightarrow -f/2\pi$ and $\delta_2 \rightarrow +\infty$,

$$-\frac{\mathcal{K}_0\left(2\sqrt{\frac{ih}{\delta_2}}\right)\mathcal{I}_0\left(2\sqrt{\frac{iz}{\delta_2}}\right)}{\mathcal{I}_0\left(2\sqrt{\frac{ih}{\delta_2}}\right)} \sim -i\frac{\pi}{2} + \ln\left(\frac{h}{\delta_2}\right) + \gamma. \tag{4.26}$$

This limit can be combined with the limit of the first term in the square brackets in the right-hand side of Eq. (4.25) and it is found that

$$\mathbf{H}_{2\mathrm{b}} \sim -\frac{1}{\rho K_1}\ln\left(\frac{z}{h}\right), \quad \nu \rightarrow -\frac{f}{2\pi}. \tag{4.27}$$

For this model, near the inertial frequency, the oceanic boundary layer behaves like a logarithmic layer and there is no cross-wind component. Since the depth scale is much larger than h, h determines the magnitude of the response.

4.3.5.3 1 and 1/2 layer model - model (2c)

Applying the boundary conditions (4.13) and (4.16), the transfer function for model (2c) is:

$$\mathbf{H}_{2\mathrm{c}}(\nu, z) = \frac{2}{\rho K_1} \times \left[\mathcal{K}_0\left(2\sqrt{\frac{iz}{\delta_2}}\right) + \frac{\mathcal{K}_1\left(2\sqrt{\frac{ih}{\delta_2}}\right)\mathcal{I}_0\left(2\sqrt{\frac{iz}{\delta_2}}\right)}{\mathcal{I}_1\left(2\sqrt{\frac{ih}{\delta_2}}\right)} \right]. \tag{4.28}$$

$\mathbf{H}_{2c}$ is plotted in the lower left panel of Fig. 4.3 for the fit at 53°S with $K_1 = 1.20$ cm^2 s^{-1} and $h = 10^4$ m.

For this model since the optimum values for h are O(10^4 m), at all frequencies,

$$\frac{\mathcal{K}_1\left(2\sqrt{\frac{ih}{\delta_2}}\right)\mathcal{I}_0\left(2\sqrt{\frac{iz}{\delta_2}}\right)}{\mathcal{I}_1\left(2\sqrt{\frac{ih}{\delta_2}}\right)} \approx 0, \tag{4.29}$$

and $\mathbf{H}_{2c} \approx \mathbf{H}_{2a}$.

There is no significant difference in the optimum values found for K_1 between model (2a) and (2c). Moreover, this model fails in the sense that the optimum values for h are found on the border of the parameter space and the return values for the cost function are slightly larger than for model (2a). As a consequence, we will not further discuss the results for this model.

4.3.6 Linear viscosity models with finite surface value

When the viscosity profile is

$$K = K_0 + K_1 z = K_1(\frac{K_0}{K_1} + z) = K_1(z_0 + z),$$

the general solution to Eq. (4.11) is:

$$\mathbf{U}(\nu, z) = \mathbf{A}(\nu)\,\mathcal{I}_0\left[2\sqrt{\frac{i(z_0+z)}{\delta_2}}\right] + \mathbf{B}(\nu)\,\mathcal{K}_0\left[2\sqrt{\frac{i(z_0+z)}{\delta_2}}\right].$$

For models (3-a,b,c), K_0 takes on a different meaning than for models (1-a,b,c). Here the ratio K_0/K_1 is interpreted as the surface roughness length z_0. First, z_0 is a vertical scale which eliminates the singularity that appeared in models (2-a,b,c) and it consequently reduces the surface velocity and surface gradient to finite quantities. Second, it is suspected to be related to the properties of surface gravity waves, e.g. to be representative of the penetration depth of turbulence bursts input by waves (Csanady, 1997). As will be seen in the results for models (3-a,b,c), we are able to estimate this length scale z_0

on large scales. Further study (beyond the scope of this present work) could relate these estimates to exterior parameters like significant wave height of surface gravity waves, or wavelengths.

4.3.6.1 Infinite depth ocean - model (3a)

Applying the boundary conditions (4.13) and (4.14), the transfer function for model (3a) is

$$\mathbf{H}_{3\mathrm{a}}(\nu, z) = \frac{1}{\rho\sqrt{i(2\pi\nu + f)K_0}} \frac{\mathcal{K}_0\left[2\sqrt{\dfrac{i(z_0+z)}{\delta_2}}\right]}{\mathcal{K}_1\left[2\sqrt{\dfrac{iz_0}{\delta_2}}\right]}. \tag{4.30}$$

$\mathbf{H}_{3\mathrm{a}}$ is plotted for the first 500 m from the surface in the top left panel of Fig. 4.4, for the results of the fit at 53°S, which are $K_0 = 99 \times 10^{-4}$ m^2 s^{-1} and $K_1 = 1.18 \times 10^{-2}$ m s^{-1}. The corresponding roughness length is $z_0 = 0.83$ m.

At the surface, the transfer function is defined and takes on a finite value, in contrast to model (2a). Moreover, as $\nu \to -f/2\pi$

$$\mathcal{K}_1\left[2\sqrt{\frac{iz_0}{\delta_2}}\right] \sim \left(2\sqrt{\frac{iz_0}{\delta_2}}\right)^{-1} = \frac{K_1}{2\sqrt{i(2\pi\nu + f)K_0}}, \tag{4.31}$$

so that

$$\mathbf{H}_{3\mathrm{a}} \sim \frac{1}{\rho K_1}\left[i\frac{\pi}{2} - \ln\left(\frac{z_0}{|\delta_2|}\right) - \gamma\right], \quad \nu \to -\frac{f}{2\pi}. \tag{4.32}$$

It can be seen that this corresponds to the approximate expression for model (2a) evaluated at the depth z_0.

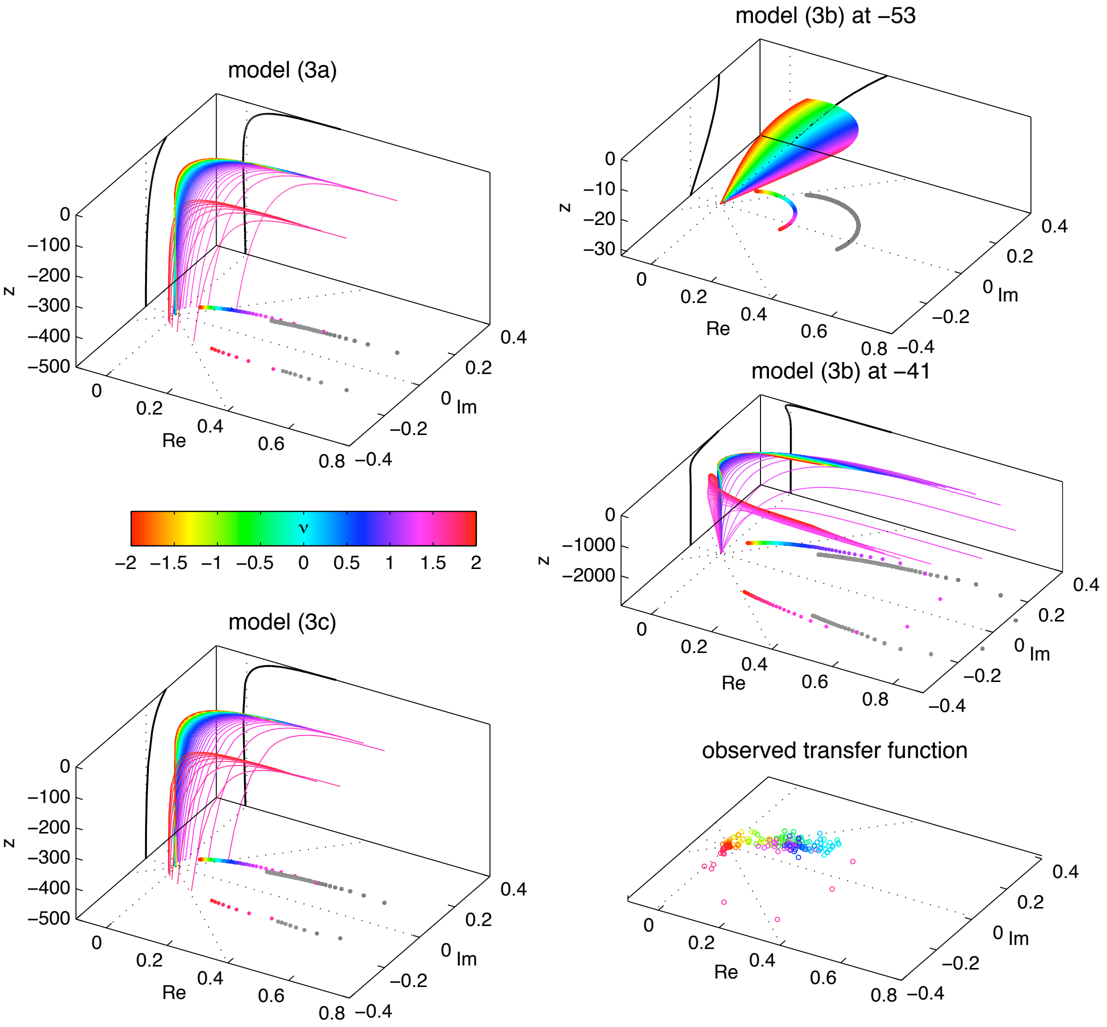

Figure 4.4: Transfer functions for model (3a) with $K_0 = 99 \times 10^{-4}$ m^2 s^{-1}, $K_1 = 1.18 \times 10^{-2}$ m s^{-1}; model (3b) with $K_0 = 722 \times 10^{-4}$ m^2 s^{-1}, $K_1 \approx 0$ m s^{-1}and $h = 32$ m; model (3c) with $K_0 = 123 \times 10^{-4}$ m^2 s^{-1}, $K_1 = 1.17 \times 10^{-2}$ m s^{-1}and $h = 9542$ m; $f = -1.16 \times 10^{-4}$ s^{-1} corresponding to the 52°-54°latitudinal band. Model (3b) is also plotted for the results at 41°S with $K_0 = 203 \times 10^{-4}$ m^2 s^{-1}, $K_1 = 0.72 \times 10^{-2}$ m s^{-1}and $h = 2981$ m; The transfer function at the surface is plotted with gray dots projected on the plane coinciding with the bottom of the axes. See also the captions of Fig. 4.2 and 4.3.

4.3.6.2 1 layer model - model (3b)

Applying the boundary conditions (4.13) and (4.15), the transfer function for model (3b) is

$$\mathbf{H}_{3b}(\nu, z) = \frac{1}{\rho\sqrt{i(2\pi\nu + f)K_0}} \times \\ \frac{\mathcal{I}_0\left[2\sqrt{\frac{i(z_0+h)}{\delta_2}}\right]\mathcal{K}_0\left[2\sqrt{\frac{i(z_0+z)}{\delta_2}}\right] - \mathcal{K}_0\left[2\sqrt{\frac{i(z_0+h)}{\delta_2}}\right]\mathcal{I}_0\left[2\sqrt{\frac{i(z_0+z)}{\delta_2}}\right]}{\mathcal{I}_1\left[2\sqrt{\frac{iz_0}{\delta_2}}\right]\mathcal{K}_0\left[2\sqrt{\frac{i(z_0+h)}{\delta_2}}\right] + \mathcal{K}_1\left[2\sqrt{\frac{iz_0}{\delta_2}}\right]\mathcal{I}_0\left[2\sqrt{\frac{i(z_0+h)}{\delta_2}}\right]}. \tag{4.33}$$

$\mathbf{H}_{3b}$ is plotted in the top right panel of Fig. 4.4, for the results of the fit at 53°S, which are $K_0 = 722 \times 10^{-4}$ m^2 s^{-1}, $K_1 = 1.13 \times 10^{-5}$ m s^{-1}, and $h = 32$ m. At this latitude, as at all latitudes south of 50°S, the optimization returns values for K_1 that are barely significantly different from zero, given our tolerance value (10^{-5}) for the parameter space search in the optimization procedure (see Appendix A.3). Moreover, for these latitudes, the optimum values for K_0 and h do not differ statistically for models (1b) and (3b). This is physically consistent with the fact that model (3b) is equivalent to model (1b) if $K_1 \rightarrow 0$.

To the north of 50°S, model (3b) shows a very different behavior, as the values of K_1 are commensurate with the optimum values of model (3a) or (3c) (see next sections) but with an physically questionable average value for h of approximately 3000 m. In order to illustrate the different behavior of this model according to the latitude, $\mathbf{H}_{3b}$ is also plotted in the middle right panel of Fig. 4.4, for the results of the fit at 41°S, which are $K_0 = 203 \times 10^{-4}$ m^2 s^{-1}, $K_1 = 0.72 \times 10^{-2}$ m s^{-1}, and $h = 2981$ m, and the corresponding roughness length is $z_0 = 2.8$ m.

The transfer function for model (3b) is defined at the surface and takes on a finite value which can be evaluated. Also, at the surface, as $\nu \rightarrow -f/2\pi$

$$\mathbf{H}_{3b} \sim -\frac{1}{\rho K_1}\ln\left(\frac{z_0}{z_0+h}\right). \tag{4.34}$$

This asymptotic behavior is hardly justifiable or applicable here considering that little weight is given to the observed frequency response close to the inertial frequency. Also, evaluating the roughness length at 53°S gives $z_0 = 6362$ m, a numerical value that clearly has no relationship to the thickness of a surface layer influenced by waves.

4.3.6.3 1 and 1/2 layer model - model (3c)

Applying the boundary conditions (4.13) and (4.16), the transfer function for model (3c) is

$$\mathbf{H}_{3\mathrm{c}}(\nu, z) = \frac{1}{\rho\sqrt{i(2\pi\nu + f)K_0}} \times \frac{\mathcal{K}_1\left[2\sqrt{\frac{i(z_0+h)}{\delta_2}}\right]\mathcal{I}_0\left[2\sqrt{\frac{i(z_0+z)}{\delta_2}}\right] + \mathcal{K}_0\left[2\sqrt{\frac{i(z_0+h)}{\delta_2}}\right]\mathcal{I}_1\left[2\sqrt{\frac{i(z_0+z)}{\delta_2}}\right]}{\mathcal{K}_1\left[2\sqrt{\frac{iz_0}{\delta_2}}\right]\mathcal{I}_1\left[2\sqrt{\frac{i(z_0+h)}{\delta_2}}\right] - \mathcal{I}_1\left[2\sqrt{\frac{iz_0}{\delta_2}}\right]\mathcal{K}_1\left[2\sqrt{\frac{i(z_0+h)}{\delta_2}}\right]}. \tag{4.35}$$

$\mathbf{H}_{3\mathrm{c}}$ is plotted for the upper 500 m in the lower left panel of Fig. 4.4, using the results of the fit at 53°S, which are $K_0 = (120 \pm 90) \times 10^{-4}$ m^2 s^{-1}, $K_1 = (1.17 \pm 0.07) \times 10^{-2}$ m s^{-1}, and $h = (9500 \pm 800)$ m. These values should be interpreted with care given the size of the statistical error bars for K_0 and h.

Since the optimum values for h across the Southern Ocean are generally O(10^4m), for all frequencies

$$\mathbf{H}_{3\mathrm{c}} \sim \mathbf{H}_{3\mathrm{a}}.$$

As such, there is no significant difference in the optimum K_0 and K_1 between models (3c) and (3a). As for all models with the zero-shear bottom boundary condition (4.15), model (3c) fails to improve on model (3a).

4.3.7 Cubic profile model

We consider now the transfer function obtained when the vertical profile for K is a cubic polynomial "shape" function (O'Brien, 1970):

$$K(z) = K_0 + K_1 z + K_2 z^2 + K_3 z^3, \tag{4.36}$$

which is applied over a layer of thickness h, with the conditions for the viscosity at the bottom of the boundary layer:

$$K(h) = 0, \quad \frac{\partial K}{\partial z}(h) = 0,$$

which give:

$$K_2 = -3\frac{K_0}{h^2} - \frac{K_1}{h}, \quad K_3 = 2\frac{K_0}{h^3} + \frac{K_1}{h^2}.$$

These expressions for K_2 and K_3 are used in (4.36) so that the three parameters K_0, K_1 and h completely determine the vertical profile. In addition, the boundary conditions (4.13) and (4.15) are applied. We did not seek an analytic solution to Eq. (4.11) for this profile but instead solved numerically for $\mathbf{U}(\nu, z)$ using standard techniques, with a centered-difference discretization scheme of the differential Eq. 4.11. By setting the magnitude of the wind stress to unity for each frequency band, $\mathbf{U}(\nu, z)$ is equal to the transfer function $\mathbf{H}_{\text{kpp}}(\nu, z)$. In order to ensure sufficient numerical accuracy, the numerical algorithm was tested for model (3b) for which an analytical solution for the transfer function is available. This showed that with a 20 cm resolution, the difference between the numerical and analytical solutions was less than the uncertainty in L (see appendix A).

$\mathbf{H}_{\text{kpp}}$ is plotted in Fig. 4.5 for the results of the fit at 53°S, which are $K_0 = 183 \times 10^{-4}$ m^2 s^{-1}, $K_1 = 1.20 \times 10^{-2}$ m s^{-1}, and $h = 10000$ m. The optimum values found across the Southern Ocean for this model are all $O(10^4$ m) and as a consequence $K(z) \approx K_0 + K_1 z$ and this model behaves similarly to models (3a) and (3c).

This is the profile implemented in the KPP model of Large et al. (1994). However, we are not considering the complete KPP model since no freshwater, heat or radiative fluxes, or convection processes are considered. Moreover, we let the boundary layer

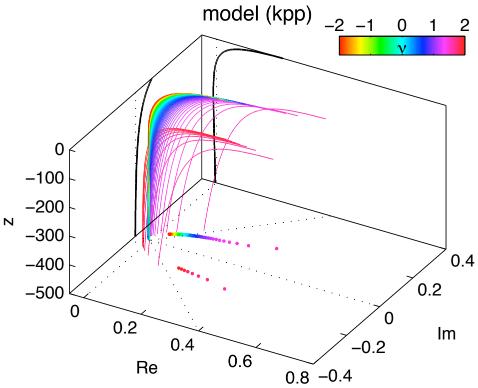

Figure 4.5: Transfer function for model (kpp) with $K_0 = 183 \times 10^{-4}$ m^2 s^{-1}, $K_1 = 1.20 \times 10^{-3}$ m s^{-1}, and $h = 10^4$ m corresponding to the 52°-54°latitudinal band. See also the caption for Fig. 4.2. The real part of the transfer functions at $\nu = 0$ is projected on the (x,z) plane and the imaginary part on the (y,z) plane.

depth h, over which the profile (4.36) is stretched, be a free parameter. This is different from an usual implementation of KPP, where h is diagnosed as the depth at which a bulk Richardson number takes on a critical value representative of the fact that the local stratification inhibits further penetration of the turbulent eddies. Also, in KPP, for stable forcing, h is required to be less than or equal to $0.7u_*/f$, which is not specified here.

4.4 Polarization of the ocean's response

A major characteristic of the observed transfer function, as well as the theoretical transfer functions derived in the previous section is the stronger response for anticyclonic forcing than for cyclonic forcing by the wind stress.

Fig. 4.6 shows, for each of the models presented in section 4.3, the ratio r of the absolute value of the transfer function at 15 m for cyclonic frequencies to the absolute value of the transfer function at the corresponding anticyclonic frequencies:

$$r(|\nu|) = \frac{|\mathbf{H}(\nu < 0)|}{|\mathbf{H}(\nu > 0)|}. \tag{4.37}$$

If the spectrum of the wind stress forcing were white, then r would be the ratio of the ocean cyclonic current speeds to the corresponding anticyclonic current speeds. As

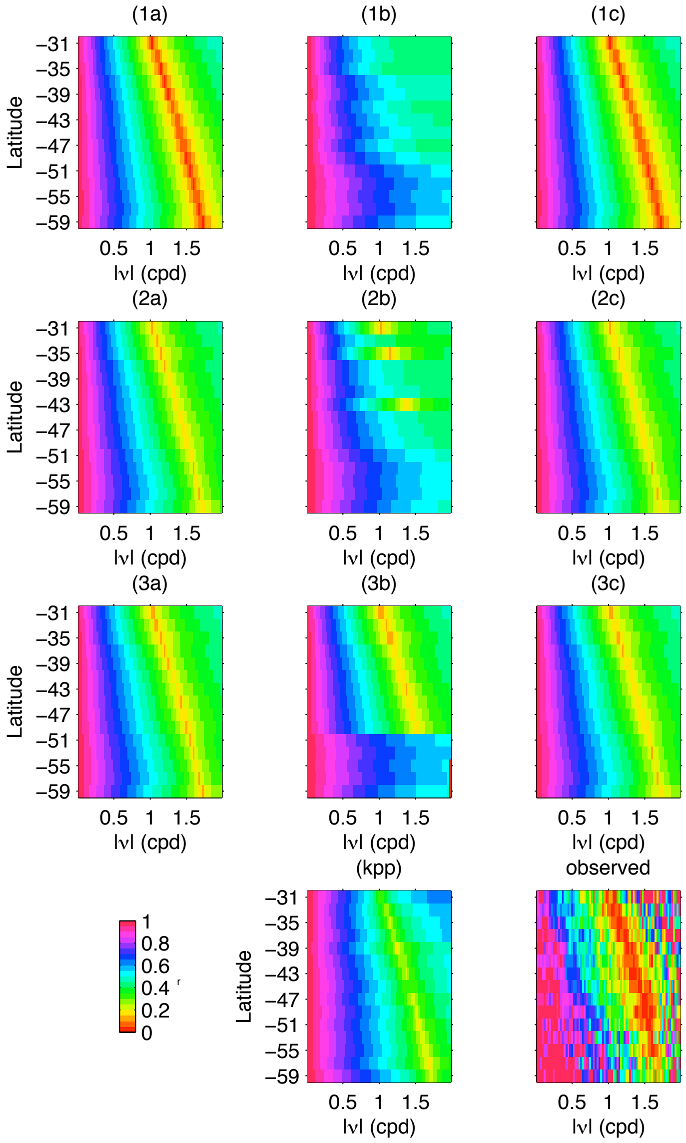

Figure 4.6: Polarization of the transfer function: ratio of the absolute value of the transfer function at cyclonic frequencies to the transfer function at the corresponding anticyclonic frequencies $r = |\mathbf{H}(\nu < 0)|/|\mathbf{H}(\nu > 0)|$. The modeled or observed transfer function is indicated by the title above each the plots. The abscissa in each plot is the absolute frequency $|\nu|$ from 0.025 to 1.975 cpd. By definition the ratio r is 1 at the zero frequency.

such, the ratio r predicts the polarization of the ocean response as a function of absolute frequency $|\nu|$. The polarization is by definition 1 at zero frequency.

Fig. 4.6 shows r for each model (the display of this figure mirrors the display of Fig. 4.1), as a function of latitude and as a function of absolute frequency $|\nu|$. The value of r was computed using the optimum parameters of each model, obtained for each latitudinal band (see section 4.5). In this figure, the lower right panel shows r for the observed transfer functions at 15 m. The polarization of the observed transfer function is noisy due to the random errors of the spectral estimation. The colorscale for r spans values between 0 and 1 because all the theoretical models predict r to be less than or equal to unity. In fact, r from the observed transfer functions is almost always less than 1 except in a few frequency bands, at low frequencies at high latitudes and at some supra-inertial bands where the spectral estimates are the most noisy.

Most of the models replicate the dominant characteristic of the observed polarization, which is a dramatically greater anticyclonic response at $|\nu| = |f|/2\pi$. This response is illustrated by the band of low values for r that follows closely the local inertial absolute frequency as a function of latitude from 1 cpd at 30°S to 1.73 cpd at 60°S. A typical example is model (1a) (top-left panel of Fig. 4.6), for which r decreases from 1 at $|\nu| = 0$ to 0 as $|\nu| \rightarrow |f|/2\pi$, and increases again for supra-inertial frequencies. For this model, r formally goes to zero because the transfer function in the anticyclonic domain ($\nu > 0$) presents a singularity at the inertial frequency. Fig. 4.6 shows r for $z = 15$ m, but for model (1a), it can be shown that it varies with depth and from the theoretical expression $\mathbf{H}_{1a}$, it can be inferred that r it is maximum at the surface and decreases with depth. It is also a decreasing function of K_0, except at the surface. As an example, at 53°S with $K_0 = 1.3$ m^2 s^{-1}, the response to a diurnally rotating cyclonic wind stress ($\nu = -1$ cpd) is theoretically r =0.45 times less than for a diurnally rotating cyclonic wind stress ($\nu = 1$ cpd) of the same magnitude. However, the observed transfer function indicates a greater ratio of 0.73, meaning that model (1a) overestimates the anticyclonic relative response. This discrepancy is due to the fact that, first the observed transfer function is finite because it is computed from real data and does not show a singularity as $|\nu| \to |f|/2\pi$, and second it is also likely due to the fact that model (1a) is the model that performs the most poorly to explain the observed transfer function in general, as will be seen in the next section.

In contrast, it will be seen that the two best models to explain the observed transfer function, models (1b) and (2b), do not strongly overestimate the anticyclonic relative response at $|\nu| = 1$ cpd since they both predict $r = 0.69$ at 53°S, in closer agreement with 0.73 for the observations.

4.5 Viscosity estimates and discussion

Using the results of the optimization, this section discusses which of the models are best able to explain the Southern Ocean drifter observations. The dynamical links between the latitudinal and seasonal variations of the parameter estimates and the environmental conditions are also explored.

4.5.1 The vertical structure of the Ekman layer

Numerous studies have compared observed oceanic velocities and theoretical predictions from Ekman models, and they have led to a range of different parameterizations and actual numerical values for K. An extensive review of earlier studies was done by Huang (1979). More recent studies are reviewed by Santiago-Mandujano and Firing (1990). The magnitude and direction of the predicted Ekman transports from wind data ($|\boldsymbol{\tau}|/\rho f$) are generally in very good agreement with observations, whether estimated from shipboard Acoustic Doppler Current Profiler observations along an oceanic transect (e.g. Chereskin and Roemmich, 1991; Wijffels et al., 1994), or from localized moorings observations on the time mean (e.g. Price et al., 1987; Schudlich and Price, 1998) or even on daily time scales (e.g. Chereskin, 1995). On the other hand, theoretical predictions for the detailed vertical structure of the wind-driven velocities have not been as satisfactory in the sense that no unifying model seems to be applicable for both the magnitude and the rotation of the velocity. In general, an Ekman-type spiral is observed, but it appears more “flat” than the theoretical one that is derived from the “classic” steady model with a constant K and an infinite ocean, which is model (1a) at zero frequency according to the nomenclature in this work. This means that the velocity magnitude decays with depth more rapidly than the velocity vector rotates away from the wind stress direction (Schudlich and Price, 1998; Price and Sundermeyer, 1999). In other words, the shear near the surface is predominantly downwind. Here, we argue that model (3b) is better at representing a predominant downwind shear close to the surface than is the classic model. Fitting model (1a) to observations for either the speed decay or the velocity rotation with depth leads to values for K which are inconsistent and which differ by one order of magnitude. As examples, in an analysis of observations of vertical shear off the coast of California, Weller (1981) gave the qualitative estimates for the constant vertical viscosity of 50×10^{-4} m^2 s^{-1} from the amplitude decay and of 500×10^{-4} m^2 s^{-1} from the rotation. Using velocity observations from the LOTUS3 mooring site in the Sargasso Sea, Price et al. (1987) estimated the vertical viscosity to be 60×10^{-4} m^2 s^{-1} from the amplitude decay but 540×10^{-4} m^2 s^{-1} from the rotation. Chereskin (1995) estimated these values as 274×10^{-4} and 1011×10^{-4} m^2 s^{-1} from the Eastern Boundary Current (EBC) mooring observations off the coast of Northern California. From shipboard ADCP data in the Drake Passage, Lenn (2006) estimated these values as 220×10^{-4} m^2 s^{-1} and 1390×10^{-4} m^2 s^{-1}.

The theoretical study of the transfer functions of the different models presented in section 4.3 indicates that the vertical structure of wind-driven currents depends on the frequency of the forcing. As such, it can be expected that observations of near-surface wind-driven ocean velocity as a function of time will be representative of the superposition of various spectral components. The frequency spectrum of the wind forcing has been shown in the Southern Ocean to exhibit a red character. As a consequence, the structure of the Ekman layer should resemble what is predicted by the transfer functions at low frequencies. However, the wind stress can also exhibit spectral peaks at high frequencies, notably at the inertial frequency (Stockwell et al., 2004).

Most models presented before predicted a resonance or a stronger response at the inertial frequency so that at least for several inertial periods, the inertial response is going to dominate the wind-driven velocities (Crawford and Large, 1996). The point is that the response in general and the vertical structure of wind-coherent currents in particular will differ according to the time scales of the forcing. Also, the ability to observe these different responses will depend on the filtering of the observation. This point was made clearly by Weller and Plueddemann (1996) who observed that the oceanic boundary layer behaved more like a slab near the inertial frequency but was sheared vertically at sub-inertial frequencies.

4.5.2 What is the best model?

Figure 4.7 shows the results for each 2° latitudinal band of the optimization for all the models presented in section 4.3. The results for models (1-a,b,c) are plotted with blue symbols, the results for models (2-a,b,c) with red symbols, the results for model (3-a,b,c) with green symbols and finally the results for the cubic profile (model (kpp)) are plotted with black symbols. Panel a shows the K_0 coefficients on a logarithmic scale, panel b shows the K_1 coefficients on a linear scale, and panel c shows the boundary layer depths h on a logarithmic scale. For the cost function L, defined in Eq. (4.8), the values plotted in Fig. 4.7d correspond to the mean value of the cost function over the selected optimum set of parameters from the bootstrap distributions (see Appendix A.3). We assess which of the models is the best model according to the values of the cost function L, taking into account its uncertainty $\delta[\mathsf{L}]$, which is defined in Appendix A.2. This analysis covers a large range of latitudes, as well as global longitudes, and it encompasses various regimes of oceanic circulation like boundary currents, jets or convergence zones. As a consequence, the uncertainties of the results could arise both from random errors inherent to the data processing and also from the different physical regimes captured by the drifter dataset.

It is not straightforward to conclude that one model performs better in all lat-

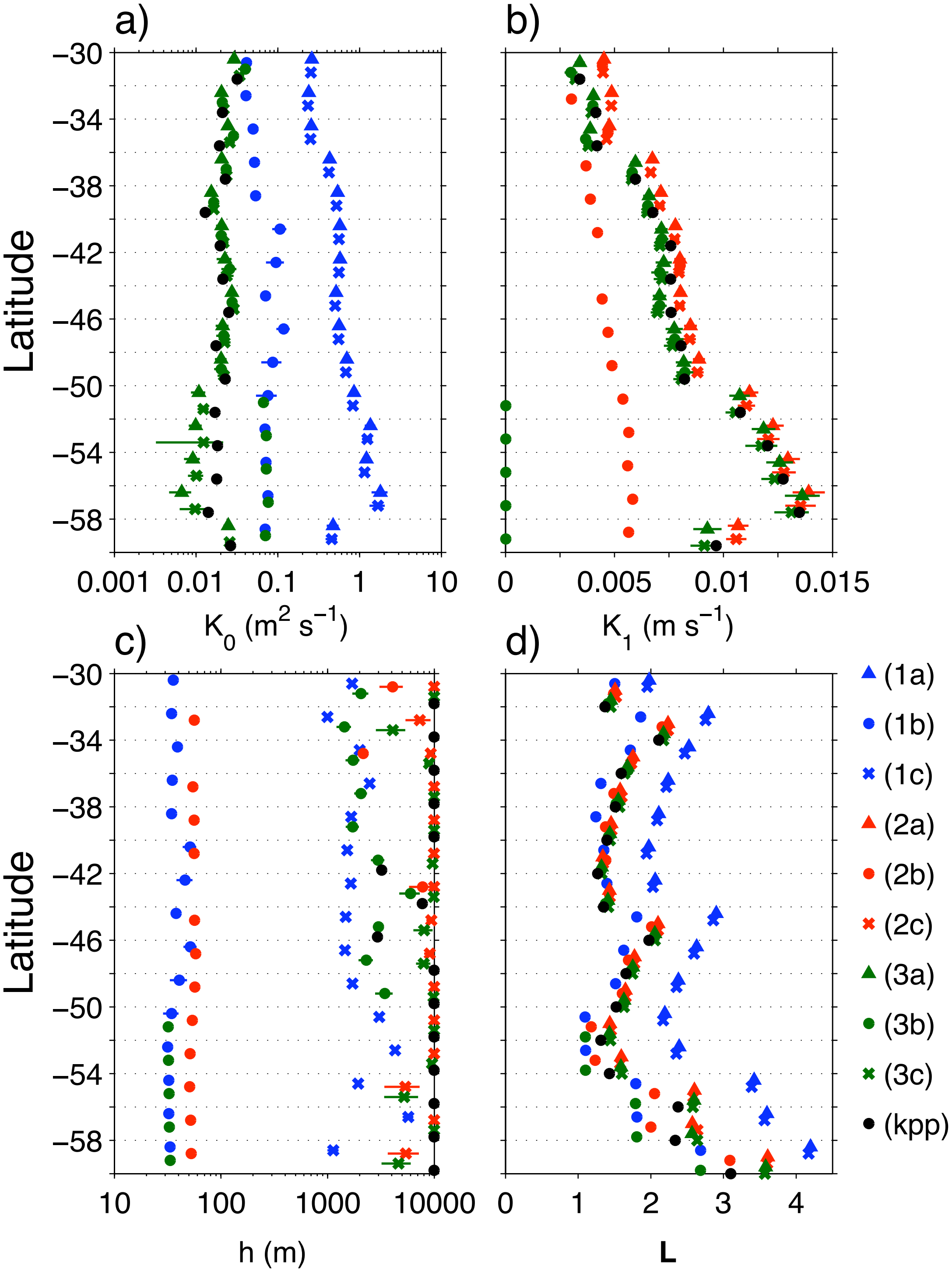

Figure 4.7: Optimum parameters and cost function for all models in 2° latitudinal bands. For model (3b) and for latitudes between 59°S and 51°S, the optimum values of K_1 are not significantly different from 0. Each data point is for data in a single 2° latitudinal band, but each model is offset from the others to improve legibility.

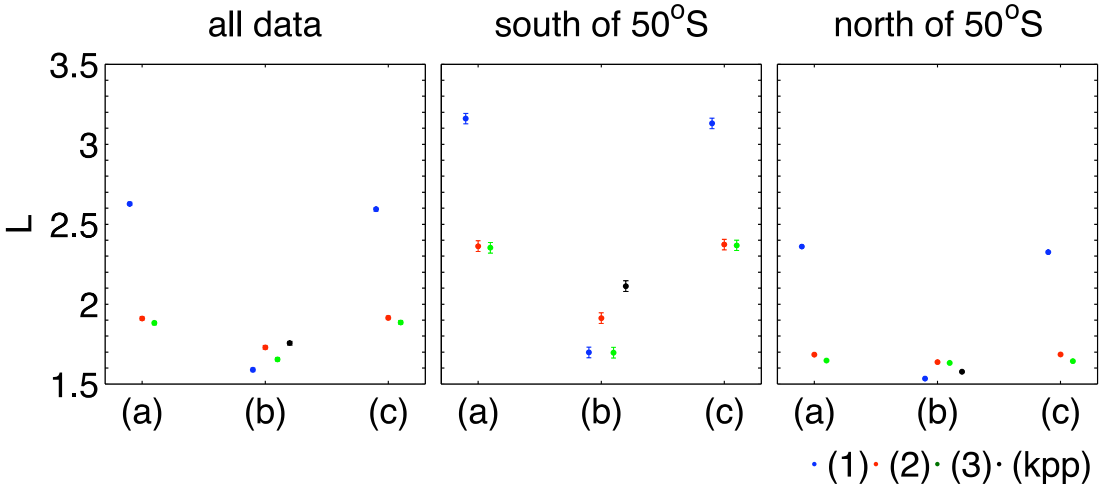

Figure 4.8: Average cost function values for all data (left panel), data south of 50°S (middle panel) and data to the north of 50°S (right panel). Error bars are plus or minus the latitudinally averaged standard error for the cost function as derived in appendix A.

itudinal bands according to the results presented in Fig. 4.7d. However, by computing an average of L over the data between 30°S and 60°S (left panel of Fig. 4.8), the models with a finite layer at the base of which the velocity goes to zero (models (1,2,3-b) perform significantly better than their counterparts with the same parameterization for K but with a different bottom boundary conditions. In contrast, several other models fail in the sense that the optimum parameters are found on the border of the parameter space explored by the optimization algorithms. For instance, even if models (2c) and (3c) return low values of L, they return values of h so large and unphysical that they are reduced to the associated infinite depth ocean models (2a) and (3a), respectively. Model (kpp) is also degenerate here since the optimum values of h are also physically too large. The cubic profile for the viscosity is consequently approximately reduced to a linear profile $K_0 + K_1 z$ near the surface and the optimum values for K_0 and K_1 are close to the optimum values returned for models (3a) and (3c). The results for these "failing" models are nevertheless reported in this work for completeness. In summary, for all data, disregarding the failing models (kpp), (2c) and (3c), the model performances are from best to worst: model (1b), model (3b), model (2b), model (3a), model (2a), model

(1a). It is important to point out here that model (1a), the model with a constant viscosity in an infinite depth homogeneous ocean, which is the model that many studies have compared with observations, is actually the worst model to explain the present observations of frequency-dependent Ekman currents in the Southern Ocean. Our attention is turned now to the two best models, and the vertical viscosity estimates they produce. It was seen in Chapter 3 that the wind energy input to the Ekman layer varied seasonally. Since the vertical viscosity and the boundary layer depth define the vertical structure of the Ekman layer energized by this wind energy input, their seasonal variations are also examined.

4.5.2.1 model (1b)

Fig. 4.9 again shows the results for all data for model (1b), and also for the data sorted by seasons. Across the Southern Ocean, model (1b) returns values for K_0 between 400×10^{-4} m^2 s^{-1} and 1180×10^{-4} m^2 s^{-1} (right panel of Fig. 4.9). The largest values, which also have the largest uncertainties, are found between 40°S and 50°S. The boundary layer depth h (left panel of Fig. 4.9) takes values between 30 and 50 m, with larger values in the same latitudinal band than where K_0 is the largest. In fact, h and K_0 are not independent. The boundary layer depth h, plotted in Fig. 4.9, is found to be within a few meters of $\delta_1(0)$, the exponential decay scale of this model at zero frequency, which is plotted in Fig. 4.13a. Through the definition of $\delta_1(0)$ (Eq. 4.17), this implies that

$$h \approx \sqrt{\frac{2K_0}{f}} = D_E/\pi. \tag{4.38}$$

This expression simply shows that, in this case, the depth of the boundary layer takes on the value of the Ekman depth divided by π. The relationship between K_0 and h was tested by regressing h against K_0, using all the estimates from the bootstrap samples (see Appendix A.1) in each latitudinal band. The results from the simple linear model $h = aK_0 + d$ are plotted in Fig. 4.10. In this figure, each panel displays for a given latitudinal band all the optimum parameter pairs, the overall mean and the regression

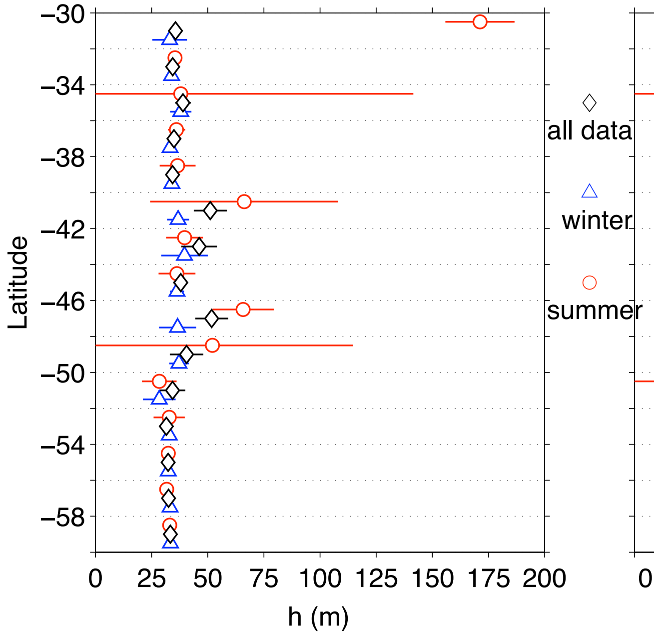

Figure 4.9: Seasonal variability of the boundary layer depth h and vertical viscosity K_0 for model (1b). The results for all data plotted in Fig. 4.7 are plotted once again for comparison. Error bars are the mean absolute difference from the optimum value.

curves for all the points. The slope and intercept of the regression curve are given in the lower right corner of each panel. In most of the latitudinal bands (except at 59°S, 55°S and 33°S), the results are well behaved and the intercept of the regression curve is close to 15 m. In some sense this is to be expected from the optimization algorithms which try to enforce the 15 m depth observations to be within the boundary layer. The regression coefficient of the fit is high, averaging 0.981 for the same bands, confirming the strong relationship between the depth of the boundary layer and the vertical viscosity. The linear coefficient a is found to decrease roughly with latitude, which implies that the Ekman layer reaches deeper at low latitudes. Given the numerical range of K_0 and h for model (1b), the correlation coefficient (0.976) of another model of the form $h = \alpha\sqrt{2K_0/f} + \beta$ and the simple correlation coefficient between h and K_0 (0.976) show that any of these three relationships between h and K_0 is equally valid.

For the data sorted by seasons, the results in Fig. 4.9 become more noisy at mid-latitudes and it is unclear that any seasonal variability is captured by the model.

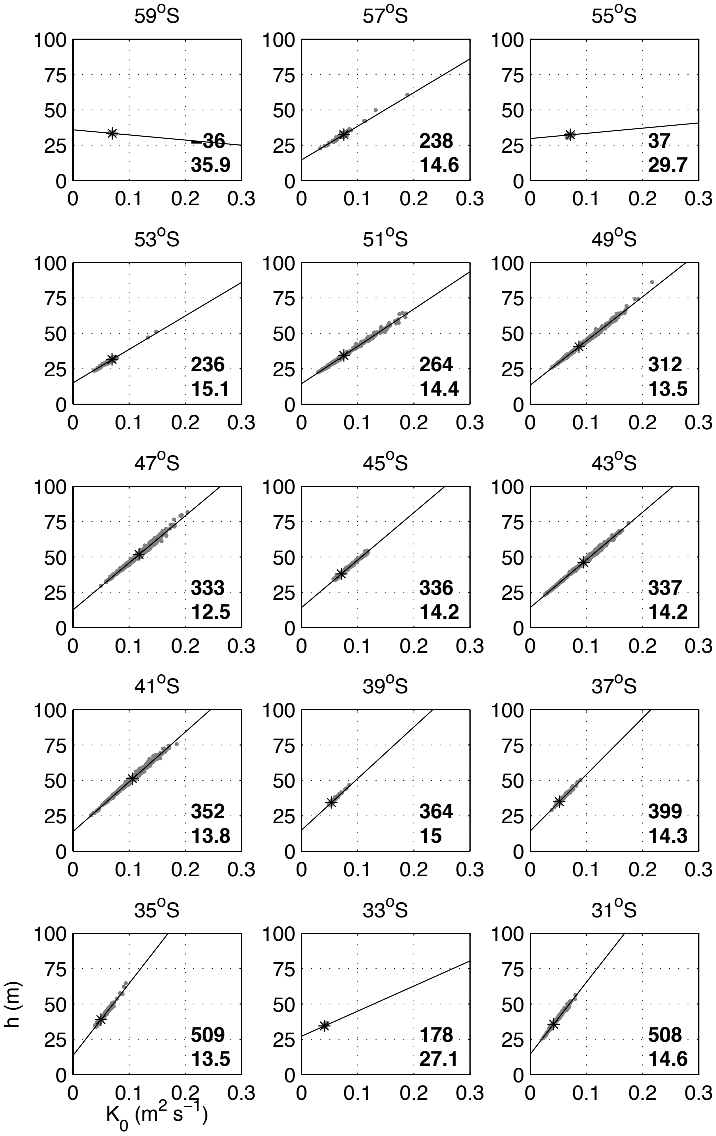

Figure 4.10: Optimum parameter pairs for model (1b) from all the bootstrap samples in each latitudinal band, plotted with gray dots. The labeling of the axes, h in m versus K_0 in m^2 s^{-1}, is indicated only for the lower left panel in order to improve the legibility of the figure. The center latitude of each 2° latitudinal band is indicated at the top of each panel. The overall optimum parameter pair is indicated by a black asterisk. For each panel, the regression curve $h = aK_0 + d$ is plotted and the corresponding rounded values of a and d are displayed in the lower right corner.

The error bars become large to the point that some values of h appear indistinguishable from 0. This is not the case. In fact, this occurs because the probability density functions of the bootstrap estimates can present several modes. For these plots (as well as for Fig. 4.11), the mean values of the distributions are plotted, and the error bars are the mean absolute differences from these mean values. As, these error bars should be interpreted as a range of excursion for the parameter considered, rather than the standard deviation of a Gaussian statistical distribution. The much larger value of h at 171 m in summer at 31°S is an extreme case of this situation. In any case, for model (1b), the cost function is larger for the summer data than for the winter data (not shown), which makes this result less reliable. Only south of 52°S and in a few latitudinal bands north of 40°S does the seasonal signal exist statistically with an increase of K_0 from summer to winter of about 24%. In contrast, at the same latitude, h does not vary with seasons.

4.5.2.2 model (3b)

The results for the second best model, model (3b), and its seasonal variations are shown in Fig. 4.11. The error bars in this figure are large, for the same reasons as for the results plotted in Fig 4.9. As mentioned previously, this model degenerates to model (1b) south of 50°S, since it returns values for K_1 which are not distinguishable from zero, and this is unchanged when the data are sorted by seasons. As such, the optimum values for h and K_0 are quasi identical to the values returned by model (1b). North of 50°S, the estimates of K_0 vary little with latitude, and are smaller, averaging to $(240 \pm 12) \times 10^{-4}$ m^2 s^{-1}. In contrast, h which is plotted in the top left panel of Fig. 4.11 on a logarithmic scale, varies greatly with latitude. Note that because of the logarithmic scale, the lower error bars may not be plotted for h. For all data north of 50°S, h is greater than 1000 m, actually ranging between about 1400 m and 6000 m. It is smaller in summer compared to winter, and does show some latitudinal dependence, which is more pronounced in summer. In summer, h changes order of magnitude from north to south, increasing roughly from 350 m at 31° S to 1925 m at 49° S. In winter, h

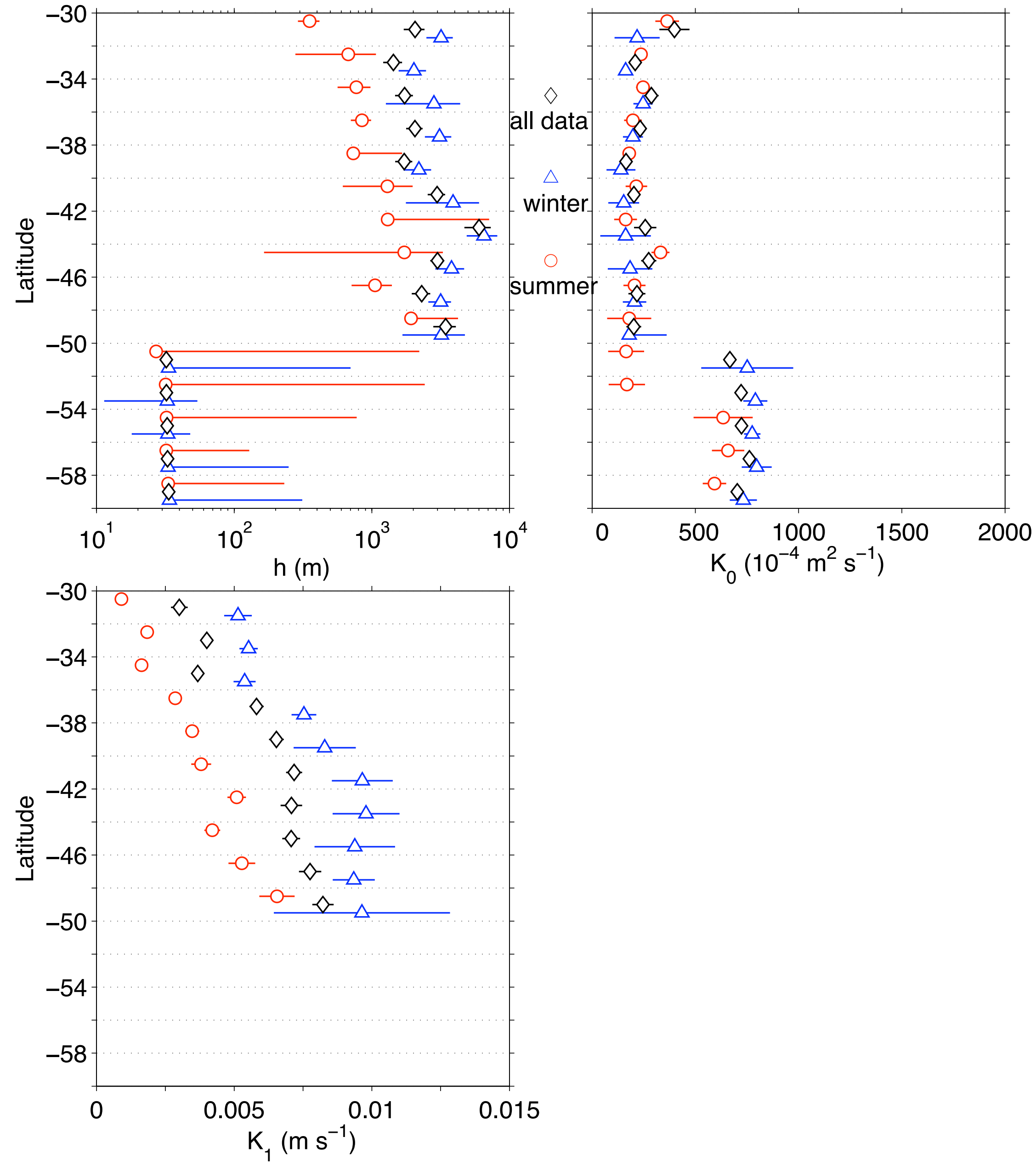

Figure 4.11: Boundary layer depth h and vertical viscosity coefficients for model (3b). The results for all data plotted in Fig. 4.7 are plotted once again for comparison. Error bars are the mean absolute difference from the optimum value.

varies between about 2000 m and 6500 m, without clear latitudinal dependence.

The values for K_1 (lower left panel of Fig. 4.11) to the north of 50°S range between 0.3 and 0.9 cm s^{-1} for all data. Two undeniable trends are noted for K_1. It increases towards the south by a factor of 2.5 for all the data. From summer to winter, K_1 increases by a factor 1.5 to the south and by 5.5 to the north. As discussed in the next section, the parameter K_1 is a friction velocity scale related to the wind stress.

North of 50°S, the parameters K_0 and K_1 are found not to be independent. The results from a regression to a simple linear model $K_0 = lK_1 + K_{00}$ are plotted in Fig. 4.12. In this figure, all the optimum parameter pairs (K_1, K_0) from the bootstrap samples for the latitudinal bands north of 50°S are plotted, along with the linear fits. In each panel, the rounded slope l in meters and the intercept K_{00} in cm^2 s^{-1} are written in black in the lower left corner. The regression coefficient of the fit is almost constant as a function of latitude and averages to 0.82. If the models were consistent with each other, especially the best models with the bottom boundary condition (b), one could expect that in the limit $K_1 \to 0$, the intercept would equal the constant vertical viscosity value found for model (1b). For reference, constant vertical viscosity from model (1b) is also written in each panel in blue. However, taking into consideration the error bars of K_0, the correspondence between K_0 from model (1b) and K_{00} can be verified only in a few latitudinal bands.

4.5.3 Relationships to external parameters

4.5.3.1 The relationship with the wind

The only explicit forcing mechanism considered in the Ekman models considered in this work is the action of the wind stress at the ocean surface. As such, one may expect the estimates of the viscosity and the boundary layer depth to have a relationship with the wind stress variability. For a stable or neutral planetary boundary layer, the relevant planetary scale is u_*/f where $u_* = \sqrt{|\boldsymbol{\tau}|/\rho}$ is the friction velocity. The value of u_* is plotted in panel b and u_*/f in panel a of Fig. 4.13, for all data and for data sorted

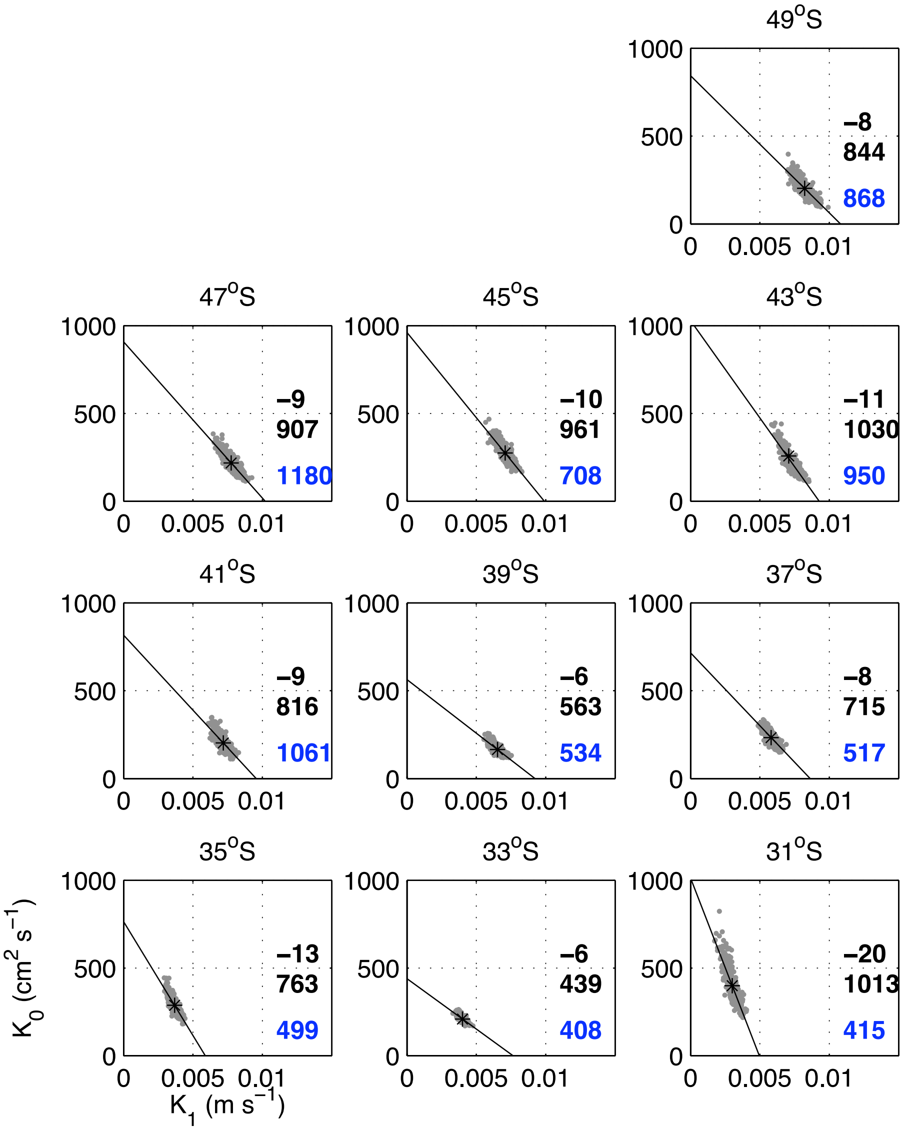

Figure 4.12: Optimum parameter pairs for model (3b) from all the bootstrap samples in latitudinal bands north of 50°S, plotted with gray dots. The labeling of the axes, K_0 in cm^2 s^{-1} versus K_1 in m s^{-1}, is indicated only for the lower left panel in order to improve the legibility of the figure. The center latitude of each 2° latitudinal band is indicated at the top of each panel. The overall optimum parameter pair is indicated by a black asterisk. For each panel, the regression curve $K_0 = lK_1 + K_{00}$ is plotted and the corresponding values of l in meters and K_{00} in cm^2 s^{-1}are displayed in the lower right corner. The value in blue font is the optimum value of the constant vertical viscosity for model (1b) in cm^2 s^{-1}in the corresponding latitudinal band.

by season, in each latitudinal band. Since these scales are evaluated by computing the mean of the wind stress values interpolated in space and time at the drifter locations, they reflect the same wind variability. The most noticeable feature in both these scales is the fact that the seasonal variability disappears south of 48°S. This is also the case for the viscosity scale u_*^2/f (not shown).

While model (1b) is overall the best model for explaining the observed transfer functions, its optimum parameters h and K_0 do not show much of the latitudinal and seasonal variability that appears in the wind stress and the scales derived from it. As such, the information that model (1b) provides on the the Ekman layer dynamics of the Southern Ocean is unclear. Also, attempts to relate h or K_0, which in fact are not independent for this model, to the mixed layer depth from climatological data were not successful. Despite providing dynamical insights, the optimum h and K_0 are within expected range of values. As a reference, the latitudinally averaged ratio of h to u_*/f for model (1b) is found to be 0.32 for all data, 0.27 in winter and 0.45 in summer, which is to be compared to the range 0.25-0.4 from numerical simulation of neutral turbulent Ekman layer by Coleman et al. (1990). Also for model (1b), the ratio of K_0 to u_*^2/f is 0.05 on average for all data, 0.04 in winter and 0.05 in summer, which is to be compared to the range 0.03-0.08 found in the same numerical study.

Our attention is now turned to some further characteristics of model (3b), the second best model. As was seen in chapter 3, the variability of the wind energy input rate to the Ekman layer is very much related to the characteristics of the wind stress. Here, for model (3b), the linear coefficient K_1, which has the units of a velocity, seems to show a relationship to the wind stress. The optimum values of K_1 for model (3b) as a function of latitude and season are plotted along with the value of u_* in Fig. 4.13b. For models with linear viscosity, the linear coefficient is usually written $K_1 = \kappa u_*$ (Thomas, 1975; Madsen, 1977). Madsen (1977) took $\kappa = 0.4$ but it seems that this value in the ocean or the atmosphere is variable (Tennekes, 1973). From the data points in Fig. 4.13b, for all data, $K_1/u_* = 0.52$, and this ratio is 0.64 in winter and 0.33 in summer. In both seasons, this ratio actually increases with latitude. This suggests that while K_1 scales like u_*, a universal and constant value of 0.4 does not seem to be adequate.

4.5.3.2 The influence of the stratification

Fig. 4.11a shows h for model (3b) which indicates that deeper boundary layers are found at lower latitudes and in winter. Large et al. (1997) diagnosed monthly averages of mixed layer depths (MLD) and boundary layer depths (BLD) established by the KPP scheme in a run of a GCM. In the Southern Ocean, in the austral winter, they found that these two depths were comparable, and only to the south of 60°S did the model show deeper values, of O(1000 m) with the range of instantaneous values (that is values diagnosed within a single model time step) extending much deeper for h, down to 2000 m. In the North Atlantic, in boreal winter, the BDL even reached the bottom of the model. These deep boundary layers however occurred at known locations of deep convections where buoyancy fluxes de-stabilize the water column and trigger free convection. The models considered here assume a forced convection mechanism fed by the the wind energy input at the surface and as such, do not consider any flux of buoyancy, nor any stratification explicitly.

Nevertheless, one may hypothesize that buoyancy fluxes implicitly condition the results returned by these Ekman models via the setting of stratification. In particular, a strong density gradient like what is found in the oceanic thermocline could inhibit the penetration of the wind momentum so that the stratification could be linked to the various depth scales of the models. From observational data, the MLD is usually defined by a temperature or density difference criteria from the surface so that the mixed layer can really be more accurately an isothermal layer. Since temperature, buoyancy or momentum do not “diffuse” down, or mix, at the same rate, the MLD and BLD h should not be expected to be equal. As an example, some substantial shear can be observed within an isothermal layer (e.g. Davis et al., 1981). The mean MLD interpolated in space on the drifter positions, as well as in time according to the month of the year, is plotted in Fig. 4.13a, as a function of latitude and season. The MLD data used here is from Dong et al. (2006), who based their climatology for the Southern Ocean on vertical density profiles from ARGO float data. This climatological depth is based on a density criterion of a 0.03 kg m^{-3} difference from the 0-20 m surface value. Despite the fact that the MLD at the location of the drifters exhibits latitudinal and seasonal trends common with h found for model (3b) (top left panel of Fig. 4.11), these two are of different orders of magnitude, h being O(1000 m) and the MLD O(100 m).

The BLD is not the only depth scale entering the mathematical expression of the transfer function for model (1b) or (3b). The depth scale δ_1 at zero frequency computed from the optimum values of K_0 for model (3b) is plotted with open symbols as a function of latitude in Fig. 4.13a. This scale actually does not appear naturally in the mathematical expression of the transfer function $\mathbf{H}_{3b}$, and neither its value nor latitudinal variations seem to have a relationship with the wind stress forcing or the MLD. In contrast, the depth scale δ_2 at zero frequency, plotted with filled symbols in Fig. 4.13a, seems to correspond to the MLD. This correspondence is not only found for all data but also for seasonally sorted data. Whereas $\delta_1(0)$ for models (1-a,b,c) is a familiar scale of exponential decay, $\delta_2(0)$ appears in a complicated manner in the expression of the transfer function for model (3b). We computed the ratio of the absolute value of the transfer function at the depth $z = \delta_2(0)$ to the surface value, evaluated using the optimum parameters. This is also the ratio of the velocity magnitudes at the same depths. At the depth $z = \delta_2(0)$, the current speed is about 15% of its surface value at 50°S, a percentage which increases almost monotonically to about 32% at 31°S. Overall, this suggests that according to model (3b), the wind-driven velocities penetrate deeper than the depth of the mixed layer. At 31°S, model (3b) indicates that the current speed is 10% of its surface value at about 120 m depth, and this 90% decay level deepens to 145 m at 49°S.

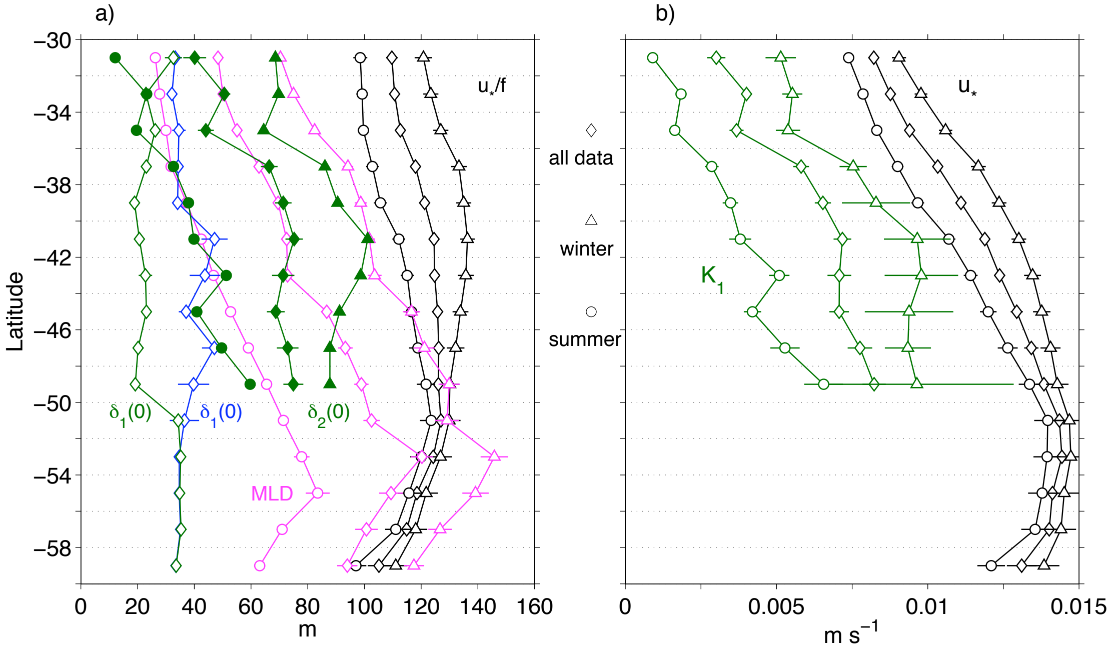

Figure 4.13: a) Green curves are for model (3b), open symbols are $\delta_1(0)$ and filled symbols are $\delta_2(0)$. The blue curve is $\delta_1(0)$ for model (1b). The planetary scale, u_*/f, is computed from the mean of the wind stress interpolated on the drifter positions (see text). The magenta curves are the MLD from Dong et al. (2006). b) K_1 for model (3b) and friction velocity u_*. Symbols for seasons are: $\diamond$ all data, $\triangle$ winter data, $\circ$ summer data. The error bars for MLD, u_* and u_*/f are the standard error of the mean. The error bars for $\delta_1(0)$ and $\delta_2(0)$ are obtained by formally propagating the errors from K_0 and K_1.

4.5.3.3 The sea surface roughness

The ocean-atmosphere interface is a moving boundary, separating the atmospheric boundary layer from the oceanic boundary layer. These two layers interact with each other, notably by creating roughness along the interface. As an example, for the atmosphere, the oceanic surface gravity waves constitute the roughness element, and their amplitude will provide the scaling for the air-side roughness length z_0 (e.g. Melville, 1977). For the ocean, the waves seem to be also an important conditioning factor, and z_0 is expected to be representative of the thickness of an unresolved, wave-enhanced sublayer (Craig and Banner, 1994), just below the surface. Possible scalings for z_0 found in the literature include the significant wave height (e.g. Terray et al., 1996), some multiple of u_*^2/g where g is the gravitational acceleration, or the wavelength of the waves (Craig and Banner, 1994).

The roughness length is an important parameter in boundary layer theory and it needs to be considered in order to model correctly the vertical velocity profile as one approaches the boundary. This is illustrated in the present case: whereas it was found that models (2-a,b,c) have kinematic features that can explain the frequency-dependent vertical structure of the Ekman layer, they presented a deceptive singularity at the surface. Resolving this has led to the development of models (3-a,b,c) by introducing the roughness length z_0, or equivalently assuming that a finite value of the viscosity $K_0 = z_0 \times K_1$ existed at the surface.

For models (3-a,b,c), the optimization procedure was set up to conduct a search of the two parameters K_0 and K_1, which are assumed a priori to be independent. They were found however to covary. The estimates of $z_0 = K_0/K_1$, computed from the estimates of K_0 and K_1 for models (3-a,b,c) and model (kpp), are plotted in Fig. 4.14. It was shown previously that for model (3b), the parameters K_0 and K_1 are not independent and that their relationship could be well modeled by $K_0 = K_{00} - K_1 l$, according to a regression applied on the estimates from the bootstrap samples. The same type of relationship actually holds for models (3a) and (3c) (not shown). In fact,

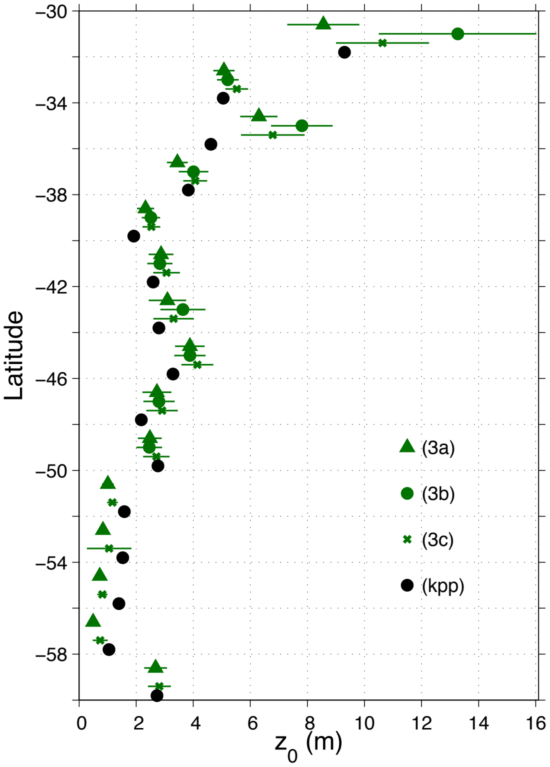

Figure 4.14: Sea surface roughness estimates $z_0 = K_0/K_1$ in 2° latitudinal bands for models (3-a,b,c) and model (kpp). Error bars are derived from the error bars for K_0 and K_1. Note that no estimates can be obtained for model (3b) south of 50°S since it is found that $K_1 \approx 0$.

the length scale l here does not correspond exactly to z_0 and is actually up to 3 times larger. However, their latitudinal variations roughly coincide, as well as their seasonal variations (not shown). Interestingly, the roughness parameter is larger in the austral summer than it is in the austral winter, which is mostly a consequence of the seasonal variations of K_1. An examination of Fig. 4.14 does not suggest a relationship to the environmental variables considered so far like the MLD, the wind stress magnitude, or the Coriolis parameter. It would be of great interest to relate these estimates to a climatology of surface wave parameters in the Southern Ocean in order to see if observed wave dependence could be detected with the drifter dataset.

4.6 Summary: a zonal view of the Ekman layer

The study of the transfer function from the wind stress to the ocean velocity at 15 m depth, derived from drifter trajectories, helps to elucidate the structure of the Ekman layer in the Southern Ocean, from 30°S to 60°S. The analysis consisted in first estimating which of 10 vertical viscosity parameterizations are the best at explaining the observed transfer functions, computed in 2° latitudinal bands. The second part of the work presented in this chapter was to analyze the vertical viscosities and boundary layer depths which were diagnosed from the Ekman layer models.

Fig. 4.15 shows the vertical structure of the Ekman layer, in two latitudinal bands centered at 41°S and 53°S, in terms of the vertical profiles of viscosity and velocities. The vertical profiles of velocities are shown for models (1b), (2b) and (3b) and were computed by multiplying the modeled transfer function by 0.1 N m^{-2}. As such, it is a representation of what the Ekman layer structure would be if the forcing consisted in a monochromatic wind stress of magnitude 0.1 N m^{-2}, (about 9 m s^{-1}10-m wind speed). Three frequency bands are represented, for ν = 0, 5 and -5 cpd. The 15 m observed transfer function in each of these frequency bands, multiplied by 0.1 N m^{-2} is also plotted. The ± 0.5 cpd frequencies are chosen here because it is at these frequencies that the coherence squared presented in Chapter 2 is approximately the highest. As

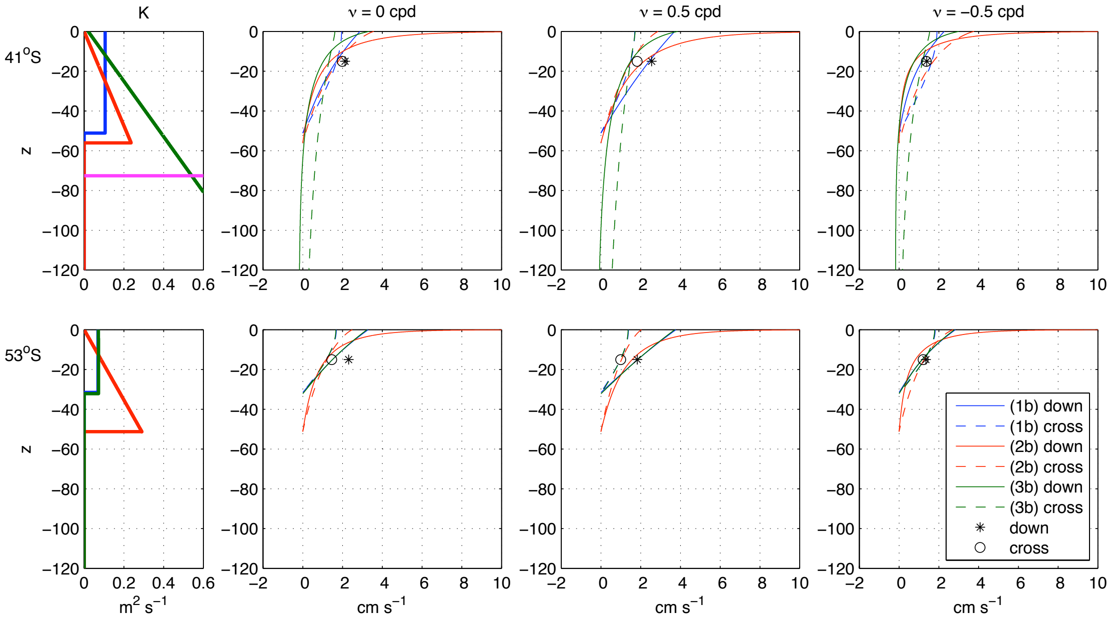

Figure 4.15: Zonally averaged vertical profiles of modeled viscosity and Ekman velocity at 41°S (upper row) and 53°S (lower row) The first column is the vertical viscosity profile $K(z)$. For the results at 41°S the depth of the mixed layer is indicated by a horizontal magenta line. The second column is the mean ($\nu = 0$) velocity profiles from model (1b) in blue, from model (2b) in red and from model (3b) in green, for the downwind components (solid lines) and the crosswind components (dashed lines). The third and fourth columns are the velocity profiles at $\nu = 0.5$ cpd and $\nu = -0.5$ cpd, respectively, with the colors referring to the same models than in the second column. In each of the velocity plots, the observed 15 m transfer function at the corresponding frequency times 0.1 N m^2 is plotted with an asterisk for the real part (downwind component) and with a circle for the imaginary part (crosswind component).

such, they are the anticyclonic and cyclonic frequency bands for which the observed oceanic response to the wind stress forcing is the strongest. The coherence is also the frequency-dependent weight function for the optimization. A consequence is that, as seen in Fig. 4.15, the models better match the observed transfer function at 0.5 and -0.5 cpd than they do for the mean. Model (2b) has not been discussed in this work but is plotted nevertheless as a reference.

Overall, the results of the optimization indicate the following zonal view of the Ekman layer in the Southern Ocean, from south to north. From 60°S to 50°S, the Ekman layer is shallow, of O(30-45) m. In this layer, the viscosity is approximately constant, averaging at 724×10^{-4} m^2 s^{-1} and shows small seasonal variations of the order of $\pm$ 15%. In the upper part of this layer, for the mean, the shear is predominantly downwind and this character is accentuated as the frequency of the motion increases towards the inertial frequency. This is illustrated at 53°S in Fig. 4.15 by noticing that the downwind component is even larger than the crosswind component at 0.5 cpd than it is 0 cpd. Also, the downwind shear is approximately constant while the cross-wind shear increases with depth. These latitudes correspond to the largest wind stress values with little seasonal variations.

At mid-latitudes, the Ekman layer is best described by slightly deeper layer, with associated increased constant vertical viscosity reaching over 1000 m^2 s^{-1}, however with very little seasonal variability. The vertical shear is not as strong as at higher latitudes but the downwind shear still dominates over the crosswind shear in the upper half of the layer.

An alternate and more dynamically consistent description of the Ekman layer to the north of 50°S is the one given by model (3b), the second best model, to explain the drifter observations in the Southern Ocean. For this description, the vertical viscosity in the Ekman layer is not constant but increases gradually with depth. A typical example is given at 41°S (upper row of Fig. 4.15) where K increases from 200×10^{-4} m^2 s^{-1} at the surface to approximately 5300×10^{-4} m^2 s^{-1} at the climatological depth of the mixed-layer. At this depth, the wind-driven velocity is reduced by about 85% from its surface value. The Ekman layer is actually much deeper than the mixed layer, maybe up to 3000 m, but the velocity decreases rapidly, and is 1% of its surface value around 600 m. The Ekman layer is much influenced by the seasonal cycle in the wind stress, causing the boundary layer to be deeper in winter, and the linear increase with depth of the viscosity to be greater, associated with stronger mean wind stress.

Appendix A

Optimization and error analysis

A.1 Bootstrapping

We implemented a bootstrap method (Efron and Gong, 1983) in order to infer the sample variance of the transfer function estimates and to assign uncertainties to our optimum parameters.

For each latitudinal band, the N segments (listed in Table 2.1) were randomly re-sampled to obtain a bootstrap sample containing N segments but allowing for repetition. A total of $M = 500$ bootstrap samples were drawn in this way and subsequently M estimates $\widehat{\mathbf{H}}_k$, $k = 1 \ldots M$, of the transfer function were computed by the peridogram method.

A.2 Error estimates for the transfer function

Estimates of the transfer function have random errors inherent to the spectral estimation. Bendat and Piersol (1986) provide approximate formulae for the variances and normalized random errors of the magnitude and phase of the transfer function. However, since we generated bootstrap samples, we can obtained unbiased estimates of the sample variance:

$$\mathrm{Var}[|\widehat{\mathbf{H}}|] = \frac{1}{M-1}\sum_{k=1}^{k=M}(\mathbf{H}_k - \overline{\mathbf{H}}_k)(\mathbf{H}_k - \overline{\mathbf{H}}_k)^*,$$

where $\overline{(\cdot)} = \frac{1}{M}\sum_{k=1}^{k=M}(\cdot)_k$ is the sample mean estimate. This variance estimate is then used to compute the standard error of the mean for the magnitude of the transfer function as a function of frequency:

$$\delta\left[|\widehat{\mathbf{H}}(\nu)|\right] = \sqrt{\frac{\mathrm{Var}[|\widehat{\mathbf{H}}(\nu)|]}{N_{\text{eff}}}},$$

where N_{eff} is the effective number of degrees of freedom (DOF). N_{eff} in each latitudinal band is less than the number of segments N listed in Table 2.1 because of the 50% overlap and the Hanning windowing of the time series segments, and is theoretically asymptotically reduced by 25% as $N \to +\infty$ (Harris, 1978). This approximation is expected to work well here, because the smallest number of segments used to compute spectral estimates (at 59°S in the summer) is still greater than 50.

A.3 Algorithms for the optimization procedure and uncertainties for the optimum parameters

We selected parameter limits for the optimization procedure for each specific model. These ones are listed in Table A.1. For h, the lower bound was taken as the physical limit of 0 m for an oceanic boundary layer whereas it was taken as 15 m for the KPP model because we needed to have the depth of the drogue to be within the layer over which the numerical integration was performed. For the upper bound, we chose the limit 10^4 m to be consistent with an expected order of magnitude of 10^3 m for a wind-driven layer. For K_0 and K_1 we limited ourselves to the $[0, 3]$ m s^{-1}or m^2 s^{-1}intervals. Because the parameter space to explore was large and sometimes several local minima for L existed, we implemented different optimization algorithms depending on the model. In some cases, we used the multidimensional unconstrained nonlinear minimization or

Nelder-Mead simplex method (Nelder and Mead, 1965), coded in the `fminsearch` MATLAB function. In order to constrain this algorithm to the chosen parameter space, we added a prohibitory penalization to L whenever the algorithm wandered outside of the space limits. When several minima appeared, we used the Nelder-Mead algorithm augmented by a simulated annealing procedure step (Press et al., 1988), using the function `simannealingSB` from the Systems Biology Toolbox for MATLAB (Schmidt and Jirstrand, 2005). The parameters used for the simulated annealing algorithm are listed in the caption of Table A.1. For model (1b), the optimization algorithm was restarted from its first result set to ensure exhaustiveness in the space search.

The optimization procedure for each model was run for the estimate of the transfer function $\widehat{\mathbf{H}}$ computed from the N segments in each latitudinal band, and then run on each of the M $\widehat{\mathbf{H}}_k$ bootstrap samples. The distribution of the M optimum values for each parameter was used to assess the uncertainty in the estimates. In some cases listed in Table A.1 (see the "Results distribution" entry line), the joint probability density functions (pdf) showed several modes with approximately the same corresponding cost function value. For these cases, the most probable mode was isolated. Then, the uncertainties were derived from the distribution around these modes and we chose the error bars for any of optimum parameter x in Fig. 4.7 to be plus or minus the mean absolute value about the mean $\overline{x}$:

$$\text{error} = \frac{1}{M^*} \sum_{k=1}^{k=M^*} |x_k - \overline{x}| \,,$$

where $M^* \leq M$ is the actual number of optimum parameter values retained for the errors estimation. In most cases, the overall optimum parameters obtained from $\widehat{\mathbf{H}}$ were indistinguishable from the mean optimum parameters obtained from the bootstrap estimates $\widehat{\mathbf{H}}_k$. However, in a few cases, the overall optimum parameters obtained differed from the mean parameters obtained from the bootstrap estimates by more than twice the uncertainties. In these cases, the overall optimum parameters belonged to another less probable mode of the joint pdf. The results presented here are the mean of the retained optimum parameters obtained from the bootstrap samples.

Because of computational constraints, we did not apply this bootstrap method to the KPP model and only one optimization procedure was run with the transfer function estimated from the N segments in each latitudinal band.

A.4 On the influence of the variance of the spectral estimator on the optimization procedure termination

The Nelder-Mead algorithm is a direct search method commonly employed in non-linear optimization (Nelder and Mead, 1965) and well reviewed in the published literature (e.g. Press et al., 1988). However, since this algorithm searches for a minimum of the cost function L, it is legitimate to wonder how the variance of the transfer function estimate $\widehat{\mathbf{H}}$ is taken into account. From the expression (4.8), we roughly propagate the errors to obtain a standard error for the cost function L:

$$\delta\left[\mathsf{L}\right] = \sum_{\nu_k} \delta\left[|\widehat{\mathbf{H}}(\nu_k)|\right] \times \widehat{\gamma}^2(\nu_k), \tag{1.1}$$

where the summation is over the frequency range. $\delta\left[\mathsf{L}\right]$ was estimated across the Southern Ocean and we found it to be less than 2×10^{-2} for latitudes lower than 46°S and to increase monotonically polewards and to be maximum at 0.11 at 59°S. This last value should therefore be used as an upper bound value for the amount by which one can hope to reduce the cost function (the function tolerance) when proceeding to the next step in the optimization algorithm. The second criterion for the termination of the algorithm however is that the diameter of an n-dimension simplex (where n is the number of dimension of the search space) be less than a tolerance value (10^{-5}). We found that this was the controlling criteria in terminating the optimizations and that setting the tolerance function to 2×10^{-2} or less did not change our results significantly. In the end, we selected 10^{-2} as the function tolerance.

Table A.1: Characteristics of the cost function minimizations. K_n: vertical viscosity polynomial coefficients; h: boundary layer depth in m; NM: Nelder-Mead simplex method ; NMSA: Nelder-Mead simplex method plus Simulated Annealing with the following options: starting temperature 100°, termination temperature 0.1°, temperature step factor 0.1. The result distribution line refers to the number of modes found in the joint probability density functions of the optimum parameters, obtained from the bootstrapping procedure.

Model	(1a)	(1b)	(1c)
Parameters	K_0	K_0,h	K_0,h
Limit constraints	[0,3]	[0,3],[0,10^4]	[0,3],[0,10^4]
Initial guess	0.5	(0.1,50)	(0.01,1000)
Algorithm	NM	NMSA×2	NMSA
Results distribution[a]	1	1 (2 at 31°S)	2
Model	**(2a)**	**(2b)**	**(2c)**
Parameters	K_1	K_1, h	K_1, h
Limit constraints	[0,3]	[0,3],[0,10^4]	[0,3],[0,10^4]
Initial guess	0.001	(10^{-3},200)	(10^{-3},10^3)
Algorithm	NM	NMSA×2	NM×2
Results distribution	1	2	1
Model	**(3a)**	**(3b)**	**(3c)**
Parameters	K_0, K_1	K_0, K_1, h	K_0, K_1, h
Limit constraints	[0,3],[0,3]	[0,3],[0,3],[0,10^4]	[0,3],[0,3],[0,10^4]
Initial guess	(0.01,0.1)	(10^{-2},8×10^{-3},500)	(10^{-2},8×10^{-3},500)
Algorithm	NM	NM	NM
Results distribution	1	2	1
Model		**(kpp)**	
Parameters		K_0, K_1, h	
Limit constraints		[0,3],[0,3],[15,10^4]	
Initial guess		(10^{-2},8×10^{-3},50)	
Algorithm		NMSA	

[a] 1:unimodal 2:bimodal

Appendix B

Equality to Gonella's (1972) transfer function

The transfer function $\mathbf{H}_{1c}(z)$ from section 4.3 is defined between $z = 0$ and $z = -h$ (note the change of sign convention):

$$\mathbf{H}_{1c}(z) = \frac{1}{\rho K_0 \alpha} \frac{\cosh\left[\alpha(z+h)\right]}{\sinh\left[\alpha h\right]} \quad \text{with} \quad \alpha = \sqrt{i\left(\frac{2\pi\nu + f}{K_0}\right)}.$$

we seek a Fourier series that coincides with $\mathbf{H}_{1c}$ on the $[-h, 0]$ interval. For this purpose, it is imaged with respect to $z = 0$ and is now defined on the $[h, -h]$ such that $\mathbf{H}_{1c}(z) = \mathbf{H}_{1c}(-z)$. A Fourier series will then have the form:

$$\mathbf{H}_{1c}(z) = \sum_{n=-\infty}^{+\infty} c_n e^{in\frac{2\pi}{2h}z},$$

with

$$c_n = \frac{1}{2h}\int_{-h}^{h} \mathbf{H}_{1c}(z) e^{-in\frac{2\pi}{2h}z} dz.$$

Let's consider

$$g(z) = \cosh[\alpha(z+h)],$$

for which the d_n Fourier coefficients are easily computed:

$$d_n = \frac{\alpha \sinh(\alpha h)}{h}\left(\alpha^2 + \frac{n^2\pi^2}{h^2}\right)^{-1}$$

Now, noticing that

$$\mathbf{H}_{1c}(z) = \frac{1}{\rho K_0 \alpha} \frac{g(z)}{\sinh(\alpha h)},$$

one obtains:

$$c_n = \frac{1}{\rho K_0 h} \left(\alpha^2 + \frac{n^2 \pi^2}{h^2} \right)^{-1}.$$

A Fourier series representation of $\mathbf{H}_{1c}$ is then

$$\begin{aligned} \mathbf{H}_{1c}(z) &= \sum_{n=-\infty}^{+\infty} \frac{1}{\rho K_0 h} \left(\alpha^2 + \frac{n^2 \pi^2}{h^2} \right)^{-1} e^{in \frac{2\pi}{2h} z} \\ &= \frac{1}{\rho K_0 h \alpha^2} \sum_{n=-\infty}^{+\infty} \left(1 + \frac{n^2 \pi^2}{\alpha^2 h^2} \right)^{-1} e^{in \frac{2\pi}{2h} z}. \end{aligned}$$

Substituting for α, one obtains

$$\mathbf{H}_{1c}(z) = \frac{1}{i \rho h (2\pi\nu + f)} \sum_{n=-\infty}^{+\infty} \left[1 - i \frac{n^2 \pi^2}{h^2 \left(\frac{2\pi\nu + f}{K_0} \right)} \right]^{-1} e^{in \frac{2\pi}{2h} z},$$

which is most likely the correct expression Gonella intended to have printed in his 1972's paper (see his table 2). Please note that in Gonella (1972), the symbol for viscosity is ν.

References

Alford, M. H., 2001: Internal swell generation: The spatial distribution of energy flux from the wind to mixed layer near-inertial motions. *J. Phys. Oceanogr.*, **31**, 2359–2368.

Alford, M. H., 2003: Improved global maps and 54-year history of wind-work on ocean inertial motions. *Geophys. Res. Lett.*, **30**(8), 1424. doi:10.1029/2002GL016614,2003. 1424,10.1029/2002GL016614,2003.

AVISO, 1996: *AVISO User Handbook for Merged TOPEX/POSEIDON products*. AVISO/Altimetry, AVI-NT-02-101-CN, 3.0 edition.

Bendat, J. S., and Piersol, A. G., 1986: *Random data. Analysis and measurements procedures, Third Edition*. John Wiley & Sons.

Bender, C., and Orszag, S., 1999: *Advanced Mathematical Methods for Scientists and Engineers: Asymptotic Methods and Perturbation Theory*. Springer.

Chereskin, T., and Roemmich, D., 1991: A comparison of measured and wind-derived Ekman transport at 11-degrees-n in the Atlantic Ocean. *J. Phys. Oceanogr.*, **21**(6), 869–878.

Chereskin, T. K., 1995: Direct evidence for an Ekman balance in the California Current. *J. Geophys. Res.*, **100**(C9), 18,261–18,269.

Chereskin, T. K., Niiler, P. P., and Poulain, P. M., 1989: A numerical study of the effet of upper-ocean shear on flexible drogued drifters. *J. Atmos. Oceanic Technol.*, **6**(2), 243–253.

Chiu, W.-C., 1970: On the spectral equations and the statistical energy spectrum of atmospheric motions in the frequency domain. *Tellus*, **22**(6), 608–619.

Cisewski, B., Strass, V. H., and Prandke, H., 2005: Upper-ocean vertical mixing in the Antarctic Polar Front Zone. *Deep-Sea Res.*, **52**(9-10), 1087–1108. doi: http://dx.doi.org/10.1016/j.dsr2.2005.01.010.

Coleman, G., Ferziger, J., and Spalart, P., 1990: A numerical study of the turbulent Ekman layer. *Journal of Fluid Mechanics*, **213**, 313–348. doi: 10.1017/S0022112090002348.

Colin De Verdière, A., 1983: Lagrangian eddy statistics from surface drifters in the eastern North Atlantic. *J. Mar. Res.*, **41**(3), 375–398.

Craig, P., and Banner, M., 1994: Modeling wave-enhanced turbulence in the ocean surface layer. *J. Phys. Oceanogr*, **24**(12), 2546–2559.

Craig, P., Hunter, J., and Johnston, B., 1993: The implications of linearly varying eddy viscosity for wind-driven current profiles. *Cont. Shelf Res*, **13**(1), 1–24.

Craig, P. D., 1996: Velocity profiles and surface roughness under breaking waves. *J. Geosphys. Res.*, **101**, 1265–1278. doi:http://doi.dox.org/10.1029/95JC03220.

Crawford, G., and Large, W., 1996: Numerical investigation of resonant inertial response of the ocean to wind forcing. *J. Phys. Oceanogr.*, **26**(6), 873–891.

Csanady, G., 1997: The ”Slip Law” of the Free Surface. *Journal of Oceanography*, **53**(1), 67–80.

Csanady, G. T., and Shaw, P. T., 1980: The evolution of a turbulent Ekman layer. *J. Geophys. Res.*, **85**(C3), 1537–1547.

Daniault, N., Blouch, P., and Fusey, F. X., 1985: The use of free-drifting meteorological buoys to study winds and surface currents. *Deep-Sea Res.*, **32**(1), 107–113.

D’Asaro, E. A., 1985a: The energy flux from the wind to near-inertial motions in the surface mixed layer. *J. Phys. Oceanogr.*, **15**(8), 1043–1059.

D’Asaro, E. A., 1985b: Upper ocean temperature structure, inertial currents, and Richardson numbers observed during strong meteorological forcing. *J. Phys. Oceanogr.*, **15**(7), 943–962.

D’Asaro, E. A., Eriksen, C. C., Levine, M. D., Niiler, P., Paulson, C. A., and Van Meurs, P., 1995: Upper-ocean inertial currents forced by a strong storm. Part I: Data and comparisons with linear theory. *J. Phys. Oceanogr.*, **25**(11), 2909–2936.

Davis, R., de Szoeke, R., Halpern, D., and Niiler, P., 1981: Variability in the upper ocean during MILE. Part I: The heat and momentum balances. *Deep-Sea Res.*, **28A**, 1427–1451.

Dong, S., Sprintall, J., and Gille, S. T., 2006: Southern ocean mixed-layer depth from ARGO float profiles. Submitted to J. Geophys. Res.

Ducet, N., Le Traon, P. Y., and Reverdin, G., 2000: Global high-resolution mapping of ocean circulation from TOPEX/Poseidon and ERS-1 and-2. *J. Geophys. Res.*, **105**, 19477–19498.

Efron, B., and Gong, G., 1983: A Leisurely Look at the Bootstrap, the Jackknife, and Cross-Validation. *The American Statistician*, **37**(1), 36–48.

Ekman, V. W., 1905: On the influence of the Earth's rotation on ocean currents. *Ark. Mat. Astr, Fys.*, **2**(11), 1–36.

Ferrari, R., and McWilliams, J. C., 2006: Parameterization of eddy fluxes near oceanic boundaries. Submitted to Ocean Modelling.

Fofonoff, N. P., 1981: The Gulf Stream. In *Evolution of Physical Oceanography: scientific surveys in honor of Henry Stommel*, editors B. A. Warren, and C. Wunsch, 112–139. MIT Press.

Gill, A. E., 1982: *Atmosphere-Ocean Dynamics*. Academic Press.

Gill, A. E., Green, J. S. A., and Simmons, A., 1974: Energy partition in the large-scale ocean circulation and the production of mid-ocean eddies. *Deep-Sea Res.*, **21**, 499–528.

Gille, S. T., 2005: Statistical characterization of zonal and meridonal ocean wind stress. *J. Atmos. Oceanic Technol.*, **22**(9), 1353–1372.

Gille, S. T., Stevens, D. P., Tokmakian, R. T., and Heywood, K. J., 2001: Antarctic Circumpolar Current response to zonally averaged winds. *J. Geophys. Res.*, **106**(C2), 2743–2759.

Gonella, J., 1972: A rotary-component method for analysing meteorological and oceanographic vector time series. *Deep-Sea Res.*, **19**, 833–846.

Gouretski, V. V., and Jancke, K., 1998: A new climatology for the world ocean. WHP SAC Tech. Rep. no. 3, WOCE Report No. 162/98, WOCE Special Analysis Centre, Max-Planck Institute, Hamburg.

Gregg, M. C., 1987: Diapycnal mixing in the thermocline: a review. *J. Geophys. Res.*, **92**, 5249–5286.

Hansen, D. V., and Poulain, P.-M., 1996: Quality control and interpolations of WOCE-TOGA drifter data. *J. Atmos. Oceanic Technol.*, **13**(4), 900–909.

Harris, F. J., 1978: On the use of windows for harmonic analysis with the discrete fourier transform. *Proceedings of the IEEE*, **66**(1).

Hasselmann, K., 1976: Stochastic climate models Part I. Theory. *Tellus*, **28**(6), 473–485.

Huang, N. E., 1979: On surface drift currents in the ocean. *J. Fluid Mech.*, **91**(1), 191–208. doi:http://dx.doi.org/10.1017/S0022112079000112.

Huang, R. X., Wei, W., and Liu, L. L., 2006: Decadal variability of wind-energy input to the world. *Deep Sea Research Part II: Topical Studies in Oceanography*, **53**(1-2), 31–41.

Jordan, T. F., and Baker, J. R., 1980: Vertical Structure of Time-Dependent Flow Dominated by Friction in a Well-Mixed Fluid. *J. Phys. Oceanogr.*, **10**(7), 1091–1103.

Kalnay, E., Kanamitsu, M., Kistler, R., Collins, W., Deaven, D., Gandin, L., Iredell, M., Saha, S., White, G., Woollen, J., Zhu, Y., Leetmaa, A., Reynolds, B., Chelliah, M., Ebisuzaki, W., Higgins, W., Janowiak, J., Mo, K., Ropelewski, C., Wang, J., Jenne, R., and Joseph, D., 1996: The NCEP/NCAR 40-year reanalysis project. *Bull. Amer. Meteor. Soc.*, **77**, 437–471.

Kundu, P. K., and Cohen, I. M., 2002: *Fluid Mechanics*. Academic Press, San Diego, second edition edition.

Large, W., and Pond, S., 1981: Open ocean momentum flux measurements in moderate to strong winds. *J. Phys. Oceanogr.*, **11**(3), 324–226.

Large, W. G., Danabasoglu, G., Doney, S. C., and McWilliams, J. C., 1997: Sensitivity to surface forcing and boundary layer mixing in a global ocean model: Annual-mean climatology. *J. Phys. Oceanogr.*, **27**(11), 2418–2447.

Large, W. G., McWilliams, J. C., and Doney, S. C., 1994: Oceanic vertical mixing: a review and a model with a nonlocal boundary layer parameterization. *Reviews of Geophysics*, **32**, 363–404. doi:10.1029/94RG01872.

Lenn, Y.-D., 2006: *Observations of Antarctic Circumpolar Current Dynamics in Drake Passage and Small-scale Variability near the Antarctic Peninsula*. Ph.D. thesis, University of California, San Diego.

Lewis, D. M., and Belcher, S. E., 2004: Time-dependent, coupled, Ekman boundary layer solutions incorporating Stokes drift. *Dyn. Atmos. Oceans*, **37**(4), 313–351.

Lumpkin, R., and Flament, P., 2001: Lagrangian statistics in the central North Pacific. *J. Mar. Syst.*, **29**, 141–155.

Madsen, O. S., 1977: A realistic model of the wind-induced ekman boundary layer. *J. Phys. Oceanogr.*, **7**(2), 248–255.

McNally, G. J., Luther, D. S., and White, W. B., 1989: Subinertial frequency response of wind-driven currents in the mixed layer measured by drifting buoys in the midlatitude North Pacific. *J. Phys. Oceanogr.*, **19**, 290–300.

Melville, W. K., 1977: Wind stress and roughness length over breaking waves. *J. Phys. Oceanogr.*, **7**(5), 702–710.

Mestas-Nuñez, A. M., Chelton, D. B., and De Szoeke, R. A., 1992: Evidence of time-dependent Sverdrup circulation in the South Pacific from the Seasat scatterometer and altimeter. *J. Phys. Oceanogr.*, **22**, 934–943.

Middleton, J. F., and Garrett, C., 1986: A kinematic analysis of polarized eddy fields using drifter data. *J. Geophys. Res.*, **91**(C4), 5094–5102.

Mooers, C. N. K., 1973: A technique for the cross spectrum analysis of pairs of complex-valued time series, with emphasis on properties of polarized components and rotational invariants. *Deep-Sea Res.*, **20**(12), 1129–1141.

Naveira Garabato, A. C., Polzin, K. L., King, B. A., Heywood, K. J., and Visbeck, M., 2004: Widespread Intense Turbulent Mixing in the Southern Ocean. *Science*, **303**(5655), 210–213.

Nelder, J. A., and Mead, R., 1965: A simplex method for function minimization. *Computer Journal*, **7**(4), 308–313.

Niiler, P., Maximenko, N. A., and C., M. J., 2003: Dynamically balanced absolute sea level of the global ocean derived from near-surface velocity observations. *Geophys. Res. Let.*, **30**(22). doi:doi:10.1029/2003GL018628, 2003.

Niiler, P. P., and Paduan, J. D., 1995: Wind-driven motions in the Northeast Pacific as measured by Lagrangian drifters. *J. Phys. Oceanogr.*, **25**(11), 2819–2830.

Niiler, P. P., Sybrandy, A. L., Bi, K., Poulain, P., and Bitterman, D., 1995: Measurements of the water-following capability of holey-sock and TRISTAR drifters. *Deep-Sea Res.*, **42**, 1951–1964.

O'Brien, 1970: A note on the vertical structure of the edyy exchange coefficient in the planetary boundar layer. *J. Atmos. Sci.*, **27**, 1213–1215.

Orsi, A. H., and Whitworth, T. I., 2004: *Hydrographic Atlas of the World Ocean Circulation Experiment (WOCE). Volume 1: Southern Ocean, (Eds. M. Sparrow, P. Chapman and J. Gould)*. International WOCE Project Office, Southampton, U.K. ISBN 0-904175-49-9. 2004.

Orsi, A. H., Whitworth, T. I., and Nowlin, W. D. J., 1995: On the meridional extend and fronts of the Antarctic Circumpolar Current. *Deep-Sea Res.*, **42**(5), 641–673.

Osborne, A. R., Kirwan, A. D. J., Provenzale, A., and Bergamasco, L., 1989: Fractal drifter trajectories in the Kuroshio. *Tellus*, **41-A**, 416–435.

Pedlosky, J., 1979: *Geophysical Fluid Dynamics*. Springer.

Pinton, J.-F., and Labbé, R., 1994: Correction to the Taylor hypothesis in swirling flows. *Journal de Physique II*, **4**(9).

Plueddemann, A., and Farrar, J., 2006: Observations and models of the energy flux from the wind to mixed-layer inertial currents. *Deep-Sea Res.*

Pollard, R. T., 1970: On the generation by winds of inertial waves in the ocean. *Deep-Sea Res.*, **17**, 795–812.

Pollard, R. T., and Millard, R. C. J., 1970: Comparison between observed and simulated wind-generated inertial oscillations. *Deep-Sea Res.*, **17**, 813–821.

Pond, S., and Pickard, G. L., 1983: *Introductory Dynamical Oceanography*. Butterworth Heinemann.

Poulain, P.-M., 1990: Near-inertial and diurnal motions in the trajectories of mixed layer drifters. *J. Mar. Res.*, **48**, 793–823.

Poulain, P.-M., Luther, D. S., and Patzert, W. C., 1992: Deriving inertial wave characteristics from surface drifter velocities: Frequency variability in the Tropical Pacific. *J. Geophys. Res.*, **97**(C11), 17947–17959.

Prandtl, L., 1952: *Essentials of fluid dynamics: with applications to hydraulics, aeronautics, meteorology and other subjects*. Blackie.

Press, W. H., Flannery, B. P., Teukolsky, S. A., and Vetterling, W. T., 1988: *Numerical Recipes in Fortran 77*. Cambridge University Press.

Price, J., and Sundermeyer, M., 1999: Stratified Ekman layers. *J. Geophys. Res.*, **104**(C9), 20467–20494.

Price, J. F., Weller, R. A., and Schudlich, R. R., 1987: Wind-driven ocean currents and Ekman transport. *Science*, **238**(4833), 1534–1538.

Rio, M., and Hernandez, F., 2004: A mean dynamic topography computed over the world ocean from altimetry, in situ measurements, and a geoid model. *J. Geophys. Res*, **109**, 1–19. doi:10.1029/2003JC002226.

Rio, M. H., and Hernandez, F., 2003: High-frequency response of wind-driven currents measured by drifting buoys and altimetry over the world ocean. *J. Geophys. Res.*, **108**(C8), 3283. doi:10.1029/2002JC001655,2003. 3283,10.1029/2002JC001655,2003.

Rupolo, V., Bach, L. H., Provenzale, A., and Artale, V., 1996: Lagragian velocity spectra at 700 m in the western North Atlantic. *J. Phys. Oceanogr.*, **26**(8), 1591–1607.

Saji, P. K., Shenoi, S. C., Almeida, A., and Rao, G., 2000: Inertial currents in the Indian Ocean derived from satellite tracked surface drifters. *Oceanologica Acta*, **23**, 635–640.

Santiago-Mandujano, F., and Firing, E., 1990: Mixed-Layer Shear Generated by Wind Stress in the Central Equatorial Pacific. *J. Phys. Oceanogr*, **20**, 1576–1582. doi: 10.1175/1520-0485(1990)020¡1576:MLSGBW¿2.0.CO;2.

Schmidt, H., and Jirstrand, M., 2005: Systems bilogy toolbox for matlab: A computational platform for research in System Biology. *Bioinformatics Advance Access*. doi: 10.1093/bioinformatics/bti799. November 2005, DOI 10.1093/bioinformatics/bti799.

Schudlich, R., and Price, J., 1998: Observations of Seasonal Variation in the Ekman Layer. *J. Phys. Oceanogr.*, **28**(6), 1187–1204.

Siedler, G., Church, J., and Gould, J., editors, 2001: *Ocean Circulation and Climate - Observing and Modelling the Global Ocean*. Academic Press.

Simmons, A. J., and Gibson, J. K., 2000: ERA-40 project report series n0.1: The ERA-40 project plan. Technical report, European Center for Medium-range Weather Forecasts.

Skyllingstad, E. D., Smyth, W. D., and Crawford, G. B., 2000: Resonant wind-driven mixing in the ocean boundary layer. *J. Phys. Oceanogr.*, **30**(8), 1866–1890.

Sloyan, B. M., 2005: Spatial variability of mixing in the Southern Ocean. *Geophys. Res. Lett.*, **32**, L18603.

Smith, S. D., 1980: Wind stress and heat flux over the ocean in gale force winds. *J. Phys. Oceanogr.*, **10**, 709–726.

Stips, A., Burchard, H., Bolding, K., Prandke, H., Simon, A., and Wuest, A., 2005: Measurement and simulation of viscous dissipation in the wave affected surface layer. *Deep Sea Research Part II: Topical Studies in Oceanography*, **52**(9-10), 1133–1155.

Stockwell, R. G., Large, W. G., and Milliff, R. F., 2004: Resonant inertial oscillations in moored buoy ocean surface winds. *Tellus A*, **56**(5), 536–536.

Sybrandy, A. L., and Niiler, P., 1991: WOCE/TOGA Lagrangian drifter construction manual, SIO ref. series 91/6. Technical Report WOCE Report N. 63/91, WOCE International Project Office.

Tapley, B., Ries, J., Bettadpur, S., Chambers, D., Cheng, M., Condi, F., Gunter, B., Kang, Z., Nagel, P., Pastor, R., Pekker, T., Poole, S., and Wang, F., 2005: GGM02 - an improved Earth gravity field model from GRACE. *J. Geod.*, **79**(8), 467–478.

Tennekes, H., 1973: The logarithmic wind profile. *J. Atmos. Sci*, **30**(2), 234–238.

Terray, E., Donelan, M., Agrawal, Y., Drennan, W., Kahma, K., Williams III, A., Hwang, P., and Kitaigorodskii, S., 1996: Estimates of kinetic energy dissipation under breaking waves. *J. Phys. Oceanogr*, **26**(5), 792–807.

Thomas, J., 1975: A theory of steady wind-driven currents in shallow water with variable eddy viscosity. *J. Phys. Oceanogr.*, **5**(1), 136–142.

Thompson, A., Gille, S., MacKinnon, J., and Sprintall, J., 2006: Spatial and temporal patterns of small-scale mixing in drake passage. *J. Phys. Oceanogr.* In press.

Toggweiler, J., and Samuels, B., 1998: On the Ocean's Large-Scale Circulation near the Limit of No Vertical Mixing. *J. Phys. Oceanogr.*, **28**(9), 1832–1852.

Wang, W., and Huang, R., 2004: Wind energy input to the Ekman layer. *J. Phys. Oceanogr*, **34**(5), 1267–1275.

Watanabe, M., and Hibiya, T., 2002: Global estimates of the wind-induced energy flux to inertial motions in the surface mixed layer. *Geophys. Res. Lett.*, **29**(8), 1239. doi: doi:10.1029/2001GL014422,2002. 1239,10.1029/2001GL014422,2002.

Weijer, W., and Gille, S. T., 2005: Energetics of wind-driven barotropic variability in the Southern Ocean. *J. Mar. Res.*, **63**(6), 1101–1125.

Weller, R., and Plueddemann, A., 1996: Observations of the vertical structure of the oceanic boundary layer. *J. Geophys. Res.*, **101**(C4), 8789–8806.

Weller, R. A., 1981: Observations of the velocity response to wind forcing in the upper ocean. *J. Geophys. Res.*, **86**(C3), 1969–1977.

Wijffels, S., Firing, E., and Bryden, H., 1994: Direct observations of the Ekman balance at 10°N in the Pacific. *J. Phys. Oceanogr.*, **24**, 1666–1679.

Wu, J., 1980: Wind-stress coefficients over sea surface near neutral conditions A revisit. *Journal of Physical Oceanography*, **10**, 727–740.

Wunsch, C., 1998: The work done by the wind on the oceanic general circulation. *J. Phys. Oceanogr.*, **28**(11), 2332–2340.

Wunsch, C., and Ferrari, R., 2004: vertical mixing, energy, and the general circulation of the oceans. *Ann. Rev. Fluid Mech.*, **36**(1), 281–314.

Yelland, M., and Taylor, P., 1996: Wind stress measurements from the open ocean. *J. Phys. Oceanogr*, **26**(4), 541–558.